AD_____

Award Number: DAMD17-00-1-0596

TITLE: Real-Time Palpation Imaging for Improved Detection and Discrimination of Breast Abnormalities

PRINCIPAL INVESTIGATOR: Timothy J. Hall, Ph.D.

CONTRACTING ORGANIZATION: University of Kansas Medical Center
Kansas City, KS 66160-7700

REPORT DATE: October 2003

TYPE OF REPORT: Annual

PREPARED FOR: U.S. Army Medical Research and Materiel Command
Fort Detrick, Maryland 21702-5012

DISTRIBUTION STATEMENT: Approved for Public Release;
Distribution Unlimited

The views, opinions and/or findings contained in this report are those of the author(s) and should not be construed as an official Department of the Army position, policy or decision unless so designated by other documentation.

20040220 032

REPORT DOCUMENTATION PAGE

Form Approved
OMB No. 074-0188

1. AGENCY USE ONLY (Leave blank)	2. REPORT DATE October 2003	3. REPORT TYPE AND DATES COVERED Annual (15 Sep 2002 – 14 Sep 2003)	
4. TITLE AND SUBTITLE Real-Time Palpation Imaging for Improved Detection and Discrimination of Breast Abnormalities		**5. FUNDING NUMBERS** DAMD17-00-1-0596	
6. AUTHOR(S) Timothy J. Hall, Ph.D.			
7. PERFORMING ORGANIZATION NAME(S) AND ADDRESS(ES) University of Kansas Medical Center Kansas City, KS 66160-7700 E-Mail: thall@kumc.edu		**8. PERFORMING ORGANIZATION REPORT NUMBER**	
9. SPONSORING / MONITORING AGENCY NAME(S) AND ADDRESS(ES) U.S. Army Medical Research and Materiel Command Fort Detrick, Maryland 21702-5012		**10. SPONSORING / MONITORING AGENCY REPORT NUMBER**	

11. SUPPLEMENTARY NOTES

12a. DISTRIBUTION / AVAILABILITY STATEMENT Approved for Public Release; Distribution Unlimited	12b. DISTRIBUTION CODE

13. ABSTRACT (Maximum 200 Words)

The purpose of our work is to develop and test a new kind of imaging system we call "palpation imaging". We expect that palpation imaging will be a useful tool for improving the discrimination between benign and malignant breast tumors. The scope of the effort in our first two years of funding was to implement our algorithm for imaging tissue elasticity on a commercial ultrasound imaging system and to begin testing that new imaging system. These images are produced at substantially real-time frames rates with normal ultrasound B-mode and strain images displayed side-by-side. These algorithms are fully integrated into the commercial system and require no system modifications. Year two efforts also involved increasing the clinical testing of these tools and investigating other elasticity imaging techniques. Breast exams performed on volunteers have shown that palpation imaging techniques are almost identical to the standard clinical breast ultrasound exam. Elasticity image information appears useful for differentiating atypical cysts, fibroadenomas, and invasive ductal carcinomas. Further testing is required to evaluate statistical performance.

14. SUBJECT TERMS Breast Imaging			15. NUMBER OF PAGES 84
			16. PRICE CODE

17. SECURITY CLASSIFICATION OF REPORT Unclassified	18. SECURITY CLASSIFICATION OF THIS PAGE Unclassified	19. SECURITY CLASSIFICATION OF ABSTRACT Unclassified	20. LIMITATION OF ABSTRACT Unlimited

NSN 7540-01-280-5500

Standard Form 298 (Rev. 2-89)
Prescribed by ANSI Std. Z39-18
298-102

Table of Contents

Introduction

The purpose of our work is to develop and test a new kind of imaging method we call "palpation imaging". We expect that palpation imaging will be a useful tool for improving the discrimination between benign and malignant breast tumors. The scope of the effort in our first two years of funding was to implement a newly-developed algorithm for motion tracking on a commercial ultrasound imaging system and to begin testing that new imaging system. The algorithm provides images of the mechanical strain induced in tissue by pressing the ultrasound transducer against the skin surface. These images are produced at substantially real-time frames rates with normal ultrasound B-mode and strain images displayed side-by-side. The algorithm is fully integrated into the commercial system and requires no system modifications. Breast exams performed on volunteers have shown that the palpation imaging study is almost identical to the standard clinical breast ultrasound exam. With the patients examined to date, we find distinct strain image sequences for cysts, fibroadenomas, and invasive ductal carcinomas. A comparison of lesion area measured in B-mode versus strain images appears to provide good discrimination between benign and malignant lesions with the data obtained so far. This work is summarized in a manuscript published in *Ultrasound in Medicine and Biology* 29(3): 427-35, 2003 (attached as Appendix 1 in the annual report last year).

The plans for the third and final year of the proposed effort included a larger, more well-defined study of the performance of palpation imaging for breast lesion classification. We planned to scan enough human subjects to obtain at least 100 patients with biopsy of surgery-proven lesion type. Unfortunately, there has been a significant shortfall in the human subject recruitment for this project. This is due to a lack of cooperation of the clinician co-investigators involved in this project. The shortage of medical staff and an increased demand to provide clinical care has left these co-investigators with limited time for research activities. Those changes as well as an outstanding opportunity resulted in the Principle Investigator, Timothy Hall, leaving the University of Kansas Medical Center (KUMC) for a position as a tenured Professor in the Medical Physics Department at the University of Wisconsin-Madison (UW). The benefits of this change of environment are wide-ranging and include a large department of investigators pursuing advances in medical imaging, a vast pool of graduate students and post-doctoral candidates to work with, and a medical staff actively involved in

our research.

Expenditure of funds at KUMC ceased 18.Jan.2003, two days after Professor Hall started work at UW. Although work has continued on this project, at both KUMC and UW, no additional funds have been spent against the grant. We have been working toward transferring this grant to UW since that time. It appears that the process is nearly complete. Associated with the grant transfer we have requested a one-year no-cost extension of this grant period. This will provide ample time to complete that proposed study.

Body

Four of the six proposed Tasks (Tasks 1–3 and 6) have been addressed so far within this project. The overall effort has been very successful and has drawn attention of the elasticity imaging research community around the world. We are extremely excited with our results to date and are very encouraged with the potential for this new kind of imaging system. Below is a description of the approved Tasks and the progress toward achieving each goal.

Task 1. *Implement real-time palpation imaging on a commercial sonography system (months 1-4): a) Program the imaging system digital signal processors to estimate strain from consecutive image frames. b) Develop a user interface for controlling the data acquisition and processing parameters. c) Test the system using existing phantoms and laboratory fixtures with motorized motion control to determine the penalty for using fixed-point versus floating point calculations.*

This task has been completed, as described in the year-2 report. We are grateful to SMSUG for their technical assistance in this effort. The software we have developed is fully functional, and has gone through multiple improvements. The current version displays 3 cm wide by 3.5 cm deep image pairs at about seven frames per second (73.5 cm^2/sec). That frame rate is sufficiently fast to provide feedback to the hand-eye coordination system to allow manipulating the conditions of tissue compression to consistently obtain high-quality strain images. The manuscript that describes the implementation of this algorithm and initial testing for displacement variance is published (Ultrasonic Imaging 24(3): 161-176, 2002).

Task 2. *Develop data acquisition techniques that provide high-quality palpation images without the use of fixtures (months 3-12): a) Implement techniques that mimic those used for phantom imaging including small hand-*

5

held fixtures to restrict motion perpendicular to the image plane. b) Test those techniques in phantoms and compare target contrast-to-noise ratio for laboratory (large motorized fixtures, controlled motion) versus clinical (small hand-held fixtures, restricted motion) systems. c) Test the clinical systems (real-time palpation imaging with small fixtures) using anthropomorphic breast phantoms. d) Test the clinical systems on volunteer patients with palpable breast abnormalities. e) Modify the data acquisition techniques to eliminate the need for fixtures to restrict motion while maintaining image quality. f) Measure conspicuity of breast lesions to assess the relative merit of different data acquisition techniques.

This task has been completed, as described in the year-2 report. Iterating between what we learned with freehand scanning of phantoms, then in vivo breasts, and back to phantoms, we found that the key to obtaining sequences of high-quality strain images (high contrast-to-noise and high similarity from frame to frame) with freehand scanning is high frame rate. The scanning technique for breast palpation imaging is nearly identical to that used in typical breast sonography with compression. The subject lies on her back with her arm behind her head and the ultrasound transducer is pressed, by hand, toward the chest wall. The real-time image feedback allow manipulation of the compression conditions while scanning. This manipulation is essential for obtaining long sequences of low noise strain image data (often 100 image frames).

Task 3. *Implement high-quality palpation imaging algorithm on a commercial sonography system and perform preliminary tests of image quality (months 7-17): a) Program the commercial sonography system to calculate high-resolution, low-noise palpation images as quickly as possible over a large region of interest. b) Develop a user interface that allows manipulation of the image formation algorithm for the trade-off between spatial resolution and image noise. c) Test the high-quality algorithm on (geometrically) simple and anthropomorphic phantoms using the modified data acquisition techniques (Task 2.e). d) Use the real-time palpation imaging technique to locate the desired region of interest and obtain sonographic data with the appropriate pre- and post-compression for volunteer patients with palpable breast abnormalities.* and **Task 6.** *Investigate the use of novel techniques, such as harmonic imaging and spatial quadrature, for improved information content in palpation images (months 18-36).*

This area of work has been our dominant effort since the first year of support. As described in the year–1 report, we can estimate displacement

6

and strain accurately in inhomogeneous media (tissue) with greater success than originally anticipated. The key to this success is real-time imaging of strain that guides manipulation of the conditions of compression.

As described in previous reports, we have implemented three displacement and strain estimation algorithms on the Elegra. The simplest of these is the algorithm that runs in real-time for data acquisition. This uses our patented adaptive search strategy to predict the deformation based on previous displacement estimates. This adaptive search reduces the computational load for strain estimation by more than a factor of 100. The algorithm also decimates the data, thereby reducing the number of displacement estimates in a given region of interest. This algorithm is used primarily for data acquisition during freehand scanning and is a compromise between frame rate and image quality. To halt data acquisition, the system 'freeze' button is pressed, just as in normal sonography, and the echo data are available for on-line post-processing. This same (real-time) strain imaging algorithm can be used to reprocess that data as the user scrolls through image memory, or one of the other algorithms can be used. The second algorithm is identical to the first except that the data is not decimated. Estimating displacement with higher data density reduces the displacement variance in the adaptive search strategy resulting in a slight improvement in image quality. The third algorithm operates on the full data field (no decimation) and does not use the adaptive search strategy, instead using a full 2-D search. This approach is much more computationally intensive, requiring about one second per strain image frame, but produces images that lack the displacement error accumulation that can result from the adaptive search strategy.

We are continuing to investigate options to further improve image quality, as described in the year-2 annual report. These advances are expected to significantly improve on-line post-processed images. As a result of that effort it has become clear that subjective visual assessment of image 'quality' and lesion conspicuity are not sufficient to quantify differences among motion tracking algorithms. As a result, we are working on a quantitative method for measuring the accuracy of motion tracking in tissues in addition to the estimates of displacement estimate error variance that are commonly reported. This work is very early in development, and is not expected to be completed during this project period. But, the approach shows great promise for comparing the relative performance of various motion tracking algorithms and parameter selection for a specific algorithm.

To date we have scanned 56 volunteers at KUMC. Some of these patients

had multiple lesions, and some were scanned on repeat occasions (perpendicular image planes, repeat visits, different transducers, etc). As reported last year, the excitement from the potential for palpation imaging and the delay at KUMC in obtaining a sufficient number of patients to adequately test this technology resulted in Siemens contracting with two other institutions to test our technology (Charing Cross Hospital in London, UK and Mayo Clinic, Rochester, MN). Those sites have been quite productive in their trials. To date the Charing Cross group has scanned over 200 breast patients and the Mayo group has scanned over 100 patients. Each found that they became proficient in their scanning technique within 10–15 patients, and they find that palpation imaging adds, on average, about five additional minutes to the normal breast ultrasound examination. The key to strain imaging, as in standard sonography, is training. With real-time feedback of the current strain images being acquired, the key is interpreting the data and making corrections to the technique, if necessary. In summary, the tools are adequate, the key to success is training.

As described in the previous annual reports, we have demonstrated evidence for changing strain image contrast in fibroadenomas as the surface pressure increases. Support for that observation continues to build, and that behavior continues to appear unique to fibroadenomas. The previous annual reports also described the frame-to-frame variability of strain images for cysts. Although those observations are still true of the cysts, our emphasis in data acquisition has been on solid lesions. We also provided evidence in previous reports describing the frame-to-frame similarity in strain images of invasive ductal carcinomas and evidence demonstrating that the apparent size of a carcinoma in strain images is larger than that seen in the B-mode images. Results reported in year–1 were for measurements performed by the PI. A more extensive study, described below, was reported at the Radiological Society of North America meeting in November 2002.

Garra, et al., (Radiology 202: 79-86, 1997) suggested that the width of a carcinoma in a strain image is typically larger than that measured in a B-mode image. Our results support that observation, and apparently extend its diagnostic utility, as described in the previous annual reports. To begin designing the experiments for Tasks 4 and 5, we asked five observers (the PI and four ultrasound clinicians) to view each sequence of side-by-side B-mode and strain images from the KUMC data. From each sequence, each observer had to choose an image pair that represented the typical view of the lesion in both B-mode and strain images. That image pair was then displayed

8

and the observer had to trace the lesion boundary in the B-mode image and measure the lesion height and width. The image pair was then re-displayed and the observer traced the lesion in the strain image and measure the lesion height and width. The combined average results for lesion measurements were shown in the year-2 report. A receiver operating charateristic (ROC) analysis of those measurements resulted in an overly-optimistic diagnostic accuracy of 0.983±0.028—nearly perfect performance. Although this is a very encouraging results, it cannot be trusted for several reasons including the small size of the patient pool, correlations among the data (multiple lesions in a single patient included in the study), and the limited variety of lesion types (invasive ductal carcinomas, fibroadenomas and cysts).

However, this work demonstrates that we are following a solid research plan. By increasing the size of the study population, and comparing the change in diagnostic accuracy when using standard sonography versus sonography plus palpation imaging, we can test the utility of palpation imaging as a diagnostic tool with ROC analysis and multi-observer measurements.

Our current plans are unchanged from those in the proposal and current protocol, except for the change of institution and the use of data from outside this funded project. We are well prepared to complete the final two tasks of the study: *Tasks 4. Acquire sonograms, elastograms, and mammograms on patients with suspicious lesions that are either palpable or detectable with sonography or mammography (months 18-32; >100 patients)and*
Task 5. Compare diagnosis of breast lesions with and without the use of palpation imaging. (months 30-36; using images obtained in Task 4).

Key Research Accomplishments

- The motion tracking algorithm has been implemented on the Siemens SONOLINE Elegra and displays B-mode and strain images side-by-side at about seven frames per second.

- We found that the key to obtaining high-quality in vivo strain images of the breast is to form the images in "real-time," that is, fast enough to provide the hand-eye coordination system sufficient feedback to control the conditions of tissue deformation.

- We have developed scanning techniques for acquiring strain image data from in vivo breasts that provides reproducible results. The technique

9

is nearly identical to typical breast sonography with compression, so it is relatively easy to learn and clinicians are likely to adopt the practice.

- There is no significant difference between the displacement variance (strain image noise) for freehand scanning versus motorized compression for strain imaging.

- We have found that the frame-to-frame strain patterns from various breast abnormalities appears to be unique to the abnormality. For example, the fluid within cysts appears to be 'stirred' when deformed in palpation imaging, and that 'stirring' causes the rf echo signal, and therefore the strain image, to decorrelate rapidly with time. We have also found that the strain contrast for fibroadenomas is not constant with compression; at very low surface pressure fibroadenomas are stiffer than their surroundings and provide high negative contrast. With increased surface pressure that contrast is often significantly reduced; Invasive ductal carcinomas maintain a high negative contrast at all surface pressures tested.

- We have found that by comparing the area of a lesion measured on the standard ultrasound B-mode image with area measured on a strain image, benign lesions have nearly equal area on both modalities but invasive ductal carcinomas are significantly larger on the strain image than in B-mode.

- The diagnostic criterion of comparing lesion size in B-mode versus strain images appears to be a strong criterion among a group of five observers. It must be noted that this was a relatively small data set with some lesions that were easily classified without the benefit of palpation imaging results. This criterion will be further tested in Tasks 4 and 5.

Reportable Outcomes

Manuscripts

1. "In vivo real-time freehand palpation imaging," Timothy J. Hall, Yanning Zhu, and Candace S. Spalding. Ultrasound Med Biol 29(3): 427-35, 2003.

2. "A modified block matching method for real-time freehand strain imaging," Yanning Zhu and Timothy J. Hall. Ultrasonic Imaging 24(3): 161-176, 2002.

3. "A Finite Element Approach for Young's Modulus Reconstruction," Yanning Zhu, Timothy J. Hall and Jingfeng Jiang. IEEE Trans Med Imaging 22(7): 890-901, 2003.

4. "Noise reduction strategies in freehand elasticity imaging" Timothy J. Hall, Jingfeng Jiang, Yanning Zhu, and Larry T. Cook, 2002 IEEE Ultrasonics Symposium Proceedings 02CH37388C: 1877 -1880, 2002.

5. "Beyond the basics: elasticity imaging with ultrasound," Timothy J. Hall Radiographics (to appear Nov.2003).

Abstracts

1. Hall TJ, Svensson W, Von Behren P, Malin J, Zhu Y, Spalding C, Hall M, Connors A, Lowery C, "Differentiating malignant from benign breast lesions noninvasively using real-time palpation imaging," J Ultrasound Med 29(5s):S93, 2003.

2. Hangiandreou NJ, Meixner DD, Hesley GK, Farrell MA, Morton MJ, Charboneau JW, Hall TJ, Zhu Y, Spalding CS, "Ultrasound strain image data obtained in breast masses: Preliminary quantitative analysis," J Ultrasound Med 29(5s): s178, 2003.

3. Cook LT, Zhu Y, Hall TJ, "Comparing one-dimensional and two-dimensional kernels for tracking two-dimensional motion ultrasonic echo data," J Ultrasound Med 29(5s): s206, 2003.

4. Hall TJ, "Elasticity imaging phantoms," J Ultrasound Med 29(5s): s207, 2003.

5. Cook LT, Zhu Y, Hall TJ, "The effect of kernel size on ultrasonic displacement estimation," Ultrasonic Imaging 25:56-7, 2003.

6. Zhu Y, Hall TJ, Cook LT, Jiang J, "Young's modulus reconstruction using ultrasound," Ultrasonic Imaging 25:64-65, 2003.

Presentations

Conference Presentation

1. "In Vivo Results of Real-Time Freehand Elasticity Imaging" by Hall TJ, Zhu Y, Spalding CS, Cook LT. Presented at the 2002 IEEE Ultrasonics Symposium, Munich, Germany, October, 2002.

2. "Lesion size measurement in palpation imaging" by Hall TJ, Spalding C, Hall M, Von Behren P, Zhu Y, Mayo M, Cook LT. Presented at the 88th Scientific Assembly and Annual Meeting of the Radiological Society of North America, Chicago, Illinois, December 2002.

3. "Differentiating malignant from benign breast lesions noninvasively using real-time palpation imaging," by Hall TJ, Svensson W, Von Behren P, Malin J, Zhu Y, Spalding C, Hall M, Connors A, Lowery C. Presented at the American Institute of Ultrasound in Medicine Annual Convention, Montreal, Canada, June 2003.

4. "Ultrasound strain image data obtained in breast masses: Preliminary quantitative analysis" by Cook LT, Zhu Y, Hall TJ. Presented at the American Institute of Ultrasound in Medicine Annual Convention, Montreal, Canada, June 2003 (poster).

5. "Elasticity imaging phantoms" by Hall TJ. Presented at the American Institute of Ultrasound in Medicine Annual Convention, Montreal, Canada, June 2003 (poster).

6. "Ultrasound strain image data obtained in breast masses: Preliminary quantitative analysis" by Hangiandreou NJ, Meixner DD, Hesley GK, Farrell MA, Morton MJ, Charboneau JW, Hall TJ, Zhu Y, Spalding CS. Presented at the American Institute of Ultrasound in Medicine Annual Convention, Montreal, Canada, June 2003 (poster).

7. "Young's modulus reconstruction using ultrasound" by Zhu Y, Hall TJ, Cook LT. Presented at the 28th International Symposium on Ultrasonic Imaging and Tissue Characterization, Arlington, Virginia, May 2003.

8. "The effect of kernel size on ultrasonic displacement estimation" by Cook LT, Zhu Y, Hall TJ. Presented at the 28th International Symposium on Ultrasonic Imaging and Tissue Characterization, Arlington, Virginia, May 2003.

Invited Symposia

1. "Beyond the basics: elasticity imaging with ultrasound," Timothy J. Hall Presented at the 88th Scientific Assembly and Annual Meeting of the Radiological Society of North America, Chicago, Illinois, December 2002.

Patents

1. Patent No. 6,508,768 B1, 21.Jan.2003 "Ultrasonic Elasticity Imaging" by Timothy J. Hall and Yanning Zhu.

Funding Applied For

1. 1RO1CA94057-01 "3-D Palpation Imaging with Ultrasound," Yanning Zhu, PI (resubmitted)

2. 1R01CA100373 "Palpation Imaging," Timothy J. Hall, PI (reviewed June 2003, scored 176, 19.3 percentile, council action pending)

3. SBIR "Absolute 3-D tactile imaging," Jae Son, Medical Tactile Systems, Inc. PI (resubmitted July 2003).

Conclusions

Our initial research plan included the development and initial testing of a method for real-time imaging of mechanical strain in tissue and is proceeding as planned. Our success in this effort far exceeds our anticipated results. The phantom studies proposed proved far too simple to evaluate the the merit of this technique, but the in vivo results demonstrate the reproducibility of strain imaging. Measurements of lesion size in strain images compared to B-mode images appears to be a sensitive diagnostic criterion for discriminating malignant from benign lesions. Further improvements in the motion tracking algorithm will make strain imaging more robust and increase the confidence of the sonographer. Our results to date indicate that real-time palpation imaging has the potential to significantly improve the diagnosis of breast abnormalities. This new tool runs as a software application on an existing clinical sonography system and is therefore easily distributed broadly when it

13

is an appropriate product. Our software is computationally intensive, but it is expected that future sonography systems from all manufacturers will have sufficient computational capacity to support this application. Wide-spread use would likely follow, if our current results are representative. We look forward to continued success.

Appendices

1. "In vivo real-time freehand palpation imaging," Timothy J. Hall, Yanning Zhu, and Candace S. Spalding. Ultrasound Med Biol 29(3): 427-35, 2003.

2. "A modified block matching method for real-time freehand strain imaging," Yanning Zhu and Timothy J. Hall. Ultrasonic Imaging 24(3): 161-176, 2002.

3. "A Finite Element Approach for Young's Modulus Reconstruction," Yanning Zhu, Timothy J. Hall and Jingfeng Jiang. IEEE Trans Med Imaging 22(7): 890-901, 2003.

4. "Noise reduction strategies in freehand elasticity imaging" Timothy J. Hall, Jingfeng Jiang, Yanning Zhu, and Larry T. Cook, 2002 IEEE Ultrasonics Symposium Proceedings 02CH37388C: 1877 -1880, 2002.

5. "Beyond the basics: elasticity imaging with ultrasound," Timothy J. Hall Radiographics (to appear Nov.2003).

doi:10.1016/S0301-5629(02)00733-0

● *Original Contribution*

IN VIVO REAL-TIME FREEHAND PALPATION IMAGING

TIMOTHY J. HALL, YANNING ZHU and CANDACE S. SPALDING

Department of Radiology, University of Kansas Medical Center, Kansas City, KS, USA

Abstract—Previous experience with laboratory fixtures and off-line processing of elasticity data showed that problems occurring in data acquisition often resulted in poor elasticity image quality. A system for real-time estimation and display of tissue elastic properties using a clinical ultrasonic imaging system has been developed. A brief description of that system and the initial clinical tests of that system are reported. Experience with real-time freehand elasticity imaging shows that images with high contrast-to-noise ratios are consistently obtained. Images of breast lesions were acquired with freehand palpation using standard linear-array ultrasound (US) transducers. Results in volunteer patients show that high-quality elasticity images are easily obtained from *in vivo* breast studies. The key element to successful scanning is real-time visual feedback of B-mode and strain images that guide the patient positioning and compression direction. Results show that individual images of axial strain in tissues can be quite misleading, and that a "movie loop" of side-by-side B-mode and strain images provides significantly more information. Our preliminary data suggest that the strain image sequences for various breast pathologies are unique. For example, strain images of fibroadenomas lose contrast with increasing precompression, but those of invasive ductal carcinoma have high negative contrast (dark relative to "normal" tissue) for a wide range of precompression. In addition, a comparison of the lesion area measured in B-mode vs. strain images, for a representative image from the sequence, appears to be a sensitive criterion for separating invasive ductal carcinoma from cyst and fibroadenoma. (E-mail: thall@wisc.edu) © 2003 World Federation for Ultrasound in Medicine & Biology.

Key Words: Ultrasound, Tissue characterization, Elasticity, Palpation, Elastography.

INTRODUCTION

The potential for improving the qualitative nature of palpation by imaging quantitative measures of tissue viscoelasticity has generated a great deal of interest world-wide. Our initial efforts focused on modeling displacement and strain, developing algorithms for displacement and strain estimation, and testing those techniques in phantoms and in kidneys *in vitro* (see, for example, Chaturvedi et al. 1998a, 1998b; Hall et al. 1997; Insana et al. 1997; Zhu et al. 1998). Significant effort was expended on developing high-order motion estimators for tracking fine-scale motion. However, little data were available to investigate the need or utility of the high-order motion-estimation techniques for *in vivo* imaging of tissues.

The first report testing the utility of strain imaging in breast lesion imaging (Garra et al. 1997) clearly demonstrated that strain imaging had merit in breast lesion

discrimination. The data-acquisition system employed a modified mammography compression paddle and, therefore, was limited in the lesion locations that could be studied. Also, only (nonreal-time) static strain images were available. In that report, Garra et al. (1997) described a set of criteria applied to evaluate strain imaging combined with normal B-mode imaging. Among those criteria were lesion visibility, relative brightness, lesion margin regularity, lesion margin definition, lesion size (lateral and axial) and B-mode image measurements relative to strain image and pathology measurements. Among their findings, they noted that benign lesions have about the same width on B-mode and strain images, but that the height measurement had lower confidence due to axial blurring in strain image formation and difficulty in determining lesion boundaries with shadows due to high attenuation. Fibroadenomas typically had heterogeneous stiffness; cancers were uniformly stiffer than their surroundings in all but one case.

The purpose of the present study was to test the utility of performing strain imaging in real-time on a commercial ultrasound (US) imaging system and to test

Address correspondence to: Timothy J. Hall, Medical Physics Department, 1530MSC, 1300 University Ave, Madison, WI 53706 USA. E-mail: tjhall@wisc.edu

one of the strain image criteria described by Garra et al. (1997) with data acquired from this new system. Results demonstrate the value in real-time side-by-side display of B-mode and strain images for guiding data acquisition and data interpretation. Comparisons among various lesion types studied *in vivo* show a significant difference in the strain image sequence for fibroadenomas, cysts and carcinoma, and help to explain some of the difficulties in data interpretation described by Garra et al. (1997). Our results are generally consistent with those found by Garra and colleagues, but the differences we found in carcinoma size in B-mode and strain images are greater, and all lesions found in sonography or mammography, whether palpable or not, were visible with our techniques. These results will help to guide future strain-imaging data acquisition and provide further evidence for the potential of elasticity imaging in breast lesion discrimination.

MATERIALS AND METHODS

The motion-tracking algorithm, its implementation on the commercial clinical US, imaging system and performance measurements in experiments with phantoms are reported elsewhere (Zhu and Hall 2002). The essential details are included here for the convenience of the reader.

Strain image formation

A 2-D block-matching algorithm, based on the sum-squared difference (SSD) method, was used for motion tracking in our implementation. With this method, motion is tracked by searching for a kernel of data from the precompression radio frequency (RF) echo data in a 2-D search region of the postcompression RF echo field. A fixed kernel size (five A-lines by 11 RF samples) was used with both the 7.5L40 (with and without tissue harmonic imaging, THI) and the VFX13-5 linear arrays for the system employed (Siemens SONOLINE Elegra, Issaquah, WA). The data are temporally sampled at 36 MHz with a lateral beam spacing of 200 μm. Therefore, the kernel size corresponds to about about one half the area of the 2-D pulse-echo US point spread function for the 7.5L40 array pulsed at 7.2 MHz. A small kernel was chosen because the assumption of rigid body motion is increasingly accurate as the size of the kernel is decreased, and because spatial resolution is expected to improve with smaller kernels. No attempt to optimize the kernel size was pursued in this study. Kernel size optimization will likely be task-dependent and will be addressed in future work.

Data were processed on the image processor subsystem of the Elegra. This subsystem hosts two Texas Instruments TMS320C80 processors. To reduce the computational load (required to achieve real-time frame rates), an adaptive search strategy was developed that reduces the size of the required search region in performing the SSD block matching. Displacements are estimated (for real-time imaging) with kernels that are separated by 16 RF samples center-to-center (no spatial overlap of displacement estimates). Displacements are estimated row-by-row, and the prior row of estimates are used to predict displacements in the current row, allowing the search region to be reduced to within one RF sample in each direction of the predicted displacements. The use of predicted displacements results in correlated displacement errors, and an error detection and correction scheme was also implemented. Strain is estimated from the displacement data using a linear regression technique similar to that described by Kallel and Ophir (1997). For real-time imaging, linear regression is performed with a 24-sample window (about 4 mm) that is incremented one displacement sample for each strain estimate. The resulting algorithm displays streaming B-mode and strain images side-by-side at about seven frames per second and stores the full sequence of I-Q (analytic form of the RF) echo data at full system bus speed. The stored data, which were acquired at a higher frame rate than the real-time display, can then be online postprocessed with the same displacement algorithm or other algorithms (not reported here), the size and location of the subregion-of-interest (SROI) can be adjusted, the grey-scale mapping can be modified, etc., and the results displayed frame-by-frame or as a cine loop.

Although the additional degrees of freedom of motion allowed with freehand compression, compared with motorized compression, were expected to result in an increase in displacement estimate error variance, that variance is only slightly higher for freehand compression (Zhu and Hall 2002). Given that the contrast and resolution of the strain-imaging system do not depend on the method of tissue deformation, displacement estimate error variance (resulting in strain image noise) is the dominant image quality parameter that will differ with the two methods of tissue deformation. With equal applied strain, motorized and freehand compression have comparable strain image noise. However, the frame-to-frame strain is not constant with freehand compression (as described below). This results in frame-to-frame variability in strain image quality with freehand scanning.

Small (*e.g.*, 2.4-mm diameter) isoechoic spherical targets in a phantom are considerably easier to locate and scan freehand than with motorized compression. The size of spherical targets measured from the resulting strain images is very close to their true dimensions (both height and width, see Zhu and Hall 2002), so both linear and area measurements in strain images *in vivo* should be accurate.

The grey-scale mapping of these strain images conforms with the *de facto* standard of mapping pixels, representing small strains dark and large strains bright. Typically, a sinusoidal (freehand) compress/release cyclic deformation was used and the acquired data contained one or more complete cycles. At the top and bottom of the stroke, there is little motion and, occasionally, there were brief hesitations during the motion. A consequence of freehand scanning is that the frame-to-frame strain is not constant. To compensate for that variability in average strain, the grey-scale for individual strain images (in the sequence of B-mode and strain images) was automatically adjusted to minimize brightness flicker. With this scaling, strain images that had an average strain of less than 0.15% were set to black. These frames rarely occur, but are most common at the top and bottom of the cyclic compression. Frames with greater than 0.15% compression were encoded as follows:

$$s_e(k, l) = \text{round}\left(\frac{s(k, l) - s_{min}}{s_{max} - 0.05\,\dfrac{s_{max}}{s_{min}}}\right), \qquad (1)$$

where $s_e(k, l)$ is the encoded strain value at position (k, l), and s_{max} and s_{min} are the maximum and minimum strain values in the frame, and round() is a function that rounds to the nearest integer. After scaling, the results are encoded into an 8-bit display range. This simple scaling provides a reasonably constant strain image brightness through the compression cycle, in the absence of significant displacement estimation errors. Large displacement estimation errors sometimes occur and this automatic grey-scale mapping can be dominated by erroneous displacement estimates.

Patient scanning

All patients provided informed consent consistent with the protocol approved by the Human Subjects Committee (Institutional Review Board) at The University of Kansas Medical Center. Patient scans were performed in a manner consistent with a normal breast US examination; the breast was scanned with the patient (typically) in the supine position with her ipsilateral arm behind her head. When the breast lesion was located, SROI was chosen that would avoid inappropriate data (lungs, areas of lost transducer contact, etc.) and the transducer was pressed toward the chest wall at a steady rate in an effort to achieve about 1–1.5% compression frame-to-frame. Subregion selection also typically excluded the retromammary fat layer and the chest wall. The soft fat, the stiff muscle and the slipping boundary between these layers can also dominate the dynamic grey-scale mapping. In some cases, for example, when scanning lateral lesions in large (D-cup) breasts, the patient was rolled slightly to her contralateral side so that gravity would flatten the breast tissue in the region to be scanned. A small plate (approximately 45-mm wide, 90-mm long) was sometimes attached to the transducer body to extend the compression surface in an effort to provide a more uniform stress field and to control motion perpendicular to the image plane. The compress/release cycle was repeated for relatively large (> 10%) compression range, while watching the B-mode image. The compression motion was adjusted by changing the compression direction or patient position until there was nearly uniaxial compression with minimal elevation motion. With this achieved, the strain-imaging software was enabled to evaluate the quality of the sequence of strain images. If a large sequence ($\gtrsim$ 30 frames) of strain images had good image quality (relatively high contrast-to-noise ratio) and high frame-to-frame similarity, the data acquisition was frozen, the image sequence stored, and the cine feature of this software was used to review, postprocess and select images to record. If the compression rate was too slow, resulting in low frame-average strain, the interframe skip was adjusted to increase the strain between frame pairs used in displacement and strain estimation, as suggested by Lubinski et al. (1999). Representative results obtained when scanning a 3-mm cyst are shown in Fig. 1. The average strain per frame (Fig. 1b) suggests nearly ideal compression rate in this case. Consecutive frames were paired for displacement estimation when analyzing this sequence of data. The cumulative strain in the sequence (Fig. 1c), obtained by summing the strain in consecutive frames, demonstrates that about an 18% compression range was achieved in this study. The initial value on the ordinate axis in each plot was set to zero and (the frame-average) strain was accumulated (Fig. 1c) from that starting point. If, for example, there was a net compression of the tissue in the first frame pair, the initial average strain was negative and the first value on the cumulative frame plot was negative. Data acquisition was frozen by the operator when an acceptable image sequence was acquired. The starting and ending points of that sequence could be at any point in the cyclic motion. Therefore, the precompression at the starting point is a random value between the minimum and maximum precompression.

RESULTS

One of the most promising uses of strain imaging is differentiation among breast lesions. To date, we have successfully scanned 39 patients with over 175 patient scans (multiple lesions per patient, repeat visits, perpendicular scan planes, different transducers and THI). Data from only 29 of these patients are included in this study
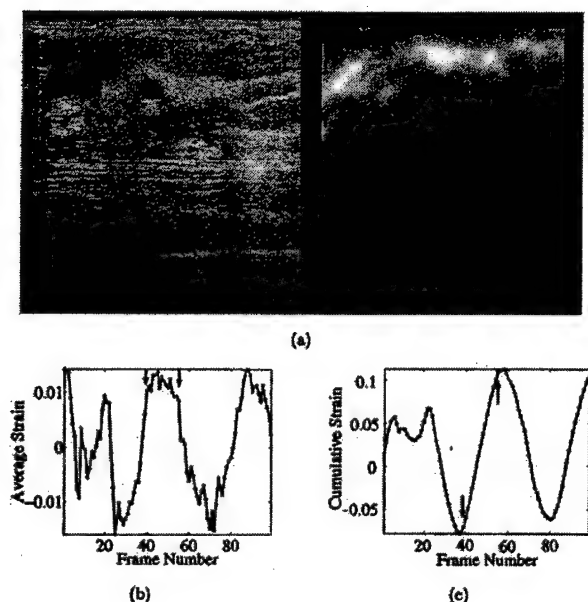
(a)

(b)   (c)

Fig. 1. Data obtained by freehand scanning of a breast cyst *in vivo*. (a) A B-mode and strain image pair obtained for frame 51 in the sequence. The white box in the B-mode image defines the ROI for strain imaging. (b) The average strain in the ROI; (c) the cumulative strain in the ROI. The arrows in (b) and (c) indicate that a sequence of frames was acquired with nearly equal average strain in each frame but with varying cumulative strain (precompression).

(a)

(b)

Fig. 2. Two image pairs from the same patient on repeat visits. The patient has a palpable fibroadenoma that measures about 16 mm $\times$ 11 mm. (a) The strain image acquired with the VFX13-5 array during the first visit, which is very similar to (b) that acquired with the 7.5L40 array 2 weeks later.

(data from patients with surgical scars or closely spaced lesions were excluded, as described below). Among these 29 patients, 19 fibroadenomas, 29 cysts and 7 carcinomas were included in this study. Ten of the fibroadenomas, at least five of the cysts and four of the carcinomas were palpable. All fibroadenomas were either pathologically proven or had been stable under radiological investigation for more than 1 year. All carcinomas were pathologically proven. Both simple and complex (hemorrhagic) cysts were included. Fibroadenomas, cysts and invasive ductal carcinomas have distinctive behavior in their strain image under cyclic compression, as detailed below.

One of the key tests was to show that strain images are reproducible, both within an image sequence and on repeat acquisitions. The question of reproducibility within an image sequence is addressed for each lesion type (fibroadenoma, cyst and invasive ductal carcinoma) below. Figure 2 shows results of repeating the freehand *in vivo* elasticity imaging on the same patient. A skilled sonographer can acquire a sufficiently similar B-mode image of an ROI with repeat scanning. However, obtaining a similar strain image requires that the ROI be found, and the direction of compression/release relative to the lesion and chest wall be the same in the two studies. No
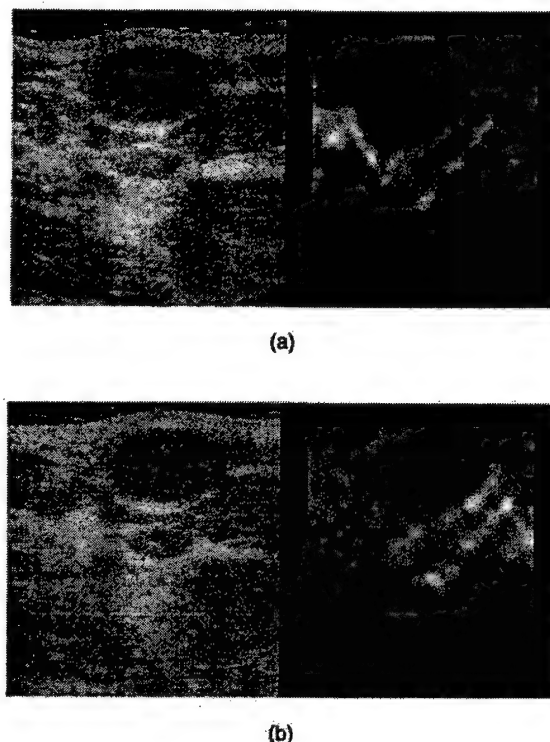
special effort was used to obtain similar images, but Fig. 2 demonstrates that the strain patterns in these images are very similar.

Too few independent samples of each lesion type have been observed to make strong statistical statements regarding each criterion described by Garra et al. (1997). The following descriptions state our qualitative observations to date, in the hope of guiding the scanning and image-evaluation techniques used by others in future studies. In particular, the automatic scaling of grey-scale values precludes quantitative statements of (and homogeneity of) relative stiffness.

A total of 37 B-mode and strain image sequences were acquired from 19 unique fibroadenomas among 9 patients. One of our most significant findings is that there was an obvious (subjective, visual) loss in strain image contrast for 14 of these 19 fibroadenomas (27 of 37 image sequences, 6 of 9 patients, average age 44 years). Fibroadenomas typically have negative contrast (are more stiff than their surroundings) at low precompression and lose contrast (stiffness becomes more like their surroundings) as they are compressed. An example of this is illustrated in Fig. 3. The largest negative contrast
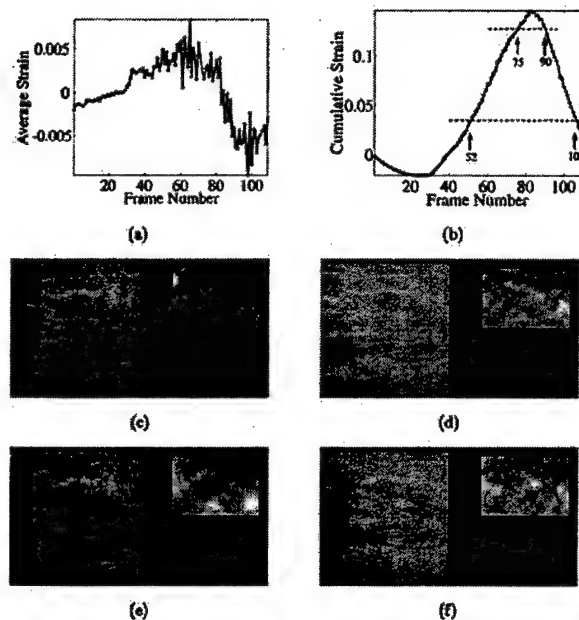
(a)

(b)

(c)

(d)

(e)

(f)

Fig. 3. Data obtained by freehand scanning of a fibroadenoma *in vivo*. (a) The average strain in the ROI for each frame suggests a slow compression rate. The interframe skip was increased to pair every fourth frame in analyzing this sequence of data. (b) The cumulative strain in the sequence shows that a 20% compression range was achieved. Images of fibroadenomas acquired with equivalent precompression [equivalent cumulative strain, frames (c) 75 and (e) 90, (d) 52 and (f) 106] are similar, but, because of the nonlinear stress-strain relationship of tissue, strain images acquired at different precompression can have significantly different contrast.
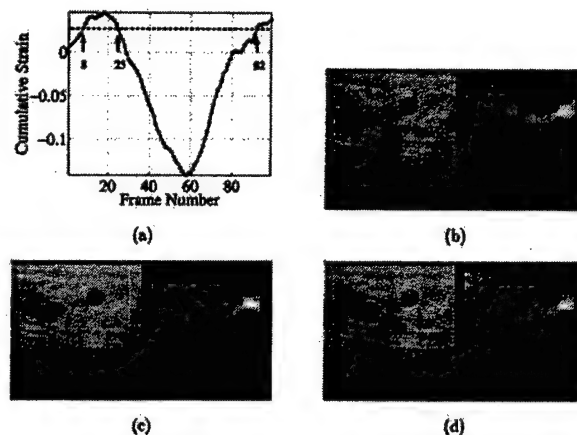

(a)

(b)

(c)

(d)

Fig. 4. Data obtained by freehand scanning of two breast cysts *in vivo*. (a) The cumulative strain in the sequence shows that a 20% compression range was achieved. Strain images of the interior of cysts, unlike those of fibroadenomas, are not necessarily similar when acquired with similar precompression (cumulative strain). (b), (c) and (d) Images from frames 8, 25 and 92, respectively, were acquired with similar precompression. Although strain images can vary smoothly from frame to frame, decorrelation of the signals within the cysts results in strain images that vary significantly over the compression cycle.

occurs with minimal precompression. Figure 3c and e shows that the transducer is barely in contact with the skin surface at this precompression. Comparing these with Fig. 3d and f demonstrates that images of fibroadenomas acquired within a sequence at equivalent precompression are very similar. However, as precompression changes, strain contrast changes (comparing Fig. 3c or e with d or f.

Both simple and complex cysts were included in this study, to investigate the possibility that fluid-filled cysts, regardless of "echogenicity," have a common behavior in cyclic strain images. The hope was that strain images might help to differentiate complex cysts from solid lesions that lack evidence of blood flow.

The frame-to-frame variability of strain images of cysts is more complicated than that observed with fibroadenomas. A total of 39 B-mode and strain image sequences were acquired from 29 unique cysts among 15 patients. A very soft bottom layer in the interior of the cyst was observed in 7 of 29 cysts (11 of 12 image sequences of those cysts). That layer might be due to a sediment inside the cystic fluid. Repositioning the patient

might have allowed us to confirm that conjecture, but that test was not performed. The interior echoes within the cysts rapidly decorrelate with compression. As a result, the apparent strain in the lesions varies with compression, but that compression-dependent strain image contrast is very different from that observed for fibroadenomas. If the incremental average strain from one strain image to the next is small ($< 0.5\%$), the strain image brightness (on a pixel-by-pixel basis) changes gradually, regardless of precompression. If the incremental average strain is not small ($\geq 1\%$), then the local brightness within the cyst varies rapidly and (seemingly) unpredictably. The typical behavior of the strain pattern in cysts is demonstrated (as well as can be with static images) in Fig. 4. Unlike the behavior observed with fibroadenomas, frames with equivalent precompression might have very different apparent strain within the cyst. Overall, a cyst can be either relatively stiff, as if it were a distended balloon, or relatively soft.

A total of 21 B-mode and strain image sequences were acquired from 7 unique carcinomas among 6 patients. All carcinomas studied so far were invasive ductal carcinomas and all but one were highly suspicious of carcinoma, based on mammogram and sonogram results. This is by far the most commonly diagnosed breast cancer. Relatively small lesions (≤ 2 cm) have high negative contrast (stiff) in a background of "normal" breast tissue, regardless of precompression. An example of this is shown in Fig. 5. The exception to this occurs for
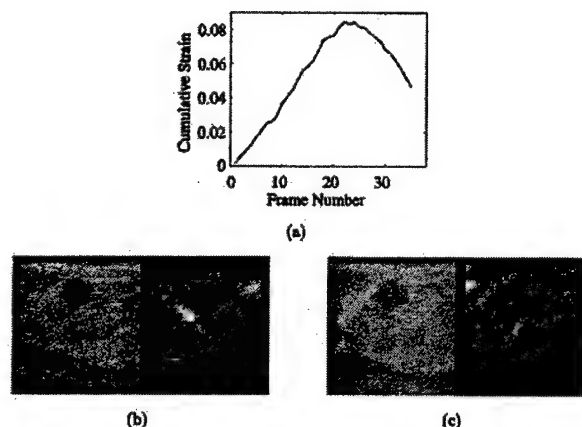
Fig. 5. Data obtained by freehand scanning of invasive ductal carcinoma *in vivo*. (a) The cumulative strain in the sequence shows that a 8% compression range was achieved. (b) Images in frame 4 acquired at low precompression, are very similar to (c) those in frame 18 acquired at much higher precompression. Some differences in the strain in "normal" surrounding tissue are seen, but vary smoothly from frame to frame.
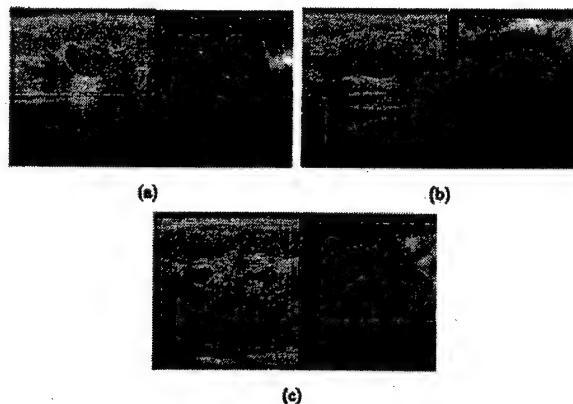

Fig. 6. B-mode and strain images of fibroadenomas with their perimeter traced in the B-mode image; that tracing also in the strain image for comparison. A fibroadenoma measuring (a) 71.4 mm^2 in B-mode and 75.0 mm^2 in strain, (b) 88.7 mm^2 in B-mode and 102 mm^2 in strain, (c) 27.2 mm^2 and 21.5 mm^2 in B-mode and 26.8 mm^2 and 21.7 mm^2 in strain, respectively. The B-mode tracing is a reasonably good approximation to that on the strain image.

very large lesions where little, if any, healthy tissue is included in the strain image.

One of the criteria that Garra et al. (1997) found to be most useful in differentiating between benign and malignant lesions was the relative size of the lesion in B-mode vs. strain images. To compare lesion size in the two imaging modalities, we transferred the I-Q echo data to an off-line computer for further analysis. The strain images were reprocessed using the same displacement estimation algorithm as that implemented on the Elegra. Off-line processing used a 16-sample (< 3 mm) window for strain estimation instead of the 24-sample window used on the Elegra (higher axial resolution). Movie loops of the side-by-side B-mode and strain image pairs (avi files) were created to view the motion of the lesion in the B-mode image and the resulting strain image. A representative frame was selected that showed the "typical" strain image for that lesion and the B-mode image was displayed, allowing the lesion boundary to be traced. The boundary in the B-mode image excluded the capsule of the lesion. The lesion width (and height) were estimated, based on the traced lesion perimeter, as the maximum dimension perpendicular (and parallel) to the acoustic beam. The tracing and measurement process was then repeated with the strain image from that same frame. The boundary traced in the strain image was the location of the steepest (visual) gradient in strain. High negative-contrast images were chosen for fibroadenomas. All tracings were performed by the first author, and most boundaries were very easily identified. In some cases, for example, in the atypical fibroadenoma shown in Fig. 3,

an experienced clinician assisted in tracing the boundary. Example images for a fibroadenoma, cysts and an invasive ductal carcinoma are shown in Figs. 6, 7 and 8.

It is intriguing to examine the relative size of these lesions, comparing their width, height and area as measured in B-mode and strain images. Figure 9a and b shows plots of the width and height of these three lesion types as measured in B-mode and strain images. Figure 9c shows plots of a similar comparison of the total area
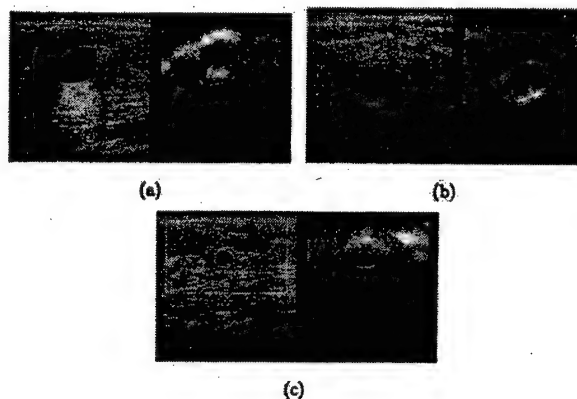

Fig. 7. B-mode and strain images of cysts with their perimeter traced in the B-mode image; that tracing also in the strain image for comparison. A cyst measuring (a) 139 mm^2 in B-mode and 145 mm^2 in strain, (b) 102 mm^2 in B-mode and 84.1 mm^2 in strain, (c) 30.3 mm^2 in B-mode and 32.5 mm^2 in strain. The B-mode tracing is a good approximation to that on the strain image, if the soft region at the bottom of the cyst, (a) and (b), were included.
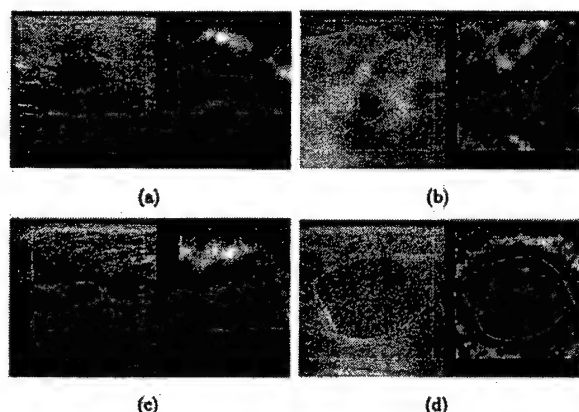
Fig. 8. B-mode and strain images of invasive ductal carcinomas with their perimeter traced in the B-mode image; that tracing also in the strain image for comparison. An invasive ductal carcinoma measuring (a) 96.1 mm^2 in B-mode and 170 mm^2 in strain, (b) 22.8 mm^2 in B-mode and 319 mm^2 in strain, (c) 48.7 mm^2 in B-mode and 170 mm^2 in strain, (d) 465 mm^2 in B-mode and at least 768 mm^2 in strain. The B-mode tracing is not representative of what would likely have been drawn on any of these strain images.

of the lesion in the two imaging modes. Table 1 shows that the width and height of benign lesions tend to be about the same size in B-mode and strain images and carcinomas are larger in strain images than in B-mode, as
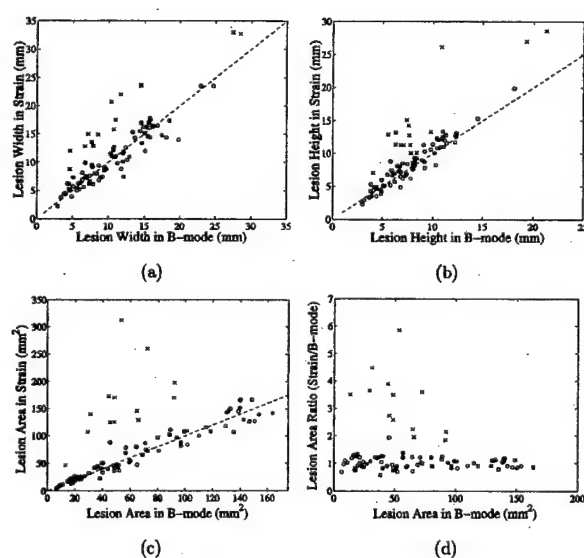
Fig. 9. Plots comparing the size of a lesion traced in the B-mode image vs. the same lesion traced in a representative strain image for (○) cysts, (□) fibroadenomas and (x) invasive ductal carcinomas. (a) The width and (b) height comparisons. (c) The areas for lesions less than 20-mm wide (in B-mode) are compared, and (d) the area ratio. The dashed line in (a)–(c) represents equal size measurement in both images.

observed by Garra et al. (1997), but the separation between benign lesion and carcinoma is larger when we use the lesion area.

In each of these examples, the study was performed on an isolated lesion. Although some data sets contained more than one lesion, those lesions were separated by at least one diameter of the largest lesion in the image. Measurements of individual lesions in clusters of lesions, most frequently observed in clusters of breast cysts, proved problematic in obtaining high-quality strain image sequences and in interpreting the motion. An example of this, shown in Fig. 10, shows that it might be more reasonable to study the cluster as a group instead of as individual lesions. When lesions are closely spaced, particularly when they share a common boundary, the motion due to compression can be quite complex, as observed in the B-mode image sequence, and the block-matching algorithm fails to track motion adequately. The block-matching algorithm assumes rigid body motion and does not accurately track significant rotation or shear motion. Further, our current system acquires data (effectively) in a plane, and significant motion perpendicular to the image plane is lost. A 3-D acquisition system would be required to track significant elevation motion. A higher-order algorithm, such as the deformable mesh (Zhu et al., 1998), would be required to track rotation and shear motion accurately. At this stage of strain image processing and interpretation, it is likely best to restrict the study to individual isolated lesions.

DISCUSSION

Real-time display of side-by-side B-mode and strain images is essential for guiding the manipulation of boundary conditions for the mechanics experiment that is strain imaging. Real-time feedback to the hand-eye coordination system allows the sonographer to manipulate the compression direction, force and rate to obtain high-quality sequences of strain images. The system employs standard linear-array transducers and requires no additional fixtures or remote data-acquisition or signal-processing hardware. It is fully integrated into the Elegra system. A small plate 9 cm × 4.5 cm is sometimes attached to the face of the transducer to extend the compression surface. This was most useful when scanning benign lesions that tended to move in elevation when compressed.

Our results show significantly different strain-image sequences for each lesion type studied. Although the three lesion types reported here do not include all those found in breasts, they represent the most common clinically observed breast lesions. It was found that, to appreciate the differences among lesion types, and to determine the "typical" strain image for a given lesion, it

Table 1. Results of measurements of the size of lesions in B-mode and strain images and the ratio of their size (strain/B-mode)

	Lesion type		
	Cyst	Fibroadenoma	IDC
B-mode			
Width (mm)	9.8 ± 5.3	11.8 ± 4.1	11.7 ± 7.2
Height (mm)	7.2 ± 3.4	8.4 ± 2.4	9.2 ± 4.8
Area (mm^2)	69.3 ± 72.2	81.9 ± 44.4	104 ± 135
Strain			
Width (mm)	9.8 ± 5.1	11.6 ± 4.1	18.6 ± 7.3
Height (mm)	7.6 ± 3.8	8.8 ± 2.7	14.8 ± 6.7
rea (mm^2)	72.8 ± 77.8	81.2 ± 44.6	236 ± 206
Ratio (strain/B-mode)			
Width	1.02 ± 0.16	1.00 ± 0.18	1.74 ± 0.36
Height	1.04 ± 0.16	1.07 ± 0.21	1.68 ± 0.36
Area	1.05 ± 0.24	1.00 ± 0.17	3.02 ± 1.19

Tabulated values are the mean $\pm$ the SD of the group. The size ratio for benign lesions is near unity, showing that these lesions typically have the same size in both imaging modalities. However, invasive ductal carcinomas (IDC) typically are 2 to 3 times as large in strain images than in B-mode images.

was necessary to observe a sequence of B-mode and strain images displayed side-by-side. With that sequence, a very reproducible determination of the lesion boundary could be obtained. Measurements of lesion dimension were then made and the results for lesion width are
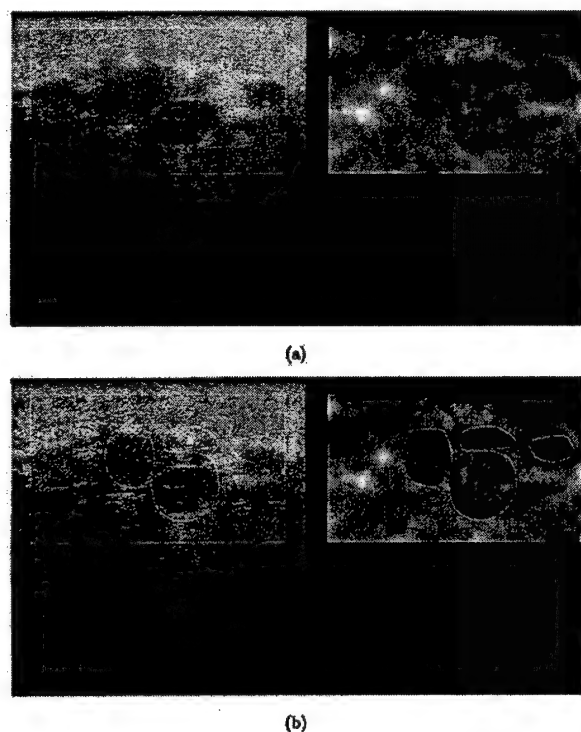

(a)

(b)

Fig. 10. B-mode and strain images of a cluster of breast cysts with their perimeter traced in the strain image; that tracing also in the B-mode image for comparison.

consistent with those reported by Garra et al. (1997). That report stated a lack of confidence in their measurements of lesion height. Our results with spherical targets in phantoms show that we can accurately measure lesion dimension in both height and width (Zhu and Hall 2002) and, therefore, we use lesion area as the criterion for comparing lesion size in B-mode and strain images.

The significant, but monotonic, change in strain contrast as a function of precompression appears to be unique to fibroadenomas so far in our experience. This contrast variation suggests that the stress-strain relationship for fibroadenoma does not parallel that of the surrounding tissue. Fibroadenomas that vary in strain contrast appear dark (stiffer) at low precompression and lose contrast (become relatively softer) at higher precompression. One possible explanation is that the stress-strain relationship for the surrounding tissue is more nonlinear than that of the fibroadenoma over the range that each are compressed in this technique. The average age of the women with fibroadenomas in this study was 44 years, and their dominant breast tissue type was subjectively judged to be fibroglandular from B-mode images. The data reported by Krouskop et al. (1998), demonstrate that both glandular tissue and (primarily) fibrous tissue, such as fibroadenoma, have nonlinear stress-strain relationships. When preloaded to 5% strain, fibrous tissue is about 3 times more stiff than glandular tissue. However, the appropriate comparison for our application is when both tissues have minimal preload and when glandular tissue is preloaded about 15% and fibrous tissue is preloaded some small fraction of that (because the less stiff tissues strain more when they are treated as a composite), and that composite is strained an average of about 1% for

data acquisition. Krouskop and colleagues did not report those results.

Garra et al. (1997) tested numerous criteria for discriminating benign from malignant breast lesions. The criterion that provided the greatest discrimination in their study was the comparison of lesion width measured in B-mode and strain images. They attributed that size difference to the desmoplasia that surrounds most malignant breast tumors (Tavassoli 1999). Desmoplasia is the excessive growth of fibrous connective tissue in the stroma surrounding the malignancy. That growth appears gray-white and feels very hard in gross pathology (Tavassoli 1999). Our study tested this criterion and extended the observation to a comparison of lesion area. The sequence of B-mode and strain image pairs allows the sonographer to select images representative of the "typical" strain image for a lesion. This ability, along with better determination of lesion boundary available by viewing a sequence of images, has likely improved the ability to measure true lesion size in strain imaging compared with the results reported by Garra et al. (1997). A study to estimate the intraobserver and interobserver variability in choosing the "typical" strain image and measuring lesion size is underway. That study is an essential part of determining the value of the relative size of lesions in B-mode and strain image pairs as a diagnostic criterion. The utility of elasticity imaging in differentiating (from benign growths) malignancies that lack desmoplasia has not been tested.

Garra et al. (1997) also found the brightness of the lesion in strain images to be a useful parameter, but our observation of the changing contrast with compression in fibroadenomas provides an improved description of the contrast of solid lesions in strain imaging. The change in strain image contrast with applied compression (*e.g.*, Fig. 3) demonstrates that observing only a single B-mode and strain image pair at an unknown precompression could be very misleading in the interpretation of the strain image data. A sequence of side-by-side B-mode and strain image pairs greatly adds to the ability to interpret strain images.

Numerous other criteria were tested by Garra et al. (1997), but demonstrated limited utility. As with their study, the current study is limited by the small number of patients and lesions included, and by the fact only one observer was involved in each report. A larger cohort of patients and a larger number of observers are needed to improve the statistical analysis of this technique. That effort will be the subject of a future report.

CONCLUSIONS

A new system for real-time imaging of tissue strain *in vivo* using freehand scanning is described and some of the results obtained with this system are reported. The new system provides real-time feedback, allowing the user to manipulate the conditions of tissue compression resulting in the ability to successfully scan all patients for which the technique was attempted. The strain images for various lesion types are unique, and the relative size of the lesions appears to be a useful criterion for discriminating benign from cancerous lesions. However, further testing will be needed to support this observation.

REFERENCES

Chaturvedi P, Insana MF, Hall TJ. 2-D companding for noise reduction in strain imaging. IEEE Trans Ultrason Ferroelec Freq Cont 1998a; 45(1):179–191.

Chaturvedi P, Insana MF, Hall TJ. Testing the limitations of 2-D companding for strain imaging using phantoms. IEEE Trans Ultrason Ferroelec Freq Cont 1998b;45(4):1022–1031.

Garra BS, Céspedes I, Ophir J, et al.. Elastography of the breast: Initial clinical results. Radiology 1997;202:79–86.

Hall TJ, Bilgen M, Insana MF, Krouskop TA. Phantom materials for elastography. IEEE Trans Ultrason Ferroelec Freq Cont 1997; 44(6):1355–1365.

Insana MF, Chaturvedi P, Hall TJ, Bilgen M. 3-D companding using linear arrays for improved strain imaging. Proc IEEE Ultrason Sympos 97CH36118. 1997;1435–1438.

Kallel F, Ophir J. A least-squares strain estimator for elastography. Ultrason Imaging 1997;10:195–208.

Krouskop TA, Wheeler TM, Kallel F, Garra BS, Hall TJ. The elastic moduli of breast and prostate tissues under compression. Ultrason Imaging 1998;20:260–274.

Lubinski MA, Emelianov SY, O'Donnell M. Adaptive strain estimation using retrospective processing. IEEE Trans Ultrason Ferroelec Freq Cont 1999;46(1):97–107.

Tavassoli FA. Pathology of the breast. New York: McGraw-Hill, 1999.

Zhu Y, Chaturvedi P, Insana M. Strain imaging with a deformable mesh. Ultrason Imaging 1998;21:127–146.

Zhu Y, Hall TJ. A modified block matching method for real-time freehand strain imaging. Ultrason Imaging 2002;24:161–176.

A Modified Block Matching Method for Real-Time Freehand Strain Imaging

Yanning Zhu and Timothy J. Hall

Department of Radiology
University of Kansas City Medical Center
3901 Rainbow Boulevard
Kansas City, KS 66216-7234
yzhu@kumc.edu

This manuscript reports a technical innovation that has been developed for real-time, freehand strain imaging. This work is based on a well-known block-matching algorithm with two significant modifications. First, since displacements are estimated row-by-row, displacement estimates from the previous row are used to predict the displacement estimates in the current row, thereby drastically reducing the search-region size and increasing computational efficiency. Second, a displacement error detection and correction method is developed to overcome the local tracking errors that may be more severe with freehand scanning and thereby improve the robustness of the algorithm. This algorithm has been implemented on a clinical ultrasound imaging system, and with real-time imaging feedback, long sequences of high quality strain images are observed using freehand compression. Displacement estimation errors with this method are experimentally measured and compared with results from simulation. We report only a specific implementation, with no comparison to other displacement estimators in the literature and no optimization of this specific technique. Images of tissue-mimicking phantoms with small spherical targets are used to test the ability to detect small lesions using the strain imaging technique. *In vivo* strain images of breast and thyroid are also shown.

KEY WORDS: Elasticity; elastography; palpation; tissue characterization; ultrasound.

1. INTRODUCTION

Ultrasonic strain imaging[1-9] is expected to have great potential for improving soft tissue diagnosis. The vast majority of the strain imaging work in the literature has focused on proof of concept and algorithm development. However, two major advances need to occur to make ultrasonic strain imaging a clinically useful tool. First, there is a need to acquire rf (or equivalent) echo data under clinically acceptable conditions with high patient throughput and low rescanning rates. Second, there is a need to further develop the clinical interpretation and significance of these results. In this work, we concentrate our effort on the first issue.

A skilled sonographer can acquire B-mode images with relative ease. Low noise strain images are more difficult to produce. Deformation of heterogeneous tissue can result in complex motion and echo signal decorrelation between the pre- and postcompression rf echo frame pair. Echo signal decorrelation leads to large strain estimation errors. Most strain imaging techniques in the literature produce strain images in two steps. First, the rf echo data is acquired by either digitizing the output from a modified clinical ultrasound system or directly downloading the rf data from the system if it is available. Second, the stored rf echo frames are processed off-line to produce strain images. With off-line processing, it is difficult to know, while scanning, whether the acquired echo frame pairs are coherent enough for strain estimation. Hence, off-line data processing is not as efficient for clinical utilization as real-time imaging.

A more clinically desirable system would be capable of displaying B-mode images and strain images side-by-side in real-time. Real-time strain imaging can help clinicians determine whether satisfactory strain images are being acquired and can also help clinicians improve their freehand compression techniques. With real-time feedback, clinicians can adjust the compression speed and angle to compensate for irregular motion (large-scale rotation or lateral or elevational translation). Hence, real-time strain imaging increases data acquisition efficiency.

Another important aspect for clinical utilization of strain imaging is the technique used to deform the soft tissue. Most phantom experiments in the literature used motorized compression fixtures. These devices are cumbersome, limit the locations that strain imaging can be applied, and are time consuming to incorporate.[8] Thus freehand scanning is desirable. Doyley et al have shown that, compared with motorized compression, the penalty for freehand scanning is small with tissue mimicking phantoms.[6] Hiltawsky et al have shown that strain imaging of breast tissues with freehand compression is feasible.[7]

Lorenz et al have developed a real-time freehand strain imaging system that is external to the ultrasound imaging platform.[9] Some encouraging results are obtained for prostate applications using the system. In their system, a modified 1-D cross-correlation algorithm is used for displacement estimation. It performs well with small strains (much less than 1%) since the motion is tracked only in one dimension. It is well-known in the literature that the contrast-to-noise ratio in strain images increases with the applied strain (below about 5%).[5,10] Hence, larger single step compression is desirable.

In our work, strain-imaging software is implemented within a high-end commercial ultrasonic imaging platform (SONOLINE Elegra, Siemens Medical Solutions, Ultrasound Group). The strain images are displayed in real-time, side-by-side with the regular B-mode images. For the purpose of estimating displacement with relatively large applied strain (1~2% for *in vivo* tissue and up to 5% for tissue mimicking phantoms), a modified 2-D block matching algorithm was selected. Block matching (template matching) algorithms are widely used in image processing applications for tracking motion. The most notable application is video compression standards such as MPEG. Its utilization in ultrasonic imaging was first reported by Trahey et al for blood flow estimation.[11]

The purpose of this paper is to report our work in developing a real-time freehand strain imaging technique. We report only a specific implementation with no comparison to other displacement estimators in the literature and no optimization of this specific technique.

In the next section, we will introduce our displacement and strain estimation algorithms. In the results section, we provide performance measures of this algorithm in the form of displacement estimation error and spatial resolution with tissue-mimicking phantoms. We also provide examples of *in vivo* strain images obtained from this system. The conclusion section summarizes this work.

METHODS

1. Standard block matching

The 2-D block matching algorithm computes a sum-squared difference (SSD) between pre- and postcompression rf frames for a rectangular kernel over a search region as follows:

$$SSD(u,v) = \sum_{i=-(K_1-1)/2}^{(K_1-1)/2} \sum_{j=-(K_2-1)/2}^{(K_2-1)/2} \left[r_1(I+i, J+j) - r_2(I+i+u, J+j+v) \right]^2 \tag{1}$$
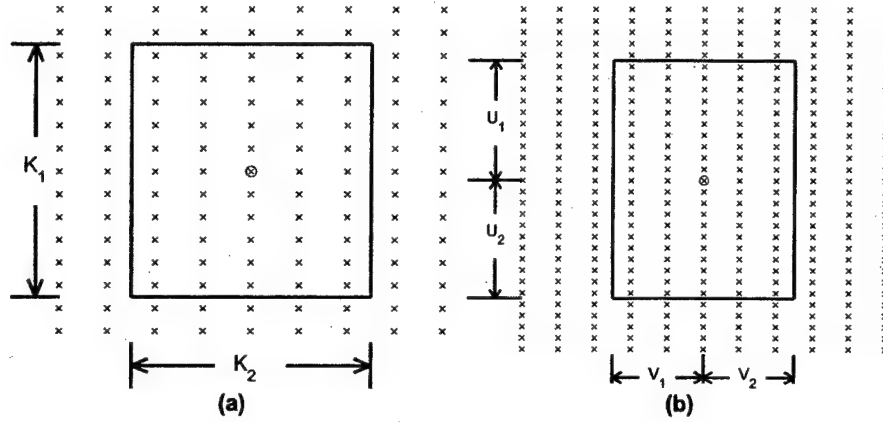
FIG. 1 Illustration of a kernel and search region. (a) Illustration of a kernel. (b) The search region defining the range of locations of kernel centers. Each 'x' represents an rf data sample. A kernel is composed of several adjacent rf A-lines (5 in our implementation) with several rf samples (11 in our implementation) per line in the pre-compression rf field. The search region defines the range of possible locations of the center of the kernel in the postcompression rf field.

where r_1 and r_2 are pre- and postcompression rf echo fields, respectively; I and J are axial and lateral rf sample indices for the location where the displacement is estimated; u and v define search locations in a search region; and K_1 and K_2 are kernel height and width, respectively. The kernel size is empirically chosen to be 11 axial samples by 5 A-lines ($K_1 = 11$ and $K_2 = 5$) for a 7.5MHz transducer, or approximately half the area of the pulse-echo point-spread function. A pictorial illustration of the kernel and search region is shown in figure 1. For each location (I,J) at which the displacement is estimated, the SSD function is computed for every rf sample location that is within the search region (range of kernel centers) defined by $-U_1 = u = U_2$ and $-V_1 = v = V_2$, where U_1, U_2, V_1, and V_2 represent search up, down, left and right distances, respectively, as shown in figure 1. The search-region height and width are $U = U_1 + U_2 + 1$ and $V = V_1 + V_2 + 1$, respectively. The displacement distribution usually does not need to be estimated as finely as rf samples. We use k and l as axial and lateral indices of displacement estimates. The location, $(u_{min}, v_{min}) = (d_1(k,l), d_2(k,l))$, at which the minimum SSD is found is considered to be the displaced position of the kernel. Hence, $d_1(k,l)$ and $d_2(k,l)$ are axial and lateral displacement estimates, respectively.

The computational cost of the block-matching algorithm to produce one displacement estimate is mainly determined by the kernel and the search-region sizes. In fact, to estimate one displacement vector, the subtraction-square-accumulation operation defined in Eq. (1) needs to be performed $K_1 K_2 UV$ times. The computed SSD values are then compared UV times to find the minimum. Since the kernel size is usually predefined and fixed, the task of reducing the computational cost of the block matching algorithm is to find a way to minimize U and V.

It is straightforward to estimate the computational load of the typical implementation of SSD-based block matching. In this case, U and V are selected to be sufficiently large to guarantee that the displacement vector is enclosed by the search region. Assume the size of each rf echo field is 40 mm by 40 mm (typical in our experiments) and the maximum applied strain is 5%. The associated axial displacement magnitude is then 0.05 x 40 mm = 2 mm. The axial sampling frequency for our study is 36 MHz, so the maximum axial displacement magnitude is about 94 samples. Assuming uniaxial compression of an incompressible medium, the to-

tal lateral strain is at most 5% (assuming no elevational expansion). However, it is difficult to accurately estimate the maximum lateral displacement magnitude since we do not know the location of the center of the compression (location where lateral displacement is zero). If we assume the center of the compression occurs at the middle of the data field, the maximum lateral displacement magnitude is 0.05 x 20 mm = 1 mm. Given that the rf echo field usually consists of 200 A-lines, the maximum lateral displacement magnitude is about 5 A-lines. With these assumptions, the search-region size can be chosen as 94x2+1 by 5x2+1 or $UV=$ 189 x 11=2079.

2. Search region reduction

The size of the search region can be minimized by using prior knowledge. The axial and lateral strain are defined by the following partial differential equations

$$s_1(k,l) = \frac{\partial d_1(k,l)}{\partial x_1},$$

$$s_2(k,l) = \frac{\partial d_2(k,l)}{x_2}. \tag{2}$$

In the sampled space, the axial and lateral strain can usually be approximated by the following difference equations

$$s_1(k,l) = \frac{d_1(k,l) - d_1(k-1,l)}{x_1(k,l) - x_1(k-1,l)},$$

$$s_2(k,l) = \frac{d_2(k,l) - d_2(k,l-1)}{x_2(k,l) - x_2(k,l-1)}, \tag{3}$$

where $x_1(k,l)$ and $x_2(k,l)$ are the axial and lateral coordinates of the location of the displacement estimate (k,l), respectively; k-1 and l-1 represent the indices of adjacent displacement estimates relative to k and l. The following inequalities can be derived from Eq. (3)

$$|d_1(k,l) - d_1(k-1,l)| \le S_1 |x_1(k,l) - x_1(k-1,l)|,$$

$$|d_2(k,l) - d_2(k,l-1)| \le S_2 |x_2(k,l) - x_2(k,l-1)|, \tag{4}$$

where S_1 and S_2 are the maximum (allowed) local strain magnitudes in the axial and lateral directions, respectively. The spatial separations of displacement estimates are $x_1(k,l)$-$x_1(k$-1$,l)$ and $x_2(k,l)$-$x_2(k,l$-1), respectively. For real-time strain imaging, the axial separation is 16 samples and the lateral is 2 A-lines. Experiments in phantoms have demonstrated that displacement can be estimated when the applied strain is greater than 5%. However, strain contrast-to-noise ratio decreases rapidly for applied strain in excess of 5%.[10] Our *in vivo* experiments have shown that the displacement can be successfully estimated for applied strain up to about 2%. Noise dominates in the displacement estimates when the applied strain is more than 2% for *in vivo* tissues. We can use this as prior knowledge to limit the ex-
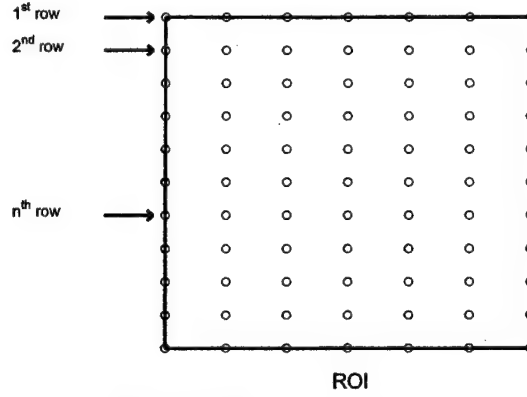
FIG. 2 Illustration of an ROI. Grid points (circles) are locations at which the displacement distribution is estimated. Each grid point coincides with an rf sample location, but the displacement distribution is less densely sampled than the rf echo signals. In our real-time implementation, grid point separations are 16 samples in the axial direction and 2 A-lines in the lateral direction.

tent of the search region. Note that if the displacement difference between adjacent estimates is 1 sample in the axial direction and 1 A-line in the lateral direction, then Inequalities (4) give us

$$S_1 \leq 6.25\%, \tag{5}$$
$$S_2 \leq 50\%.$$

The maximum local strain we intend to estimate is less than 6.25%. If we estimate displacement in the order of increasing k and l (row by row and from left to right), then the displacement that is currently being estimated is within a 3 sample by 3 sample block centered at the location predicted by the previously estimated displacement (one sample in each direction away from our best guess). In other words, we can reduce the search-region size to 3 by 3 if we use the previous estimates to predict where to search for adjacent estimates. Note that we allow larger local strain than the total strain since the strain distribution is not uniform. With the search region reduction, $UV=3\times3=9$. Compared to typical block matching, the new method reduces the computational load by a factor of $2079/9 = 231$.

In implementing the reduced search-region block-matching strategy, we first manually select a region of interest (ROI) which is a subregion of the field of view. For example, in breast imaging, we select an ROI that excludes undesired echo regions. The locations at which the displacement is estimated are determined by grid points with equal spacing starting at the upper-left corner of the ROI, as shown in figure 2. The displacement is then estimated in two stages. In the first stage, the displacement of the first row of grid points, as shown in figure 2, is estimated using Eq. (1). Since there is no prior knowledge of the displacement distribution, a large search region is used. The size of the search region at this stage is determined by the following equations.

$$U_1 = U_2 = CEIL(S_1 x_1(0,0)), \tag{6}$$
$$V_1 = V_2 = CEIL(S_1 A),$$

where *CEIL* is the function that rounds to the next larger integer; $x_1(0,0)$ is the depth of the top of the ROI; A is the number of A-lines in the field of view. The search region created by Eq. (6) is large enough to enclose the true displacements as long as the applied strain does not exceed S_1.

In the second stage, the displacement is estimated from the top of the ROI to the bottom, row by row. Displacement estimates obtained in the first row are used to predict displacements in lower rows, and the search region in this stage is reduced to 3 rf samples by 3 A-lines using the equation

$$SSD(u,v) = \sum_{i=-(K_1-1)/2}^{(K_1-1)/2} \sum_{j=-(K_2-1)/2}^{(K_2-1)/2} [r_1(I+i, J+j) - \tag{7}$$
$$r_2(I + d_1(k-1,l) + i + u, J + d_2(k-1,l) + j + v)]^2 .$$

In Eq. (7), a search center, $(I+d_1(k-1, l), J+d_2(k-1, l))$, is used to guide the search. In other words, when we do not have any knowledge of the displacement distribution, the search center is (I, J). After a row (or rows) of the displacement distribution is estimated, that information can be used to guide the search at neighboring locations and allows the use of a small search region. Note from Inequalities 4 that it is logical to set the search-region center to be $(I+d_1(k-1, l), J+d_2(k, l-1))$. However, since the difference between $d_2(k-1, l)$ and $d_2(k, l-1)$ is small, the search-region center is selected as $(I+d_1(k-1, l), J+d_2(k-1, l))$ to simplify the algorithm.

The computational load can be further reduced by performing the 2-D (3 by 3 search region) search sparsely. Lateral displacement does not need to be estimated as densely as axial displacement because lateral sample spacing is much greater than axial. For real-time imaging, we can apply 3 by 3 search regions every 5 rows and use the lateral displacement estimates to guide the next 4 rows of displacement estimation. These 4 rows of displacement estimates are obtained using a 3 by 1 search region (1-D search). An even more aggressive strategy is to only estimate the lateral displacement for the first row and use this to predict the lateral displacement for the remaining rows and limit the 2-D search to the first row only.

3. Displacement error detection and correction

Two types of displacement estimation errors can occur. It is common for large errors to appear in the first row. This is due to the inherent pre- and postcompression rf waveform decorrelation and periodic ambiguities ('false-peak errors') associated with large search regions. Figure 3 shows an example of this type of error.

The second type of error results from correlations in displacement estimates when using predicted displacements to reduce the search-region size. Errors in displacement estimates propagate if they are large enough that the defined search regions do not enclose true displacements. When tissue is compressed, large and irregular local deformation can occur. This may cause local decorrelation in the recorded rf frame pair. Figure 4 shows an example of this type of error. The displacement estimation errors tend to accumulate when estimating displacement near those local regions.

A segmentation method that can detect and correct large errors is needed to overcome these problems. Each row of the displacement estimates is checked for errors in three steps. In the first step, from left to right within a row, the displacement estimates are segmented. Segmentation occurs if the difference between adjacent displacement estimates is larger than 2 samples. The result of this step for the displacement curve shown in figure 3 (row
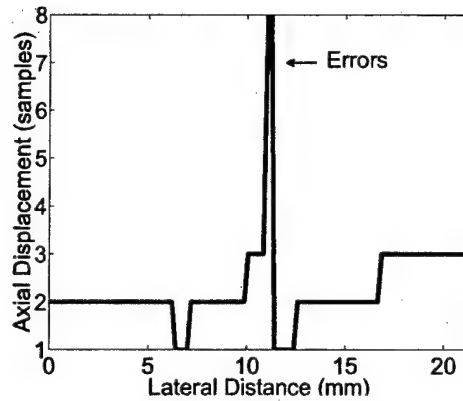
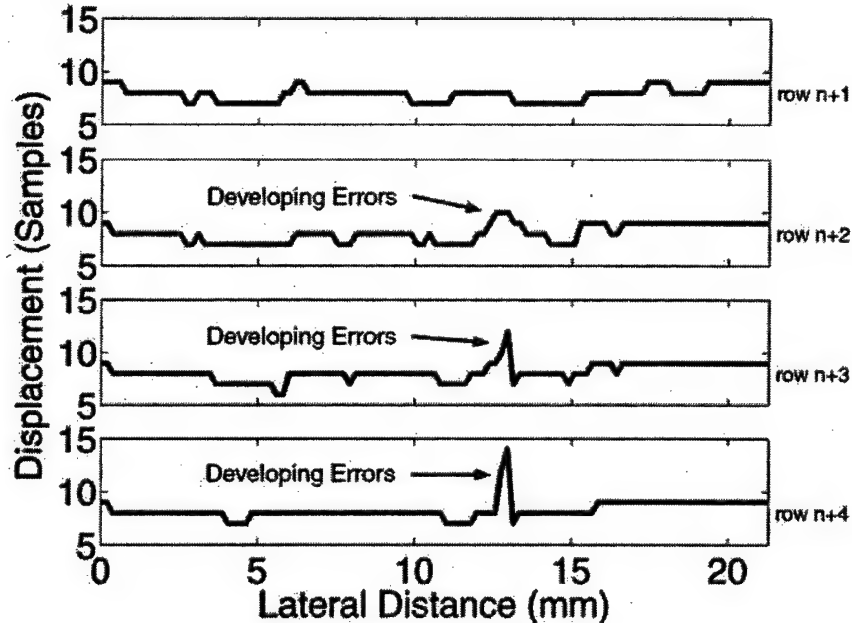FIG. 3 Example of errors in the first row displacement estimates.

FIG. 4 Example of errors in consecutive rows with a 3x3 search region.

n+4) is shown in figure 5(a) where the displacement estimates are segmented into three groups. In the second step, groups that are not adjacent are merged if the difference of displacement estimates between two nearest end points of the two groups is smaller than a threshold (3 samples in this case). For the example displacement curve, group 3 is merged into group 1. In the last step, the group that has the largest number of displacement estimates ('members', group 1 in this example) is marked as the 'correct' group of displacement estimates and all remaining groups are marked as errors. In the error correction stage, the displacement values of the error groups are then discarded and replaced by linearly interpolating values from the correct group. Figure 5(b) shows the displacement curve after error correction.
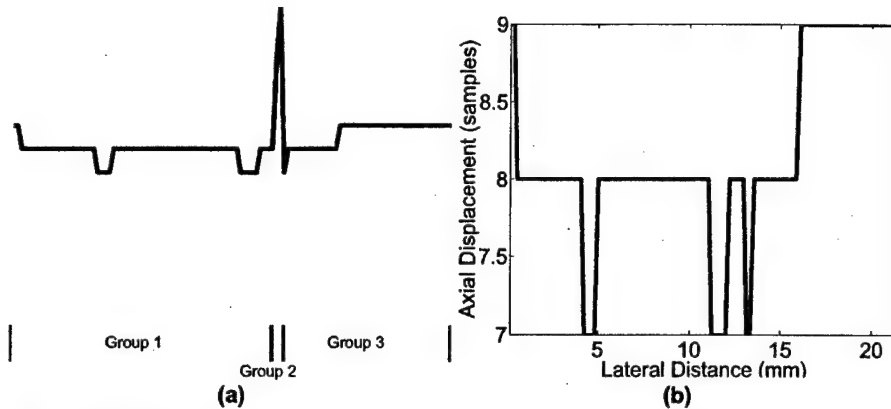
FIG. 5 Demonstration of error detection and correction. (a) Groups that are generated after initial segmentation. This displacement curve is the same as row $n+4$ in figure 4. (b) Displacement curve after error correction with the segmentation method.
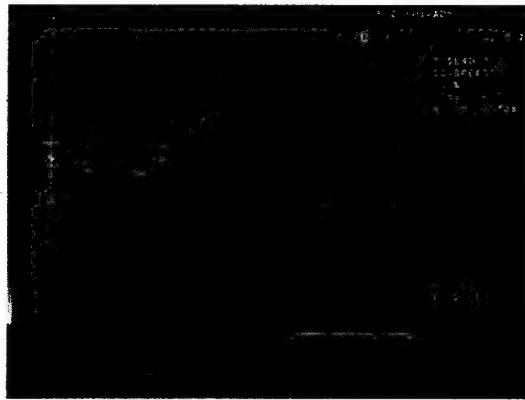

FIG. 6 Example of B-mode and strain images displayed side-by-side on an Elegra monitor during patient scanning.

Tests with *in vivo* data have shown that the error detection and correction process does not need to be applied to every row of displacement estimates. Displacement errors build up gradually since the small search region prevents large displacement deviations between adjacent rows. Errors are more apparent and easier to detect after the displacement estimation process progresses several rows. With this observation, we apply the error detection and correction process once every 5 rows. For each detected error, all 5 displacement estimates are replaced by the interpolated values.

4. Subsample accuracy displacement estimation

The displacement distribution that is estimated using this modified block matching algorithm has integer sample accuracy. With 36 MHz sampling and the strain estimation method described below, we find in phantom experiments that when the total applied strain is larger than 2%, this accuracy is adequate for creating low noise strain images. However, when the total applied strain is smaller than 2%, obvious strain artifacts can be seen in the image.[12,13] There are two ways of alleviating this problem. One way is to interpolate recorded rf frames
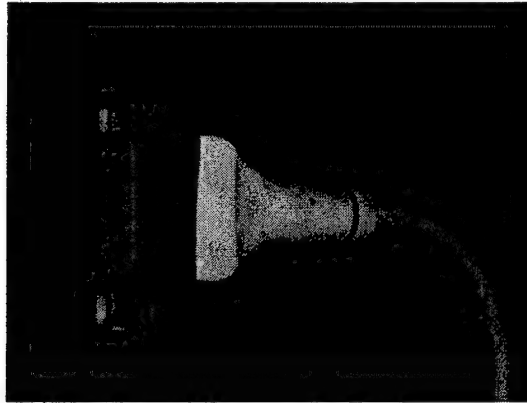
FIG. 7 Photograph of a transducer with the compressor plate mounted.

to higher sampling frequencies. This will increase the computational cost tremendously since interpolation requires computation and the kernel and search-region sizes must be increased. The alternative method, used in our implementation, is to quadratically interpolate the SSD values around the minimum to obtain sub-sample accuracy in displacement estimates. With this added processing, the strain artifacts are not severe when the applied strain is more than 0.2%.

5. Strain estimation

The axial strain is defined as the spatial derivative of the axial displacement, and there are several methods to estimate this derivative. The simplest methods are forward, backward, and center differences where only two data points are used. Estimating derivatives using only two data points requires low noise in displacement estimates. Since a relatively small kernel is used to estimate displacement, the noise in the displacement is too high to use these methods. However, axial strain can be estimated using a low order polynomial curve fitting method,[14] and we have implemented a linear regression strain estimator. In addition, this method provides the ability to trade off spatial resolution for increased smoothness of strain images. The strain images have better spatial resolution, but more noise, if shorter segments of displacement estimates are used in linear regression. The strain images are visually well balanced in smoothness and spatial resolution if the linear window length is set between 2-3 mm for a 7.5 MHz transducer.

IMPLEMENTATION

We have implemented the modified block matching algorithm on the Siemens Sonoline Elegra. The strain imaging software is an application that resides in the Elegra. The real-time beamformed I-Q (analytical representation of the rf signal[15]) frames are passed to a digital signal processor subsystem. That subsystem houses two Texas Instruments TMS-320C80 MVP processors that execute the software. An I-Q frame pair is used for displacement and strain estimation. The first frame is also envelope detected and a B-mode image is formed. Then, both B-mode and strain images are displayed side-by-side on the Elegra's monitor as shown in figure 6. The strain image corresponds to a region of interest (ROI) marked by the white-outlined rectangular subregion on the B-mode image. A user interface
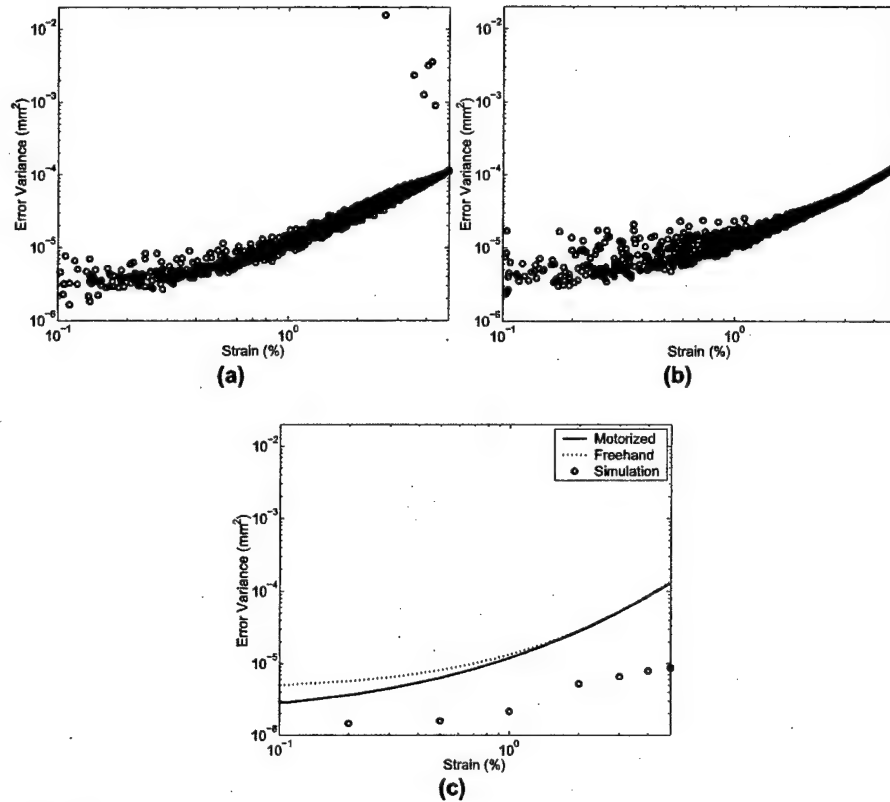
FIG. 8 Plots of the variance in displacement estimate errors for experimental and simulated data. (a) Motorized compression. (b) Freehand compression. (c) Curve-fits for experimental data with simulated data. In (c), the solid and dotted curves represent results obtained from motorized and freehand compression, respectively; circles are data obtained from simulation.

allows the adjustment of the size and location of the ROI, the separation (in the data stream) between I-Q frames used to estimate strain, and some of the strain visualization parameters such as strain to gray-scale mapping, etc. This software is capable of displaying the side-by-side images at about 7 frames/second.

With this system, strain imaging is performed in three stages. In the setup stage, the sonographer locates the lesion and selects the ROI in which the strain is estimated and displayed. Then, by pushing a button, the software enters the real-time side-by-side display mode. The user starts the compress-release cycle. If the user finds an image sequence that is of interest, she can freeze the data acquisition. A cine-mode allows the user to browse each frame or loop through a selected set of frames for a more careful study of the acquired data.

Tissue deformation is generated by cyclic motion of the transducer (i.e., compressing and releasing the body surface). A small (4.5 cm x 9 cm) compressor plate can be mounted to the face of the transducer to enlarge the compression surface and produce a more uniform stress field[16]. A picture of the transducer with a mounted compressor plate is shown in figure 7. Krouskop et al[17] have shown that if the cyclic motion is approximately 1Hz, then the breast tissue components behave as elastic materials (i.e., the viscous effects are negligible). Hence, during data acquisition, cyclic deformation of about 1Hz is attempted.

Experiments have shown that 7/s frame rate is sufficient for a sonographer to scan free-hand and control the compression motion of the transducer to compensate for undesirable lateral and elevational motion. No additional motion restricting device is necessary. However, successfully acquiring strain image data is not trivial. The sonographer needs to understand that the information being extracted is mechanical in nature and that the major challenge in strain image scanning is to minimize the rf waveform decorrelation.

Note that most of the parameters involved in the processing that generates strain estimates have not been optimized. These parameters include the kernel size used in the block-matching algorithm and the window length used in the moving linear regression algorithm that estimates strain from the displacement distribution. The optimization will be performed in our future work.

RESULTS

All data sets shown in this section were acquired using the system described above. A 7.5L40 linear array transducer (pulsed at 7.2MHz) was used in our data acquisition. The field of view was 40 mm x 40 mm. The system performance is studied in terms of basic image quality parameters. Reported here are representative measurements of noise and resolution. More detailed investigations into these topics will follow in future work after the processing parameters are optimized.

1. Displacement estimation error

The variance of the error in the displacement estimates was measured using a uniform gelatin phantom to produce a predictable displacement distribution. Both motorized compression and freehand compression were used in order to compare the variance of displacement errors with each of these methods. The motorized compression (a laboratory system[10]) used a large compression plate that covered the entire upper surface of the free-standing gelatin block (10 cm x 10 cm x 7 cm (WxDxH), no additional fixtures). The motor was programmed to produce a sinusoidal compression of 20% at 0.4 Hz. Freehand scanning was performed with the compressor plate shown in figure 7 and the compression was intended to replicate that of motorized compression. The separation between I-Q frame pairs, called the skip number and used for strain image formation, was adjusted to achieve a wide range of frame-average strains from these data sets.

The acquired data sets were processed off-line using an algorithm identical to that programmed on the Elegra. Since the phantom had uniform stiffness, the displacement curve along the compression direction should be a straight line (strain is constant over the entire field of view). Linear regression was applied to the estimated displacement curve along each A-line in the region of interest to generate the best-fit displacement curve. This line was then considered to be the true displacement. The displacement error was calculated as the difference between estimates and the fitted lines. The corresponding strain was calculated by averaging over strain estimates for all A-lines in the ROI.

We also simulated rf frame pairs for the medium with uniform stiffness.[5] The scanning pulse, sampled at 36 MHz, had 7.2 MHz center frequency, a -6 dB bandwidth of 40% and a Gaussian lateral profile with -6 dB beam-width of 400 μm and beam spacing of 200 μm. These parameters closely simulated the beam profile produced by the Elegra 7.5L40 probe. The simulated compressions resulted in applied strains of 0.2, 0.5, 1, 2, 3, 4 and 5%. For each compression, 30 rf frame pairs were generated and the modified block-matching algorithm
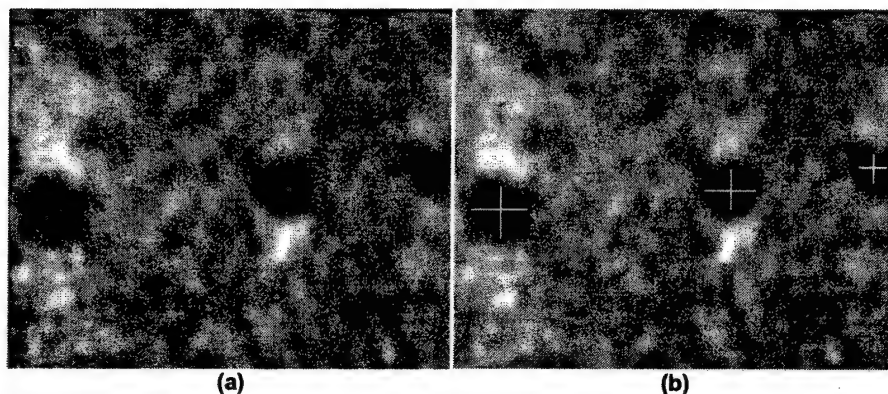
FIG. 9 Strain image (a) of a phantom with spherical targets. The average strain is 2.5%. The size measurements, shown in (b), are accurate, as detailed in table 1.

was used for displacement estimation. The displacement estimates were compared with the known true displacements to calculate the variance of the displacement estimation error.

Figure 8 shows the variance of the displacement estimation error versus the estimated applied strain. In figure 8(a) and (b) (motorized and freehand compression, respectively) the first 50 frames in the collected rf data sequences were used as precompression data fields. The skip number was varied from 1 to 15 for motorized compression and from 1 to 25 for freehand compression to achieve strains ranging from 0.1% to 5%. There were a total of 725 strain and variance measurements for motorized compression and 1250 measurements for freehand compression. In figure 8(a), there are 6 measurements with high displacement estimation error at relatively high strain. These are the cases where the error detection and correction method failed due to excessive noise in the first row displacement estimates.

Displacement error variance estimates for motorized and freehand compression were fit to a second degree polynomial in log-log space to generate representative curves for each data set and those curves were plotted in figure 8(c). Note that the 6 measurements for motorized compression with high error variance were excluded when curve fitting. The circles in figure 8(c) are displacement error variance measurements obtained from the simulation. The standard deviations of the error variance measurements for simulation are so small that they are not plotted (they would not be visible if plotted).

As seen in figure 8(c), the displacement error variance curve is relatively flat for strain less than 1%. This is likely due to the fixed displacement error produced by the quadratic interpolation.[13] The displacement estimate error variance for experimental data increases with the applied strain faster than the results obtained from simulation. This is likely due to elevational motion resulting from compressing the free-standing gel block (plane stress conditions), whereas the simulated data employed plane strain conditions (no elevational motion). Comparable performance is observed with motorized and freehand compression. Although motorized compression generally has slightly lower displacement errors, the benefit associated with freehand scanning offsets the small improvement in displacement estimate errors.

2. Small lesion detection

Gelatin phantoms with spherical targets that were three times stiffer than the background[18] were used to test the strain imaging system performance with small targets. The strain image (acquired with 2.5% compression) shown in figure 9(a) contains three targets (4.0 mm, 3.2

TABLE 1 Measured target size in millimeters.

	Leftmost target	Middle target	Rightmost target
Height (axial)	4.1	3.1	2.3
Width (lateral)	4.0	3.4	2.3
Actual diameter	4.0	3.2	2.4
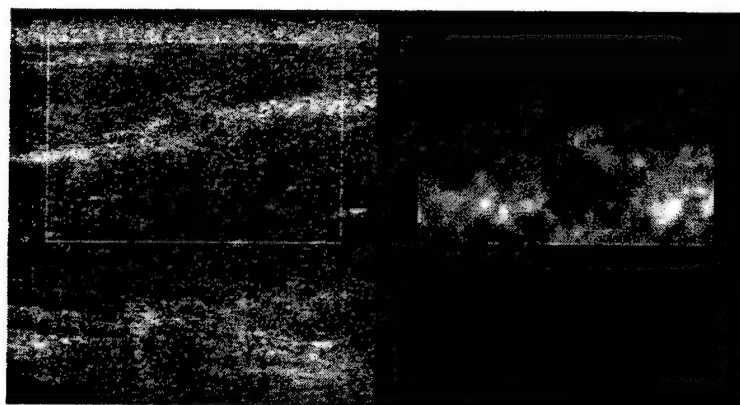
FIG. 10 Strain image of a 3 mm x 3 mm *in vivo* cyst in breast.

mm and 2.4 mm diameter, respectively). The apparent size of these targets was measured in the strain image in both axial and lateral directions. Figure 9(b) shows line segments that correspond to the width and height for each target and table 1 shows the measured sizes. These results suggest that spherical targets as small as 2.4 mm diameter can be accurately measured in both the lateral and axial dimensions.

3. *In vivo* strain images

Real-time freehand strain imaging has also been performed on *in vivo* tissues. The images, shown below, demonstrate that these strain images have reasonably low noise and high contrast.

Figure 10 shows an *in vivo* breast cyst that is about 3 mm x 3 mm. The visibility of the cyst in the strain image confirms our phantom results that lesions of a few millimeters in diameter can be detected in the strain images. The exact reason that the fluid filled cyst appears stiffer than the background is unknown. A reasonable hypothesis is that the cyst fluid is bounded by a distended capsule and appears stiff much like an air-filled balloon feels stiff.

Figure 11 shows an *in vivo* breast carcinoma. The apparent size of the tumor is much larger in the strain image (about twice as big) than in the B-mode image. This is consistent with the findings of Garra et al.[8]

Figure 12 shows an *in vivo* thyroid strain image. There is a nodule inside the thyroid, seen in both B-mode and strain images. The tissue structures and therefore the boundary conditions around the thyroid are very different from the breast, and in both cases compression induced motion is complex. However, with real-time feedback, the sonographer can manipulate the compression technique and obtain strain images. A problem in strain imaging of the thyroid is that the trachea and major blood vessels are often included in the field of view. Since
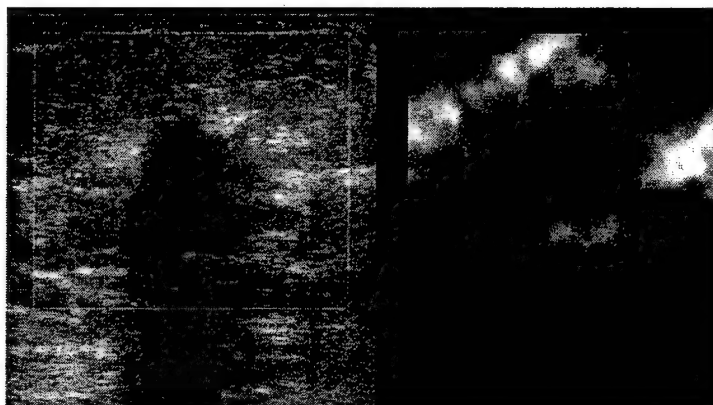
ZHU AND HALL

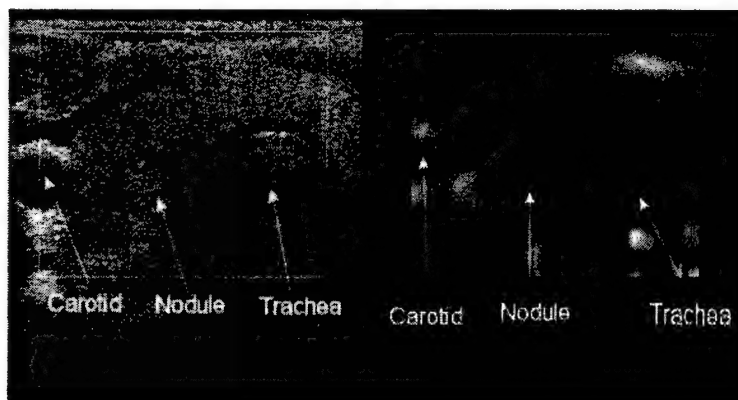FIG. 11 Strain image of an *in vivo* breast carcinoma.

FIG. 12 Strain image of an *in vivo* thyroid with a nodule. Flow in the carotid and echo noise in the trachea cause errors in motion tracking and strain estimation.

there are no echo signals from the trachea, displacement estimates in this region are at best misleading. The blood flow in the carotid is perpendicular to the image plane and introduces elevational motion that causes echo signal decorrelation and motion tracking errors. The observer must consider these factors for correct strain image interpretation in this case.

CONCLUSION

A computationally efficient displacement estimation algorithm has been developed for real-time, freehand ultrasonic strain imaging. The proposed method is based on a block-matching algorithm that is widely used for motion detection in digital image processing. Major modifications increase the computational efficiency and robustness of the typical block matching algorithm. The algorithm is implemented on the Siemens SONOLINE Elegra as an add-on software application.

With real-time feedback of strain images, sonographers can adjust their compression/ scanning technique to consistently form strain images. Strain images with acceptable quality are observed in both breast and thyroid scanning, which require different scanning tech-

niques and where the motion is much more complex than in phantoms. Since the algorithm is implemented on a commercially available clinical imaging system, data can be efficiently acquired from a large number of patients, enabling clinical evaluation of strain imaging in soft tissue diagnosis.

ACKNOWLEDGEMENTS

REFERENCES

1. Tristam, M., Barbosa, D.C., Cosgrove, D.O., Nassiri, D.K., Bamber, J.C. and Hill, C.R., Ultrasonic study of in vivo kinetic characteristics of human tissues, *Ultrasound Med. Biol. 12*, 927-937 (1986).

2. Krouskop, T.A., Dougherty, D.R. and Vinson, S.F., A pulsed Doppler ultrasonic system for making non-invasive measurements of the mechanical properties of soft tissues, *J. Rehab. Res. Dev. 24*, 1-8 (1987).

3. Ophir, J., Céspedes, I., Ponnekanti, H., Vazdi, Y., and Li, X., Elastography: a quantitative method for imaging the elasticity of biological tissues, *Ultrasonic Imaging 13*, 111-134 (1991).

4. O'Donnell, M., Skovoroda, A.R., Shapo, B., and Emelianov, S. , Internal displacement and strain iamging using ultrasonic speckle tracking, *IEEE Trans. Ultrason. Ferroelec. Freq. Contr. 41*, 314-325 (1994).

5. Chaturvedi, P., Insana, M.F. and Hall, T.J. , 2-d companding for noise reduction in strain imaging, *IEEE Trans. Ultrason. Ferroelec. Freq. Contr. 45*, 179-191 (1998).

6. Doyley, M.M., Bamber, J.C., Fuechsel, F. and Bush, N.L., A freehand elastographic imaging approach for clinical breast imaging: system development and performance evaluation, *Ultrasound Med. Biol. 27*, 1347-1357 (2001).

7. Hiltawsky, K.., Kruger, M., Starke, C., Heuser, L., Ermert, H., and Jensen, A., Freehand ultrasound elastography of breast lesions: clinical results, *Ultrasound Med. Biol. 27*, 1461-1469 (2001).

8. Garra, B.S., Céspedes, I., Ophir, J., Spratt, S.R., Zuurbier, R.A., Magnant, C.M. and Pennanen, M.F., Elastography of breast lesions: initial clinical results, *Radiology 202*, 79-86 (1997).

9. Lorenz, A., Sommerfeld, H.J., Garcia-Schurmann, M., Philippou, S., Senge, T. and Ermert, H. , A new system for the acquistioin of ultrasonic multicompression strain images of the human prostate in vivo, *IEEE Trans. Ultrason. Ferroelec. Freq. Contr. 46*, 1147-1154 (1999).

10. Chaturvedi, P., Insana, M.F., and Hall, T.J., Testing the limitations of 2-D local companding in strain imaging using phantoms, *IEEE Trans. Ultrason. Ferroelec. Freq. Contr. 45, 1022-1031 (1998)*.

11. Trahey, GE., Allison, J. W. and von Ramm, O.T., Angle independent ultrasonic detection of blood flow, *IEEE Trans. Biomed. Eng. 34*, 965-967 (1987).

12. Varghese, T. and Ophir, J., Characterization of elastographic noise using the envelope of echo signals, *Ultrasound Med. Biol. 24*, 543-555 (1998).

13. Alam, S.K. and Ophir, J., The effects of nonlinear signal transforamtions on bias errors in elastography, *IEEE Trans. Ultrason. Ferroelec. Freq. Contr. 47*, 297-303 (2000).

14. Kallel, F. and Ophir, J., A least-squares strain estimator for elastography, *Ultrasonic Imaging 10*, 195-208 (1997).

15. Urkowitz, H., *Signal Theory and Random Processes* (Artech House, Inc., Norwood, MA, 1983).

16. Konofagou, E., Dutta, P., Ophir, J. and Céspedes, I., Reduction of stress nonuniformities by apodization of compressor displacement in elastography, *Ultrasound Med. Biol. 22*, 1229-1236 (1996).

17. Krouskop, T.A., Wheeler, T.M., Kallel, F., Garra, B.S. and Hall, T.J., Elastic moduli of breast and prostate tissues under compression, *Ultrasonic Imaging 20*, 260-274 (1998).

18. Hall, T.J., Bilgen, M., Insana, M.F., and Krouskop, T.A., Phantom materials for elastography, *IEEE Trans Ultrason, Ferroelec. Freq Contr. 44*, 1355-1365 (1997).

A Finite-Element Approach for Young's Modulus Reconstruction

Yanning Zhu*, Timothy J. Hall, and Jingfeng Jiang

Abstract—Modulus imaging has great potential in soft-tissue characterization since it reveals intrinsic mechanical properties. A novel Young's modulus reconstruction algorithm that is based on finite-element analysis is reported here. This new method overcomes some limitations in other Young's modulus reconstruction methods. Specifically, it relaxes the force boundary condition requirements so that only the force distribution at the compression surface is necessary, thus making the new method more practical. The validity of the new method is demonstrated and the performance of the algorithm with noise in the input data is tested using numerical simulations. Details of how to apply this method under clinical conditions is also discussed.

Index Terms—Tissue characterization, tissue elasticity.

I. INTRODUCTION

THE ELASTIC properties of biological tissues are usually modified by disease. Surgeons often describe the "feel" of excised abnormal tissues. As a result, a quantitative measure of the elastic properties of tissue should be useful in diagnosing abnormalities. The physical quantities that describe tissue elastic properties are stress, strain, and elastic moduli, and methods have been developed to estimate each of these. Palpation, which has been used for more than 4000 years, utilizes tissue surface stress information to detect tissue abnormalities. Palpation remains an effective diagnostic tool. In fact, the majority of breast tumors are discovered with palpation [1]. However, palpation is qualitative and lacks sensitivity to small deep abnormalities. Quantitative methods similar to palpation have been developed to visualize surface pressure [2], [3]. Other recent developments in bioelasticity imaging techniques involve accurately and noninvasively measuring the tissue strain distribution during external compression. Studies have shown that these techniques show promise in diagnosing and monitoring diseases of the breast [4]–[7], kidney [8]–[11], and blood vessels [12], [13].

Mapping stress or strain distributions provides only relative information about tissue elasticity. Using either stress or strain information alone, one can only identify a region of tissue that is stiff (or soft) relative to its surroundings. Elastic moduli provide

an absolute measure of tissue elasticity that is intrinsic to the material. The stress or strain distributions alone lacks a one-to-one relationship with the elastic moduli distribution. Images of the stress or strain distribution may also include misleading artifacts that could lead to uncertainties in diagnosing tissue abnormalities. Therefore, it is desirable to measure elastic moduli in bioelasticity imaging techniques. However, measuring the distribution of elastic moduli is more difficult than either the stress or strain distribution.

The theory of mechanics shows that to describe the complete elastic properties of a material requires a tensor that has 81 components [14]. Clearly, it is impractical to measure all these components. Assumptions can be made to simplify the problem and reduce the number of unique tensor elements. If a material is assumed to be continuous, incompressible, and isotropic, then its elasticity can be completely described by one elastic modulus, either Young's modulus E or shear modulus μ. Strictly speaking, none of the above assumptions are valid for biological tissues, but most biological tissues closely approximate continuous and incompressible materials. Some tissues, such as muscle, are anisotropic in their structure, function, and mechanical properties. For this paper, however, we will assume tissue to be continuous, incompressible, and isotropic as a first approximation.

Currently, ultrasonic-based techniques for measuring the elastic modulus of tissue fall into two categories. First, dynamic compression techniques [15]–[18], such as sonoelasticity, use a vibrator to propagate low-frequency "pumping" waves into tissue. In the most promising of these approaches, shear wave velocity or wavelength are estimated, and from these the shear modulus can be estimated. However, problems associated with this technique are high image noise, low spatial resolution, and difficulty in propagating the shear wave energy across tissue boundaries.

The other category is referred to as (quasi)static compression techniques. In static compression techniques, the tissue Young's modulus distribution is estimated from the tissue deformation and boundary pressure measurements. The methods to estimate tissue deformation have been extensively discussed in ultrasound based elastography [19]–[28]. The tissue is deformed either by an external force or an internal force. The RF echo waveforms before and after an incremental deformation are recorded, and the tissue displacement distribution is estimated by comparing these RF waveforms. Tissue internal displacement can be also obtained using magnetic resonance imaging [29]–[31] and optical elastography [32] techniques. Young's modulus estimation can be performed utilizing the tissue deformation information obtained with the strain imaging

techniques. In addition to the displacement distribution, some Young's modulus estimation methods also require knowledge of the pressure or force boundary conditions.

There are four methods in the literature for reconstructing the Young's modulus distribution based on static compression techniques for displacement estimation. The first method estimates Young's modulus by numerically solving a second-order partial differential equation that describes a linear, isotropic, incompressible medium under static deformation [33]. That method requires significant spatial smoothing of the displacement estimates to obtain second-order partial differentials that are also smooth. Hence, with noisy displacement estimates, that method inherently has low spatial resolution. Another problem associated with that method is that for a two-dimensional (2-D) analysis, the force boundary condition of the medium must be known on all sides. However, in practice, the force distribution can only be (easily) measured on one side (the compression surface) of the medium.

The second method uses an iterative technique to reconstruct the modulus distribution [34], [35]. That method uses finite-element analysis (FEA) to solve the forward elasticity problem. The input to the FEA algorithm is the measured displacement field, the assumed boundary conditions, and an initial guess of the modulus distribution. The output of the FEA algorithm is an estimate of the displacement distribution. The difference between the measured displacement distribution and the FEA prediction is used to adjust the modulus distribution from its initial guess. By repeating the process multiple times, one can obtain a modulus distribution that minimizes the displacement distribution difference in a least squares sense. The advantage of that approach is that it does not require knowledge of the pressure boundary conditions. However, without knowing the boundary pressure, only relative modulus estimates can be obtained. In other words, the ratio of the modulus between different locations can be determined. Although that method can reduce the artifacts in strain images, it does not provide absolute measurement of the tissue modulus distribution which can be useful in tumor discrimination as suggested in [36], and an incorrect initial modulus guess may result in convergence to an incorrect modulus distribution. For media, such as tissue, that have a complicated modulus distribution, a good initial guess for the modulus distribution is difficult to obtain.

In the third modulus reconstruction method, a finite-difference approach is used to describe the elasticity problem in a medium [37]. That approach rearranges linear equations that describe the forward problem so that the modulus distribution becomes unknown variables in these equations. The modulus distribution can then be solved. However, that method also requires knowledge of the boundary conditions on all sides of the object.

The fourth approach uses a variational method to formulate the forward solution [38]. Then the terms with unknowns are rearranged to derive a matrix equation similar to ours. However, the boundary force condition was not utilized in their treatment. Hence, this method can only reconstruct the ratio between the Lame constants and tissue mass density.

In our approach, FEA is used to construct a set of linear equations that describes the elastic behavior of a 2-D object. Similar

to the third method mentioned above, we rewrite the linear equation set so that the Young's modulus distribution are explicit variables which can be solved. The solution does not require an initial guess or iteration of the modulus distribution solution, and it provides absolute, not relative, modulus estimates. Unlike the equation set for solving forward elasticity problems, where the number of equations equals the number of unknown variables, the equation set for our inverse solution usually involves more equations than unknowns. This allows us to simplify the force boundary conditions so that only one (surface) force distribution is necessary to solve for the modulus distribution.

The details of our modulus estimation method are described in Section II. The validity of this method is tested with simulations and results are shown in Section III. The discussion of how this technique can be implemented for ultrasonic imaging systems is provided in Section IV.

II. METHOD

Three integral parts of the proposed modulus estimation method are described in this section, one subsection each. Section II-A provides the information necessary for solving a forward elasticity problem of 2-D continua using FEA. Although the content of this subsection is well known in the literature, it is briefly reviewed here to provide sufficient background, terminology, and notation for the development of Section II-B. In Section II-B, the FEA-based modulus estimation technique (inverse problem) is described in detail. Section II-C addresses issues of how to apply the proposed method under practical constraints.

A. The FEA Method for Solving a Forward Problem of 2-D Continua

The FEA procedure for solving a forward elasticity problem of 2-D continua can be summarized as follows [39]–[41].

1) Select an element type and derive the element stiffness matrix.
2) Form a mesh using the selected element to cover the region of interest (ROI) for which the elasticity problem is solved.
3) Generate the global stiffness matrix by assembling element stiffness matrices.
4) Apply the boundary conditions to solve the global matrix equations for the solution.

The details of these steps are provided below.

Step 1: For 2-D problems, the common choices for element type are triangles or quadrilaterals. In other words, each element has either three or four nodes. The element matrix equations for elasticity problems have the form

$$K^{(e)}\delta^{(e)} = f^{(e)} \tag{1}$$

where $K^{(e)}$, $\delta^{(e)}$, and $f^{(e)}$ are, respectively, the element stiffness matrix, the element nodal displacement vector, and the element nodal force vector for element e. In this paper, rectangular elements, as shown in Fig. 1, are used. Details of how to compute the element stiffness matrix is provided in Appendix I.

Step 2: For problems that can be described by partial differential equations but do not have closed form solutions, FEA has
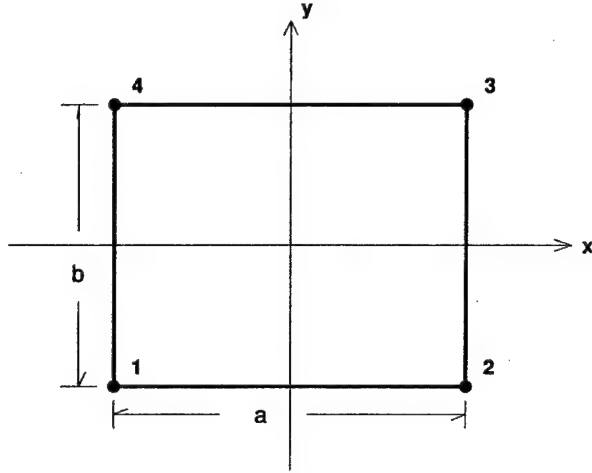
Fig. 1. The rectangular mesh element. Nodal numbers start from the bottom left corner and increase on the clockwise direction.
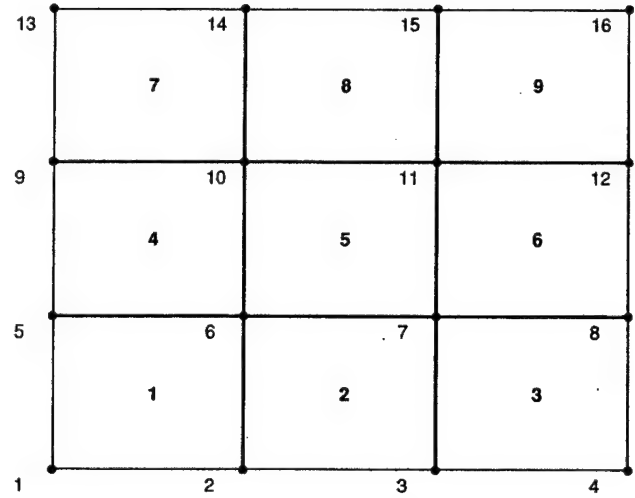

Fig. 2. A nine-element mesh composed of rectangular elements with uniform size. Numbers in the center of the rectangular elements are the element numbers and numbers close to nodes (intersection points) are the global nodal numbers.

been developed to find approximate numerical solutions on discretized problem domains. These solutions can then be interpolated to form continuous solution spaces using shape functions. The discretization process is performed by creating a mesh that covers the ROI in the object.

A mesh is composed of elements that cover a contiguous area in the problem domain. In this paper, all elements in the ROI are rectangles of the same size. A nine-element mesh is illustrated in Fig. 2. The numbers in the center of the rectangular elements are element numbers and numbers close to nodes (intersection points) are nodal numbers.

The mesh configuration can be represented by a connectivity matrix, C. The number of rows of C equals the number of elements, N_e. For four-node elements (rectangles), C has four columns. The ith row of C records nodes associated with the ith element. For the mesh shown in Fig. 2, the first two rows of C are

$$\begin{pmatrix} 1 & 2 & 6 & 5 \\ 2 & 3 & 7 & 6 \end{pmatrix}. \tag{2}$$

Step 3: The matrix equation for a meshed system (for example, the system described in Fig. 2) has the form

$$K\delta = f, \tag{3}$$

where K is the global stiffness matrix; δ is the global nodal displacement vector; and f is the global nodal force vector. The global displacement vector has the form

$$\delta = \begin{pmatrix} \delta_{1x} & \delta_{1y} & \delta_{2x} & \delta_{2y} & \dots \end{pmatrix}^T \tag{4}$$

where δ_{1x} and δ_{1y} are the displacements in the x and y directions for node 1, and so on. The global nodal force vector has the form

$$f = \begin{pmatrix} f_{1x} & f_{1y} & f_{2x} & f_{2y} & \cdots \end{pmatrix}^T \tag{5}$$

where f_{1x} and f_{1y} are the net force exerted on node 1 in x and y directions, and so on. The global stiffness matrix K is assembled from element stiffness matrices. The assembly process can be found in Appendix II.

Step 4: Displacement boundary conditions are usually specified for the elasticity problems in our applications, and a penalty

approach [41] can be used to solve (3). The details of the penalty approach is provided in Appendix III.

B. The FEA Approach for Solving an Inverse Problem of 2-D Continua

Soft tissues can generally be considered as incompressible media [33]. Hence, the Possion's ratio can be assumed to be a constant that is close to 0.5 (0.49, for instance) throughout the ROI. With this assumption, matrix $\tilde{K}$ in (24) is same for every element if all elements have the same aspect ratio (which is true in this paper since the mesh is composed of the elements with same size).

In the element-to-global stiffness matrix assembly procedure described in Section II-A, each component of $K^{(e)}$ (i.e., the product of the element Young's modulus and a constant) is accumulated onto the global stiffness matrix. Hence, each component of the global stiffness matrix is a linear combination of the Young's modulus of each element. In other words, the global stiffness matrix can be written as

$$K = [K_{ij}] \quad i = 1, \dots, N, j = 1, \dots, N, \tag{6}$$

$$K_{ij} = \sum_{e=1}^{N_e} c_e^{ij} E^{(e)} \tag{7}$$

where c_e^{ij} are constants.

From (3), the left-hand side of the system matrix equation is $K\delta$. In Young's modulus reconstruction, the displacement distribution is estimated with tissue motion tracking techniques. In other words, δ is a "known" vector. Performing the matrix-vector multiplication

$$K\delta = \begin{bmatrix} \sum_{j=1}^{N} \delta_j K_{1j} \\ \vdots \\ \sum_{j=1}^{N} \delta_j K_{ij} \\ \vdots \\ \sum_{j=1}^{N} \delta_j K_{Nj} \end{bmatrix}. \tag{8}$$

Since K_{ij} is a linear combination of $E^{(e)}$ [see (7)], each component of the resulting vector on the right-hand side of (8) is also a linear combination of $E^{(e)}$. Or

$$K\delta = \begin{bmatrix} \sum_{j=1}^{N_e} D_{1j} E^{(j)} \\ \vdots \\ \sum_{j=1}^{N_e} D_{ij} E^{(j)} \\ \vdots \\ \sum_{j=1}^{N_e} D_{Nj} E^{(j)} \end{bmatrix}. \tag{9}$$

The right-hand side of (9) can be written as a product of a matrix and a vector. Or

$$K\delta = DE \tag{10}$$

where D is a N-by-N_e matrix; $E = (E^{(1)} \cdots E^{(j)} \cdots E^{(N_e)})^T$ is the Young's modulus vector. Now, (3) can be rewritten as

$$DE = f. \tag{11}$$

Recall from the global stiffness matrix assembly procedure, provided in Section II-B, that the component $K_{ij}^{(e)} = E^{(e)} \widetilde{K}_{ij}$ of the local stiffness matrix of element e is accumulated to the $C_i^{(e)}$th row and $C_j^{(e)}$th column of the global stiffness matrix, or $K_{C_i^{(e)} C_j^{(e)}}$. When performing the multiplication of $K\delta$ [see (8)], $E^{(e)} \widetilde{K}_{ij}$ is multiplied with $\delta_{C_j^{(e)}}$. The product is then accumulated to the $C_i^{(e)}$th component of the resulting vector. Hence, $\widetilde{K}_{ij} \delta_{C_j^{(e)}}$ is a summand of the $C_i^{(e)}$th row and eth column component of the matrix D. Based on this observation, the matrix D can be assembled from the element stiffness matrix using the following procedure.

1) Initialize a N-by-N_e null matrix.
2) For element e, generate a local variable number to global variable number conversion index vector $I^{(e)}$ defined in (26).
3) Accumulate $\widetilde{K}_{ij} \delta_{I_j^{(e)}}$ to $D_{I_i^{(e)} e}$ for $i = 1, \ldots, 8$ and $j = 1, \ldots, 8$.
4) Iterate 2 and 3 for all elements.

Similar to solving forward elasticity problems with (3), the Young's modulus reconstruction problem can be solved from (11) were D is an N-by-N_e matrix. Usually, $N > N_e$ and (11) defines an overdetermined set of equations. The common technique for solving an overdetermined linear equation set is to convert it to a least-square problem [42]. The conversion can be done by multiplying both sides of (11) by D^T

$$(D^T D)E = D^T f. \tag{12}$$

Since $(D^T D)$ is an N_e-by-N_e matrix, E can be solved by the following equation

$$E = (D^T D)^{-1} D^T f. \tag{13}$$

The application of this method under practical constraints is provided in the next subsection.

C. Practical Concerns

1) Necessary Measurements: Equation (3) implies that there is an unstressed state to which the object returns when all external forces are removed from the object. Then, the external forces (e.g., gravitational force, atmospherical pressure, and compressional force) are exerted on the object. The displacement is measured between the unstressed state and the state with external load. In reality, however, the geometrical distribution of the object in the unstressed state is unknown. Hence, (11) [which is derived from (3)] cannot be used directly to solve the inverse problem. Fortunately, if the object is assumed to be a linear elastic body for small incremental deformations, then this problem can be solved.

Assume there are two loading states of the object S_1 and S_2. In S_1, the object can be described by

$$K\delta^{(S_1)} = f^{(S_1)} \tag{14}$$

where $\delta^{(S_1)}$ is the object displacement between the natural state and S_1; $f^{(S_1)}$ is the compressional load measured in S_1. In S_2, the object can be described by

$$K\delta^{(S_2)} = f^{(S_2)}. \tag{15}$$

Note that K is state independent given the linear elastic body assumption.

Subtracting (15) from (14), we find

$$K\Delta\delta = \Delta f \tag{16}$$

where $\Delta\delta = \delta^{(S_1)} - \delta^{(S_2)}$ and $\Delta f = f^{(S_1)} - f^{(S_2)}$. Replacing (3) with (16), the derivation introduced in Section II-B still holds. (16) states that three measurements, namely, $\Delta\delta$, $f^{(S_1)}$, and $f^{(S_2)}$, are necessary for Young's modulus reconstruction.

2) Young's Modulus Reconstruction With Partial Boundary Conditions: Recall that (11) defines an over-determined set of linear equations. This means that only a subset of (11) are needed for inverse solution. Let D_s be a matrix that is formed from a subset of rows from D, and f_s be the force vector formed from the corresponding subset of f. As long as $(D_s^T D_s)$ is invertible, a unique inverse solution can be obtained from

$$E = (D_s^T D_s)^{-1} D_s^T f_s. \tag{17}$$

This property can be used to relax the force boundary conditions for the inverse problem.

Under typical conditions a subregion of the tissue under study is observed. A mesh can be created to cover an ROI which is a subset of the field of view. Only one side (the surface of the tissue) of the boundary force distribution can be measured with ease with a force sensor array. With the example shown in Fig. 2, let us assume that the compressional force can be measured along the top side (nodes {13, 14, 15, 16}). D_s and f_s are determined by the following rule: *select all equations from (11) involving all interior nodes of the mesh and all nodes except the outer most two for which the force measurements are made.* With the example shown in Fig. 2, the selected nodes are {6, 7, 10, 11, 14, 15}. The related subset of the matrix equations include rows {11, 12, 13, 14, 19, 20, 21, 22, 27, 28, 29, 30} of (11).

It is difficult to mathematically prove that the equation selection rule described above always provides invertible $D_s^T D_s$, however, it is easy to test whether $D_s^T D_s$ is invertible given a mesh configuration. From the variety of mesh configurations that have been tested, the equation selection rule described above always provides invertible $D_s^T D_s$.

3) The Size of D Matrix: The size of the matrix D can be a problem if it is assembled as a dense matrix. For example, if the mesh has 100×100 elements, then there are total of $101 \times 101 = 10\,201$ nodes. The size of D is 20 402-by-10 000, or 204 020 000 components. Representing each component as double precision floating point numbers and storing this dense matrix requires about 1.52 GB of computer memory. With current computer technology, storing such a large matrix may not be a problem. However, calculating $(D^T D)^{-1}$ is impractical.

Fortunately, D is a sparse matrix. Recall that each row of (3) describes the behavior of a node, and there are a maximum of four elements related to one node. Thus, the maximum nonzero components of a row in D is four.

The number of nonzero components of D for a 100-by-100 element mesh is in fact 80 000. Using the sparse matrix features provided by MATLAB, this can be stored with about 1MB of memory. Compared with dense matrix storage, this is a 1600:1 reduction in memory requirement. Using a 750-MHz Pentium III PC, $(D^T D)^{-1}$ can be computed in about 20 s. Note that although the discussion is based on D, same conclusion can be drawn for D_s.

III. RESULTS

A. Solving the Forward Problem With Ideal Input

First, we simulated an object for which the forward problem was solved. The dimension of the simulated object was $40 \times 40 \times 2$ (width $\times$ height $\times$ thickness in millimeters). Young's modulus distribution of the object is shown in Fig. 3. The Young's modulus of the background was 15 kPa which approximates the stiffness of normal glandular breast tissue [36]. There were two 10-mm-diameter targets in the object that simulate lesions. The upper target was three times stiffer (45 kPa) than the background and the lower target was three times less stiff (5 kPa) than the background.

A mesh was created for this object with 160 elements in both horizontal and vertical directions. The total number of elements was $160 \times 160 = 25\,600$. The size of each element was 0.25 mm $\times$ 0.25 mm. To produce a realistic estimate of boundary force values, we assumed plain stress conditions for the compression. The Possion's ratio ν of 0.49 was used (incompressible media). The displacement boundary conditions were assigned such that the displacement of bottom side of the object was zero and the top side of the the object was 0.8 mm simulating a 2% compression of the object.

Using the forward FEA method introduced in Section II-A, we calculated the displacement distribution and the force distribution along top and the bottom sides of the object. Using the displacement distribution, strain in both the horizontal direction (s_{xx}) and vertical direction (s_{yy}) were calculated and shown in Fig. 4(a) and (b), respectively. With the plain stress assumption, the following relationship holds $s_{xx}/s_{yy} = -\nu/2$. The force distribution on the top and bottom sides of the object are shown in Fig. 5(a) and (b), respectively. Note that the forces on the top side are all negative since the direction of the applied force is pointing vertically down. As shown in Fig. 5, the magnitude of force on the outer most nodes are half of the magnitude of the
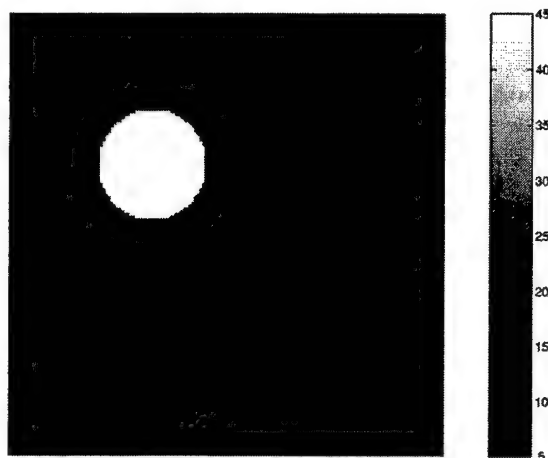

Fig. 3. The Young's modulus distribution for the simulated object. The units of the color bar are kPa.
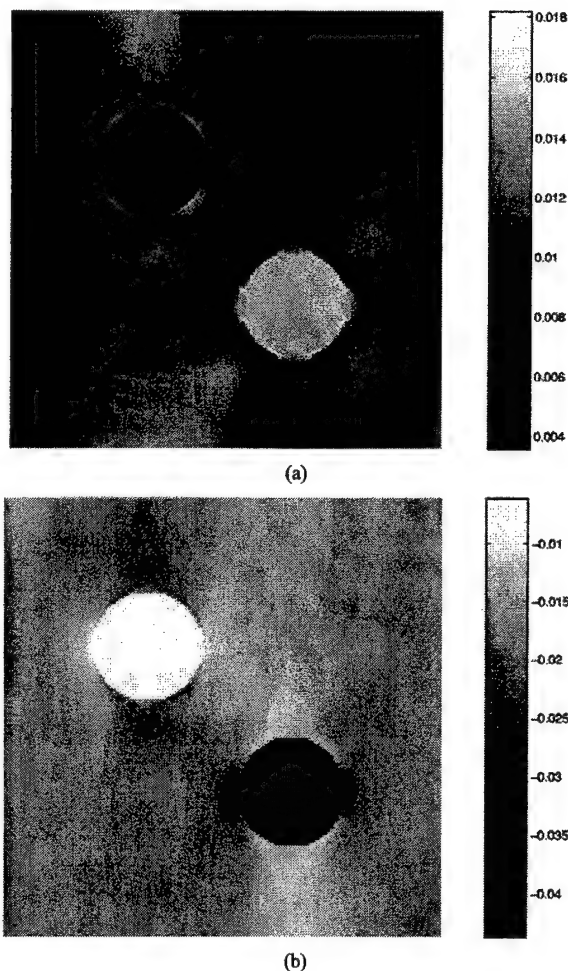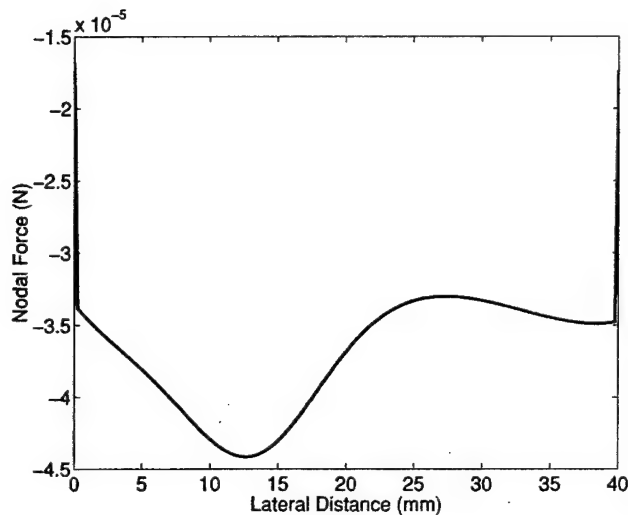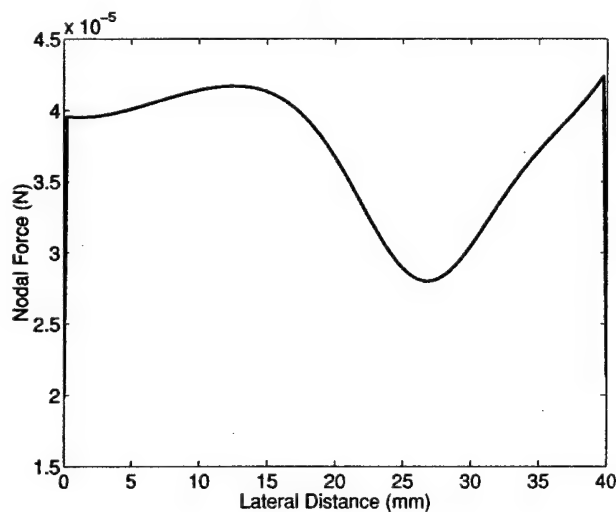

(a)

(b)

Fig. 4. Strain images obtained from the forward FEA calculation for the object illustrated in Fig. 3. (a) Horizontal strain s_{xx}. (b) Vertical strain s_{yy}.

force on their adjacent nodes since the area of support for the outer most nodes is half that of the inner nodes. With the same surface pressure, the exerted force is half the magnitude.

(a)

Meshed area for forward simulation

Fig. 6. An illustration of the meshed areas for the forward simulation and the Young's modulus reconstruction.

(b)

Fig. 5. The boundary force distribution obtained from the forward FEA calculation for the object illustrated in Fig. 3. (a) Force on the top side. (b) Force on the bottom side.

Fig. 7. The reconstructed Young's modulus image using the ideal (noise-free) displacement and force boundary conditions.

B. Solving the Inverse Problem With Ideal Input

To test the modulus reconstruction technique we used the results of the forward problem calculations, but, in effect, discarded nonessential information. The only input to the inverse (modulus distribution) computation were the ideal displacement distribution over a (sub-)ROI and the force distribution at the top (compression) surface generated by the forward solution. The sub-ROI was 30 mm × 30 mm and a new mesh was created to cover that area. An illustration of the meshed areas for the forward simulation and the inverse reconstruction is shown in Fig. 6.

Fig. 7 shows the result of the Young's modulus estimation. The standard deviation of the relative error in the reconstructed Young's modulus distribution is $2.0 \times 10^{-5}\%$—a nearly exact reconstruction is obtained. This result is encouraging since it shows that the Young's modulus estimation method introduced above is a valid approach and confirms that the "partial force"
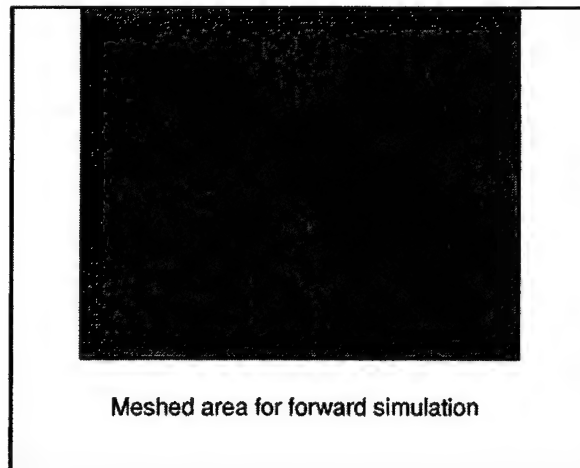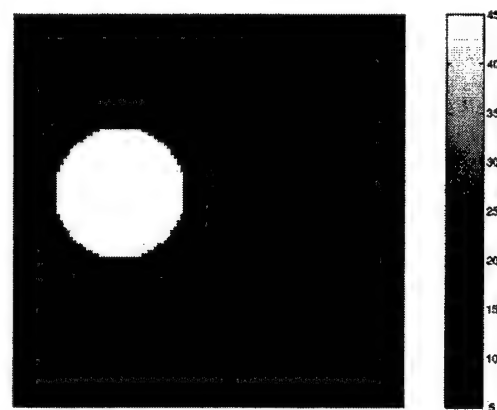
boundary condition is sufficient to estimate the modulus distribution.

In the above modulus estimation simulation, the size of the elements was the same as that used in the forward simulation. The small elements provide high spatial resolution. However, it is not likely that such high spatial resolution can be achieved under all practical conditions. In the next simulation, we increased the size of the elements to 1 mm × 1 mm. In other words, we blurred the spatial sampling by a factor of 4. Fig. 8(a) shows the "true" modulus image of the same object. The "true" modulus value of each element were calculated by averaging the 16 modulus values in the corresponding area of the finer meshed object. The inverse problem was solved using the exact displacement and force from the forward simulation results produced by the finer mesh. The result of the modulus estimation is shown in Fig. 8(b). The relative difference between Fig. 8(a) and (b) is shown in Fig. 8(c). The mean and standard deviation of the image shown in Fig. 8(c) are −1.25% and 17.8%, respectively. The small mean value suggests that the modulus estimates are unbiased. However, the standard deviation value shows that the reconstructed modulus image using larger element size can be noisy. Since the modulus estimates are unbiased, a simple spatial averaging can improve the visual effect of the reconstructed

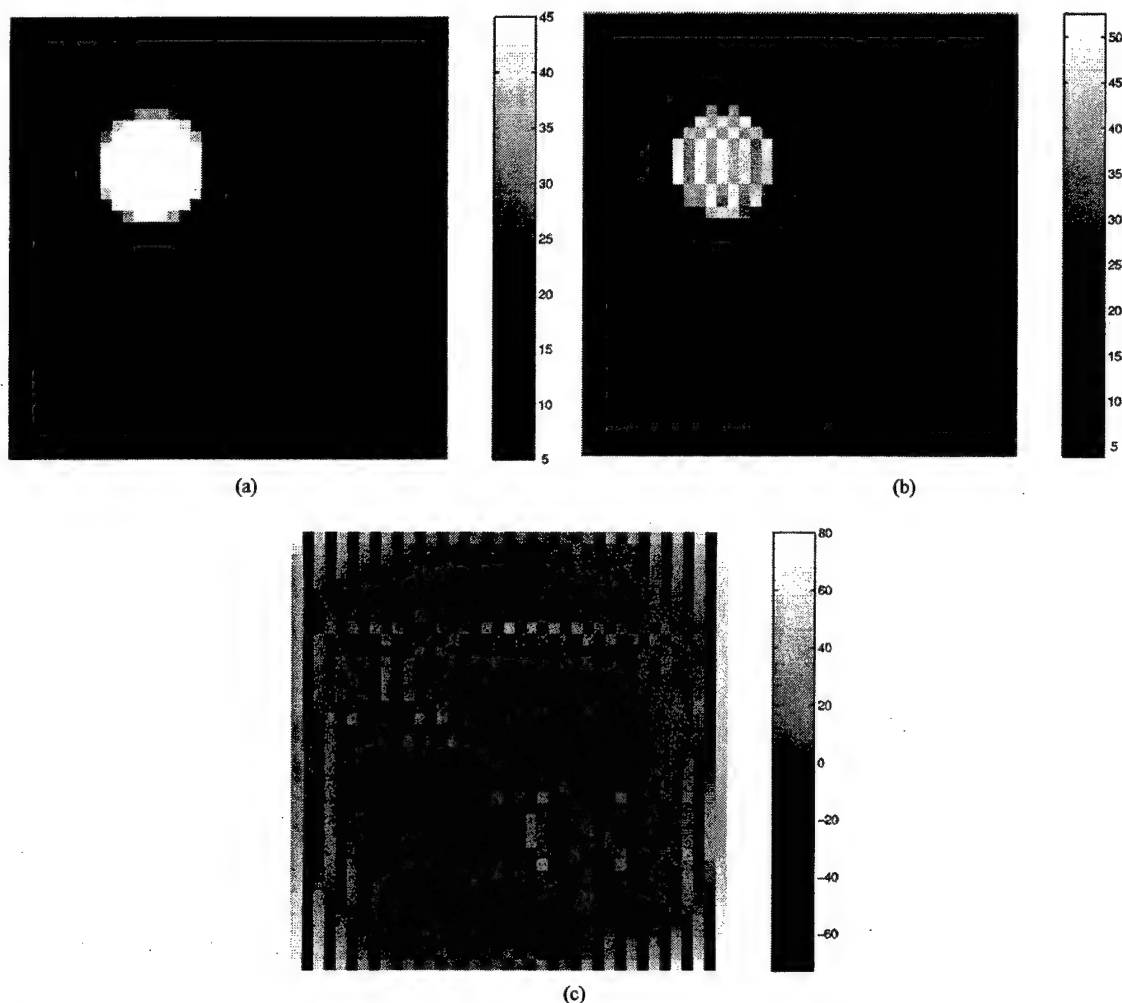(a)   (b)

(c)

Fig. 8.   Simulation results using the larger element size. (a) The ideal decimated modulus image. (b) The reconstructed modulus image using the larger element size. (c) The relative difference between (a) and (b) measured in percentage, mean $= -1.25\%$, std $= 17.8\%$.

modulus images at the expense of further reducing the spatial resolution.

C. Modulus Estimation With Noisy Displacement and Boundary Force Estimates

Inevitably, there is noise in the displacement and boundary force estimates that are used in modulus estimation. Hence, it is necessary to study the effect of noise in the input data on the resulting modulus estimates. To avoid the difficulty of analytically deriving the noise relationship between input data and final outcome, we rely on numerical simulation. The forward solution shown in Figs. 4 and 5 was used as the ideal displacement and boundary force distributions. The inverse simulation was based on the mesh configuration that produced the result shown in Fig. 8. Noise, modeled as zero mean white Gaussian random processes [43],[1] was added to

both the ideal displacement and boundary force distributions. A range of the standard deviations (noise) were used to study the relationship between noise power and the modulus estimation error. For each predetermined level of noise, 100 realizations of (noisy) displacement and force distributions were generated and the object modulus distributions were reconstructed.

The modulus estimation error is defined as the difference between the "true" modulus distribution [Fig. 8(a)] and the estimated modulus distribution with noise present in the input data (force boundary condition and displacement distribution). The relative mean and the relative standard deviation of the error were calculated from the outcome of all 100 realizations of noise fields. The simulation results are shown in Fig. 9. The standard deviation of the noise added to the boundary force distribution is 5% of the mean ideal force in Fig. 9(a) and (b) and 10% in Fig. 9(c) and (d). Fig. 9(a) and (c) shows the relationship between the standard deviation of the displacement error and the mean relative modulus estimation error. Fig. 9(b) and (d) shows the relationship between the standard deviation of the displacement error and the standard deviation of the relative modulus estimation error.

---

[1]Bilgen et al have shown through simulation that the noise in displacement estimates is Gaussian distributed. However, the spectrum of the noise is not shown in their work. The spectrum of noise is assumed to be white as an approximation.
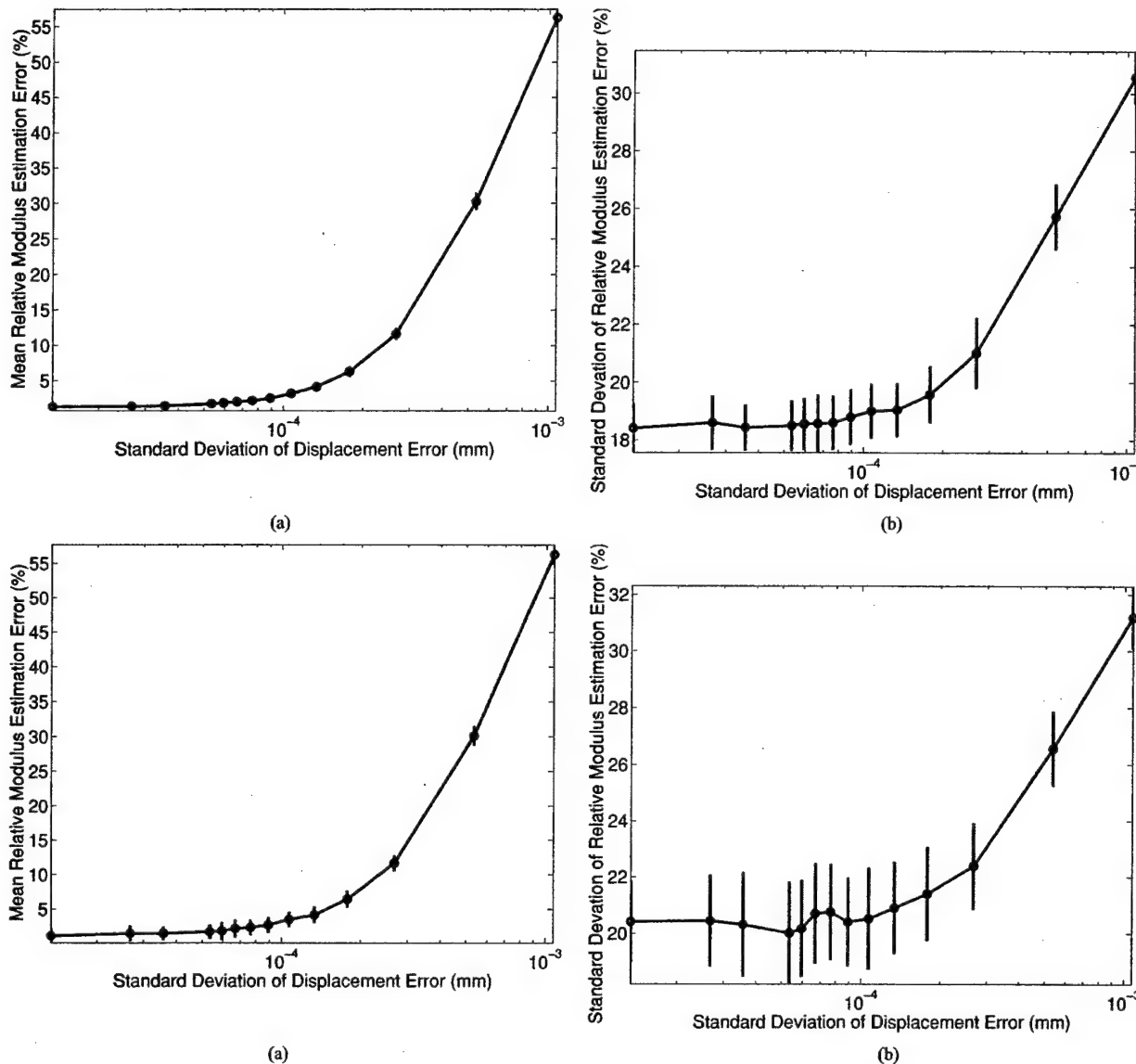
Fig. 9. Modulus estimation performance curves. (a) Standard deviation of the error in displacement versus the mean relative error in modulus estimates resulting from a 5% standard deviation in the "measured" force. (b) Standard deviation of the error in displacement versus standard deviation of the relative error in modulus estimates resulting from a 5% standard deviation in the "measured" force. (c) Standard deviation of the error in displacement versus the mean relative error in modulus estimates resulting from a 10% standard deviation in the "measured" force. (d) Standard deviation of the error in displacement versus standard deviation of the relative error in modulus estimates resulting from a 10% standard deviation in the "measured" force.

Comparing Fig. 9(a) with Fig. 9(c) and (d), we found that the modulus estimation error is not very sensitive to the errors in the boundary force measurements. However, it is very sensitive to errors in the displacement measurements. When the standard deviation of the displacement error exceeds 10^{-4} mm, the modulus estimation becomes biased, as shown in Fig. 9(a) and (b), and the noise in modulus estimation starts to increase rapidly. Note that the units in the horizontal axis of all plots in Fig. 9 are mm. To make the results independent of the actual object dimension, we re-plotted results in Fig. 10. In Fig. 10 the horizontal axis is changed to standard deviation of relative strain error. From the plots shown in Fig. 10, we can see that when the noise in the displacement estimates causes more than 1% strain error, the quality of modulus estimates starts to degrade rapidly.

IV. DISCUSSION

The derivation in Section II-C2, shows that the boundary conditions for the inverse problem with the proposed method are less restrictive than those of the forward problem. In the forward simulation, boundary conditions that describe all sides of the meshed object are required to solve (3) for the displacement distribution and the boundary force distribution. In modulus reconstruction, however, only the sub-ROI of the object needs to be meshed, and only partial boundary force conditions need to be specified. This makes our approach more practical and far easier to implement (experimentally) than other methods.

In our method, the medium is assumed to be elastic. Possible tissue viscous behavior is not accounted for in our model. With
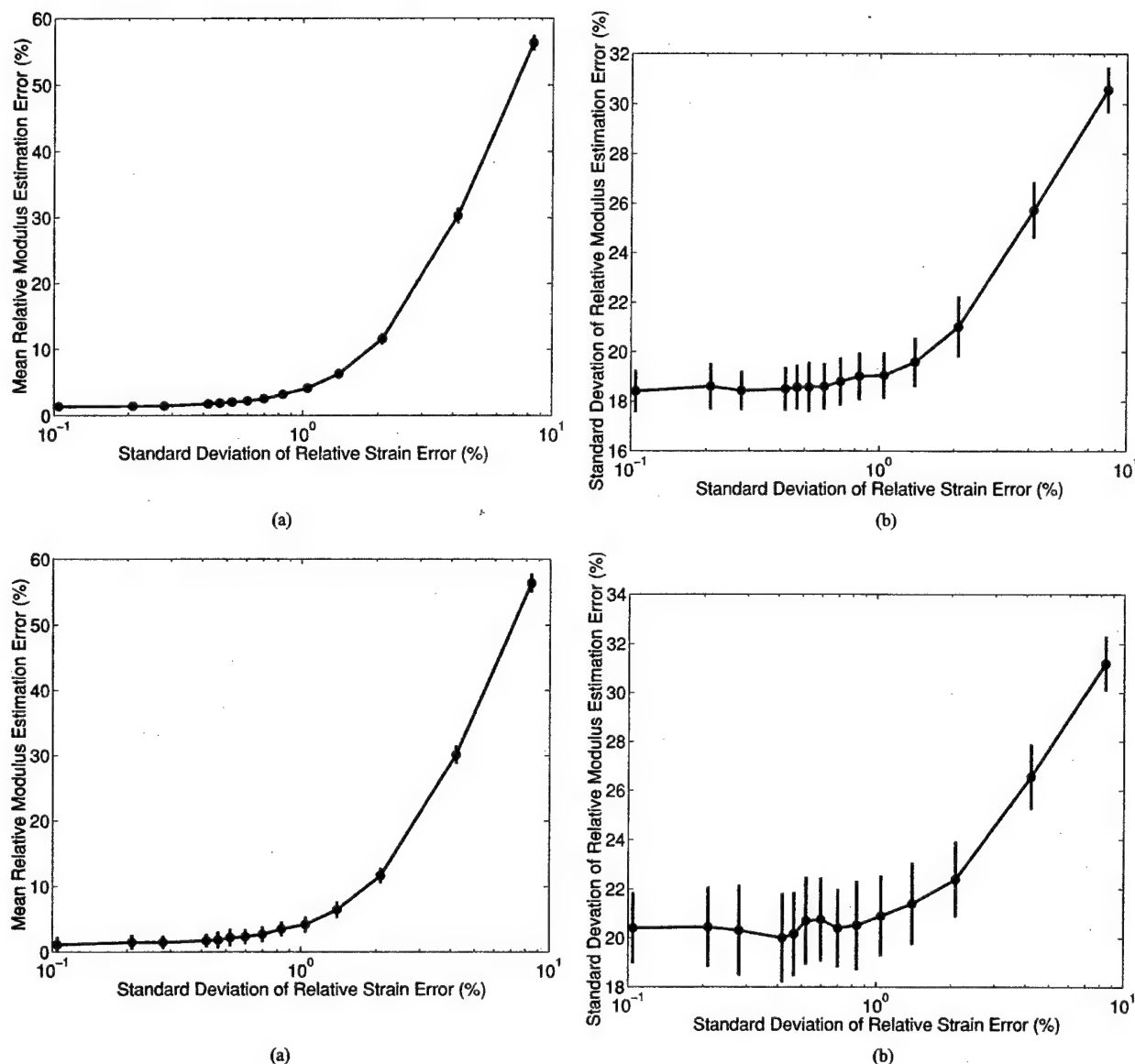
(a)

(b)

(a)

(b)

Fig. 10. Modulus estimation performance curves. (a) Standard deviation of the error in strain versus the mean relative error in modulus estimates resulting from a 5% standard deviation in the "measured" force. (b) Standard deviation of the error in strain versus standard deviation of the relative error in modulus estimates resulting from a 5% standard deviation in the "measured" force. (c) Standard deviation of the error in strain versus the mean relative error in modulus estimates resulting from a 10% standard deviation in the "measured" force. (d) Standard deviation of the error in strain versus standard deviation of the relative error in modulus estimates resulting from a 10% standard deviation in the "measured" force.

carefully designed methods for data acquisition, the viscous response to the external compression can be negligible [36].

In Section II-C1 we also assume the elastic behavior of the medium to be linear. This assumption only needs to be true between two states, S_1 and S_2. Most human tissues have a nonlinear stress-strain relationship. Although the tissue can have significant nonlinear behavior, we can restrict our analysis to incremental deformations and forces as described in (16). Since the incremental deformation between S_1 and S_2 is usually small (less than 2%), the assumption of linear elasticity is reasonable.

For high accuracy FEA solutions to the forward elasticity problem, the object is usually meshed with nonuniform size and shape elements. The mesh has higher element density near curved interfaces where the modulus changes value, but

this requires knowledge of the object geometry. In modulus reconstruction, the internal geometry is unknown, so rectangular elements are used. One may argue that it is possible to first obtain a rough modulus reconstruction using uniform elements, then re-mesh the object with nonuniform elements and reconstruct modulus again for higher accuracy. To do so requires higher accuracy displacement estimates in the regions with higher element density. Since the displacement field is usually estimated with uniform accuracy, this approach is likely to fail.

To understand the effect of the noise in the measured displacement and force distribution, we conducted a number of numerical simulations. The results of these simulations, shown in Figs. 9 and 10, provide an estimate of the required accuracy in

input displacement and force data. We found that the method is less sensitive to noise in the force measurements than to noise in the displacement estimates. The size of mesh elements can be adjusted to change the sensitivity to displacement estimation errors. For a given displacement error, larger mesh elements result in smaller the strain error.

From Figs. 10(b) and (d), we observed that the modulus estimates obtained from noisy displacement and force estimates are also noisy (22% relative errors). However, since the modulus contrast between normal and cancerous tissues is usually large (greater than 100%) [36], the modulus image contrast-to-noise ratio for cancerous lesions will still be high.

We cannot prove that the inverse problem has a unique solution from physical principles. However, our method provides a unique solution algebraically. For the simulations that we have conducted, when there is no noise in the input data, the solution that we obtained is the same (within the numerical processing errors) as the Young's modulus distribution that we specified for the object (see Fig. 7 and Section III-B). With the added noise (to both surface force and the displacement distribution), our method generates solutions that are close to the true Young's modulus distribution(see Fig. 9 and Section III-C). This suggests that our method is stable and robust. Since we lack the necessary equipment to simultaneously measure surface force and the displacement distribution and, therefore, cannot test our method experimentally. This will be the subject of future effort.

FEA treats 2-D elasticity problems as special cases of a general three-dimensional (3-D) problem. The choice of these special cases are either plain strain (elevational strain is zero) or plain stress (elevational stress is zero). With the plain strain assumption, the external force is assumed to be exerted on a one–dimensional boundary, and it is difficult to relate such a load condition to reality. With the plain stress assumption, the object has finite thickness, and the calculated boundary force can be more easily related to actual measurements obtained on a 2-D surface.

Tissue deformation is 3-D in nature. However, we have found that *in vivo* breast, for example, can be deformed such that the motion perpendicular to the image plane is small. Thus, a 2-D description of motion provides a reasonable approximation to the plane strain condition. However, force measurements are more easily related to the plane stress condition, and with this assumption the resulting modulus estimates will have limited accuracy. To overcome this limitation, we need to extend our approach to 3-D. Extending 2-D modeling to 3-D is relatively straightforward with FEA methods.

The examples and discussion of displacement estimation techniques relate to our work in using ultrasound to track tissue motion. There is also a growing body of work where magnetic resonance techniques are used for estimating tissue elasticity [44], [45]. The modulus reconstruction technique should be applicable in that work as well.

V. Conclusion

A new approach for estimating the modulus distribution from noninvasively determined force and displacement estimates is

reported. Simulations demonstrate that the modulus distribution for an ROI can be determined from force measurements on a single surface and displacement estimates within that ROI. The accuracy in force and displacement estimates required with this approach are also estimated with simulations. These results suggest that moduli of *in vivo* tissues can be estimated with reasonable accuracy with minor modification to current clinical imaging systems.

Appendix I

In Fig. 1, nodes are locally numbered.[2] The element nodal displacement vector for the rectangular element has eight components and can be written as

$$\delta^{(e)} = \begin{pmatrix} \delta_{1x}^{(e)} & \delta_{1y}^{(e)} & \delta_{2x}^{(e)} & \delta_{2y}^{(e)} & \delta_{3x}^{(e)} & \delta_{3y}^{(e)} & \delta_{4x}^{(e)} & \delta_{4y}^{(e)} \end{pmatrix}^T \tag{18}$$

where $\delta_{1x}^{(e)}$ and $\delta_{1y}^{(e)}$ are the displacement components in the x and y directions of the first node, and so on for the rest of the components; T is the matrix or vector transpose operator. The element nodal force vector also has eight components and can be written as

$$f^{(e)} = \begin{pmatrix} f_{1x}^{(e)} & f_{1y}^{(e)} & f_{2x}^{(e)} & f_{2y}^{(e)} & f_{3x}^{(e)} & f_{3y}^{(e)} & f_{4x}^{(e)} & f_{4y}^{(e)} \end{pmatrix}^T. \tag{19}$$

The element stiffness matrix can be computed as [40]

$$K^{(e)} = \int_{-b/2}^{b/2} \int_{-a/2}^{a/2} t B^{(e)T} M^{(e)} B^{(e)} dx dy \tag{20}$$

where t is the element thickness, M is the material property matrix, and B is the displacement to strain mapping matrix. For example, with linear elasticity problems and assuming plain stress

$$M^{(e)} = E^{(e)} \frac{\left(1 - \nu^{(e)}\right)}{\left(1 + \nu^{(e)}\right)\left(1 - 2\nu^{(e)}\right)}$$

$$\cdot \begin{bmatrix} 1 & \frac{\nu^{(e)}}{1-\nu^{(e)}} & 0 \\ \frac{\nu^{(e)}}{1-\nu^{(e)}} & 1 & 0 \\ 0 & 0 & \frac{1-2\nu^{(e)}}{2(1-\nu^{(e)})} \end{bmatrix} \tag{21}$$

where $E^{(e)}$ and $\nu^{(e)}$ are the Young's modulus and Possion's ratio of element e, and a and b are the element width and height. For rectangular elements, the displacement to strain mapping matrix is

$$B^{(e)} = \begin{bmatrix} \frac{\partial H_1}{\partial x} & 0 & \frac{\partial H_2}{\partial x} & 0 & \frac{\partial H_3}{\partial x} & 0 & \frac{\partial H_4}{\partial x} & 0 \\ 0 & \frac{\partial H_1}{\partial y} & 0 & \frac{\partial H_2}{\partial y} & 0 & \frac{\partial H_3}{\partial y} & 0 & \frac{\partial H_4}{\partial y} \\ \frac{\partial H_1}{\partial y} & \frac{\partial H_1}{\partial x} & \frac{\partial H_2}{\partial y} & \frac{\partial H_2}{\partial x} & \frac{\partial H_3}{\partial y} & \frac{\partial H_3}{\partial x} & \frac{\partial H_4}{\partial y} & \frac{\partial H_4}{\partial x} \end{bmatrix} \tag{22}$$

---

[2]The number starts from the lower left corner of the element and increases in the clockwise direction. Note that other numbering methods can also be selected as long as the connectivity matrix (introduced in Step 2) is created with the same numbering scheme for all elements.

where $H_i, i = 1, \ldots, 4$ are shape functions. The shape functions are usually selected to perform bilinear interpolations that have the form

$$H_1 = \frac{1}{ab}\left(\frac{a}{2} - x\right)\left(\frac{b}{2} - y\right)$$

$$H_2 = \frac{1}{ab}\left(\frac{a}{2} + x\right)\left(\frac{b}{2} - y\right)$$

$$H_3 = \frac{1}{ab}\left(\frac{a}{2} + x\right)\left(\frac{b}{2} + y\right)$$

$$H_4 = \frac{1}{ab}\left(\frac{a}{2} - x\right)\left(\frac{b}{2} + y\right). \tag{23}$$

The representation of the element stiffness matrix (24) can be obtained by substituting (21)–(23) into (20) and performing the double definite integration. For convenience in deriving the inverse (modulus estimation) problem, the element stiffness matrix can be written as

$$K^{(e)} = E^{(e)}\widetilde{K} \tag{24}$$

where $\widetilde{K}$ is an 8-by-8 matrix in which each component is a function of the aspect ratio (a/b) and Possion's ratio of the rectangular element.

APPENDIX II

Following is a description of the global stiffness matrix assembling process.

1) Initialize a N-by-N null matrix (all zero entries), where N equals the total degrees of freedom of the system or

N = number of nodes $\times$ degrees of freedom per node. (25)

For the mesh shown in Fig. 2, $N = 16 \times 2 = 32$.

2) For element e, generate a local (element) variable number to global (system) variable number conversion index vector

$$I^{(e)} = \Big(c_{e1}*2 - 1, c_{e1}*2, c_{e2}*2 - 1, c_{e2}*2, c_{e3}*2 - 1,$$

$$c_{e3}*2, c_{e4}*2 - 1, c_{e4}*2 \Big) \tag{26}$$

where c_{e1} is the eth row and first column entry of the connectivity matrix C, and so on. For the system shown in Fig. 2, the index vector for the first element is

$$I^{(1)} = (1 \quad 2 \quad 3 \quad 4 \quad 11 \quad 12 \quad 9 \quad 10). \tag{27}$$

3) Accumulate $K_{ij}^{(e)}$ to $K_{I_i^{(e)} I_j^{(e)}}$ for $i = 1, \ldots, 8$ and $j = 1, \ldots, 8$ ($K_{ij}^{(e)}$ is the ith row jth column component of matrix $K^{(e)}$; $K_{I_i^{(e)} I_j^{(e)}}$ is the $I_i^{(e)}$ row $I_j^{(e)}$ column component of matrix K; $I_i^{(e)}$ is the ith component of the index matrix).

4) Iterate 2 and 3 for all elements.

APPENDIX III

The displacement boundary condition can be defined as $\delta_{\mathrm{sub}} = \delta_c$, where δ_{sub} is a vector that is composed of a subset of the components of the global nodal displacement vector δ; δ_c is a known constant vector that specifies the nodal boundary displacement. For example, a common displacement boundary condition for the object meshed by our 9-node example shown in Fig. 2 is to compress the top side downward 1% of the total height of the object while the bottom is fixed vertically. This example displacement boundary condition can be defined as $\delta_{\mathrm{sub}} = (\delta_2 \quad \delta_4 \quad \delta_6 \quad \delta_8 \quad \delta_{26} \quad \delta_{28} \quad \delta_{30} \quad \delta_{32})^T$ and $\delta_c = (0 \quad 0 \quad 0 \quad 0 \quad 0.01h \quad 0.01h \quad 0.01h \quad 0.01h)^T$, where h is the height of the object. The penalty approach can be expressed as the following seven steps.

1) Initialize the global force vector f as a null vector.
2) Select a large number L (a choice for L is $L = max|K| \times 10^4$ as suggested by Chandrupatla [41].
3) According to δ_{sub}, set the corresponding f_{sub} to $L \times \delta_c$ ($f_{\mathrm{sub}} = (f_2 \quad f_4 \quad f_6 \quad f_8 \quad f_{26} \quad f_{28} \quad f_{30} \quad f_{32})^T$ for the given example).
4) According to δ_{sub}, add L to the corresponding diagonal component of K (for our example, these diagonal components are $K_{2,2}, K_{4,4}, K_{6,6}, K_{8,8}, K_{26,26}, K_{28,28}, K_{30,30},$ and $K_{32,32}$).
5) Solve $K\delta = f$ for δ.
6) Calculate reaction force $f_{\mathrm{sub}} = -L(\delta_{\mathrm{sub}} - \delta_c)$.
7) Replace δ_{sub} with δ_c.

REFERENCES

[1] C. P. McPherson, K. K. Swenson, G. Jolitz, and C. L. Murray, "Survival among women ages 40–49 years with breast carcinoma according to method of detection," *Cancer*, vol. 79, no. 10, pp. 1923–1932, 1997.

[2] A. Sarvazyan, "Mechanical imaging: A new techonology for medical diagonsis," *Int. J. Med. Inform.*, vol. 49, pp. 195–216, 1998.

[3] P. S. Wellman, "Tactile imaging," Ph.D. dissertation, Dept. Eng. Sci., Harvard Univ., Cambridge, MA, 1999.

[4] E. I. Cespedes, J. Ophir, H. Ponnekanti, and N. Maklad, "Elastography: Elasticity imaging using ultrasound with application to muscle and breast *in vivo*," *Ultrasound Imag.*, vol. 15, pp. 73–88, 1993.

[5] E. Chen, R. Adler, P. Carson, W. Jenkins, and W. O'Brein, "Ultrasound tissue displacement imaging using ultrasound with application to muscle and breast cancer," *Ultrasound Med. Biol.*, vol. 21, pp. 1153–1162, 1995.

[6] B. S. Garra, E. I. Cespedes, J. Ophir, S. R. Spratt, R. A. Zuubrier, C. M. Magnant, and M. F. Pennanen, "Elastography of breast lesions: Initial clinical results," *Radiology*, vol. 202, pp. 79–86, 1997.

[7] T. J. Hall, Y. Zhu, and C. S. Splading, "*In vivo* real-time freehand palpation imaging," *Ultrasound Med. Biol.*, Oct. 2002.

[8] S. Y. Emelianov, M. A. Lubinski, W. F. Weiztel, R. C. Wiggins, A. R. skovoroda, and M. O'Donnell, "Elasticity imaging for early detection of renal pathology," *Ultrasound Med. Biol.*, vol. 21, pp. 871–883, 1995.

[9] P. Chatruvedi, M. F. Insana, and T. J. Hall, "Acoustic and elastic imaging to model disease-induced changes in soft tissue structure," in *Lecture Notes in Computer Science*, A. Kuba and M. Samal, Eds. New York: Springer-Verlag, 1997, vol. 1230, pp. 1–14.

[10] F. Kallel, J. Ophir, K. McGee, and T. Krouskop, "Elastographic imaging of low-contrast elastic modulus distributions in tissue," *Ultrasound Med. Biol.*, vol. 24, pp. 409–425, 1998.

[11] T. J. Hall, H. A. Khant, M. F. Insana, J. G. Wood, Y. Zhu, D. Preston, and B. D. Cowley, "The utility of quantitative ultrasound for tracking the progression of polycystic kidney disease," *Proc. SPIE*, vol. 3982, pp. 161–171, 2000.

[12] B. M. Shapo, J. R. Crowe, A. R. Skovoroda, M. J. Eberle, N. A. Cohn, and M. O'Donnel, "Displacement and strain imaging of coronary arteries with intraluminal ultrasound," *IEEE Trans. Ultrason., Ferroelect. Freq. Contr.*, vol. 43, pp. 234–246, Mar. 1996.

[13] L. K. Ryan and F. S. Foster, "Ultrasonic measurement of differential displacement and strain in a vascular model," *Ultrason. Imag.*, vol. 19, pp. 19–38, 1997.

[14] Y. C. Fung, *A First Course in Continuum Mechanics*. Englewood Cliffs, NJ: Prentice-Hall, 1994.

[15] T. A. Krouskop, D. R. Dougherty, and F. S. Vinson, "A pulsed doppler ultrasonic system for making noninasive measurement of the mechanical properties of soft tissue," *J. Rehab. Res. Dev.*, vol. 24, pp. 1–8, 1987.

[16] R. M. Lerner, S. R. Huang, and K. J. Parker, "Sonoelasticity images derived from ultrasound signals in mechanically vibrated tissues," *Ultrasound Med. Biol.*, vol. 16, no. 3, pp. 231–239, 1990.

[17] Y. Yamakoshi, J. Sato, and T. Sato, "Ultrasonic imaging of internal vibration of soft tissue under forced vibration," *IEEE Trans. Ultrason., Ferroelect. Freq. Contr.*, vol. 37, pp. 45–53, Mar 1990.

[18] L. Sandrin, S. Catheline, M. Tanter, X. Hannequin, and M. Fink, "Time-resolved pulsed elastography with ultrafast ultrasonic imaging," *Ultrason. Imag.*, vol. 21, no. 4, pp. 259–272, 1999.

[19] R. J. Dickinson and C. R. Hill, "Measurement of soft tissue mation using correlation between a-scans," *Ultrasound Med. Biol.*, vol. 8, no. 3, pp. 263–271, 1982.

[20] L. S. Wilson and D. E. Robinson, "Ultrasonic measurement of small displacements and deformations of tissue," *Ultrason. Imag.*, vol. 4, pp. 71–82, 1982.

[21] M. Tristam, D. C. Barbosa, D. O. Cosgrove, D. K. Nassiri, J. C. Bamber, and C. R. Hill, "Ultrasonic study of *in vivo* kinetic characteristics of human tissues," *Ultrasound Med. Biol.*, vol. 12, no. 12, pp. 927–937, 1986.

[22] J. Ophir, I. Cespedes, H. Ponnekanti, Y. Yazdi, and X. Li, "Elastography: A quantitive method for imaging the elasticity of biological tissues," *Ultrason. Imag.*, vol. 13, pp. 111–134, 1991.

[23] M. O'Donnell, A. Skovoroda, B. Shapo, and S. Emelianov, "Internal displacement and strain imaging using ultrasonic speckle tracking," *IEEE Trans. Ultrason., Ferroelect. Freq. Contr.*, vol. 41, pp. 314–325, May 1994.

[24] M. Bilgen and M. F. Insana, "Deformation models and correlation analysis in elastography," *J. Acoust. Soc. Amer.*, vol. 99, pp. 3212–3224, 1996.

[25] K. A. Wear and R. L. Popp, "Theoretical analysis of a technique for the characterization of myocardium contraction based upon temporal correlation of ultrasound echoes," *IEEE Trans. Ultrason., Ferroelect. Freq. Contr.*, vol. UFFC-34, pp. 368–375, 1987.

[26] R. Adler, J. Rubin, P. Bland, and P. Carson, "Quantitive tissue motion analysis of digitized m-mode images: Gestational differences of fetal lung," *Ultrasound Med. Biol.*, vol. 16, pp. 561–569, 1990.

[27] P. DeJong, T. Arts, A. Hoeks, and R. Reneman, "Determination of tissue motion velocity by correlation interpolation of pulsed ultrasonic echo signals," *Ultrason. Imag.*, vol. 12, pp. 84–98, 1990.

[28] Y. Zhu and T. J. Hall, "A modified block matching method for realtime freehand strain imaging," *Ultrason. Imag.*, Nov. 2002.

[29] R. Muthupillai and R. L. Ehman, "Magnetic resonance elastography," *Nat. Med.*, vol. 2, no. 5, pp. 601–603, 1996.

[30] A. M. T. E. Oliphant, M. A. Dresner, J. L. Mahowald, S. A. Kruse, E. Amromin, J. P. Felmlee, J. F. Greenleaf, and R. L. Ehman, "Magnetic resonance elastography: Non-invasive mapping of tissue elasticity," *Med. Image Anal.*, vol. 5, no. 4, pp. 237–254, 2001.

[31] J. B. Weaver, E. E. V. Houten, M. I. Miga, F. E. Kennedy, and K. D. Paulsen, "Magnetic resonance elastography using 3D gradient echo measurements of steady-state motion," *Med. Phys.*, vol. 28, no. 8, pp. 1620–1628, 2001.

[32] D. D. Duncan and S. J. Kirkpartrick, "Processing algorithms for tracking speckle shifts in optical elastography of biological tissues," *J. Biomed. Opt.*, vol. 6, no. 4, pp. 418–426, 2001.

[33] A. R. Skovoroda, S. Y. Emelianov, and M. O'Donnell, "Tissue elasticity reconstruction based on ultrasonic displacement and strain images," *IEEE Trans. Ultrason., Ferroelect. Freq. Contr.*, vol. 42, pp. 747–765, July 1995.

[34] F. Kallel and M. Bertrand, "Tissue elasticity reconstruction using linear perturbation method," *IEEE Trans. Med. Imag.*, vol. 15, pp. 299–313, June 1996.

[35] M. M. Doyley, P. M. Meaney, and J. C. Bamber, "Evaluation of an iterative reconstruction method for quantitative elastography," *Phys. Med. Biol.*, vol. 45, pp. 1521–1540, 2000.

[36] T. A. Krouskop, T. M. Wheeler, F. Kallerl, B. S. Garra, and T. J. Hall, "Elastic moduli of breast and prostate tissues under compression," *Ultrason. Imag.*, vol. 20, pp. 260–274, 1998.

[37] K. R. Raghavan and A. E. Yagle, "Forward and inverse problems in elasticity imaging of soft-tissue," *IEEE Trans. Nucl. Sci.*, vol. 41, pp. 1639–1648, Aug. 1994.

[38] A. J. Romano, J. J. Shirron, and J. A. Bucaro, "On the noninvasive determination of material parameters from a knowledge of elastic displacements: Theory and numerical simulation," *IEEE Trans. Ultrason., Ferroelect. Freq. Contr.*, vol. 45, pp. 751–759, May 1998.

[39] K. H. Huebner, E. A. Thornton, and T. G. Byrom, *The Finite Element Method for Engineers*, 3rd ed. New York: Wiley, 1995.

[40] Y. W. Kwon and H. Bang, *The Finite Eement Method Using MATLAB*, 2nd ed. New York: CRC, 2000.

[41] T. R. Chandrupatla and A. D. Belegundu, *Introduction to Finite Elements in Engineering*, 2nd ed. Englewood Cliffs, NJ: Prentice-Hall, 1997.

[42] W. H. Press, S. A. Teukolsky, W. T. Vetterling, and B. P. Flannery, "Numerical Recipes in C," in *The Art of Scientific Computing*, 2nd ed. Cambridge, MA: Cambridge Univ. Press, 1992.

[43] M. Bilgen and M. F. Insana, "Convariance analysis of time delay estimates for strained signals," *IEEE Trans. Signal Processing*, vol. 46, pp. 2589–2600, Oct. 1998.

[44] E. E. V. Houen, K. D. Paulsen, M. I. Miga, F. E. Kennedy, and J. B. Weaver, "An overlapping subzone technique for MR-based elastic property reconstruction," *Magn. Reson. Med.*, vol. 42, no. 4, pp. 779–786, 1999.

[45] T. Wu, J. P. Felmlee, J. F. Greenleaf, S. J. Riederer, and R. L. Ehman, "Assessment of thermal tissue ablation with MR elastography," *Magn. Reson. Med.*, vol. 45, no. 1, pp. 80–87, 2001.

Noise Reduction Strategies in Freehand elasticity Imaging

Timothy J. Hall, Jingfeng Jiang, Yanning Zhu, Larry T. Cook
Department of Radiology, University of Kansas Medical Center
3901 Rainbow Boulevard, Kansas City, KS 66160-7234

Abstract— We are developing a clinical ultrasonic imaging system for real-time estimation and display of tissue elastic properties. We have demonstrated that real-time feedback of elasticity images is essential for obtaining high-quality data (consecutive images with high spatial coherence). The key element to successful scanning is real-time visual feedback which guides the patient positioning and compression direction. Our data have clearly demonstrated nonlinearity in the strain properties of different tissue types. We have also demonstrated that a comparison of the area of a breast lesion observed in strain images versus B-mode images is a sensitive criterion for differentiating malignant from benign tumors. Frame-to-frame variability in strain images somewhat degrades the ability to observe these phenomena. Three strategies for reducing frame-to-frame strain image noise are described. The combination of these post-processing strategies provides a signicant improvement in the quality of long sequences of strain images.

I. Introduction

We are implementing and testing real-time mechanical strain imaging integrated into a clinical ultrasound imaging system (Elegra, Siemens Medical Solutions) [1]. Our work was motivated by promising *in vivo* results reported by Garra et al. [2]. In that report they described data acquisition based on a modied mammography system. The use of that system limited the areas of the breast from which they could acquire data.

Freehand scanning has been the dominant method of clinical sonography for many years. So, freehand scanning will likely more quickly gain clinical acceptance of elasticity imaging if it can be performed efciently . We have argued that real-time feedback to the hand-eye coordination system allows constant manipulation of the boundary conditions of deformation and allows the observer to know when high quality strain image data are acquired. The small delay between acquiring successive frames (tens of milliseconds) and the relatively slow deformation rate (cyclic freehand deformation at about 1 Hz) likely results in primarily an elastic response in tissue (minimal viscous effect) [3].

In vivo elasticity images of breast lesions obtained with our system have high contrast-to-noise ratios. In fact, relatively long sequences (30 sequential frames or more) of high quality strain images are normally obtained in clinical trials. An example image from a breast tumor is shown in Fig. 1. Using our system we have demonstrated that broadenomas often have a surface pressure-dependent strain image contrast [1]. The strain image contrast for a broadenoma is generally highest with the least surface pressure and contrast decreases as the pressure is increased. In addition, the relative size of a lesion in B-mode versus strain images is a sensitive criterion for differentiating malignant from benign lesions [1, 2]. A plot of lesion area measured in B-mode images versus lesion area in the corresponding strain images (Fig. 2) illustrates this performance.

Viewing strain image sequences allows visualization of strain image noise that is not apparent in single strain images. Given that pressure dependent strain image contrast and the relative lesion size comparison are useful criteria for differentiating breast lesions, reducing that frame-to-frame variability in strain estimates will improve the ability to visualize that varying contrast and better determine lesion boundaries.
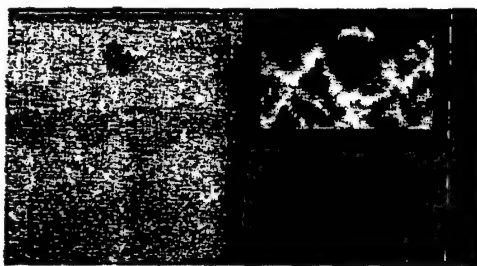
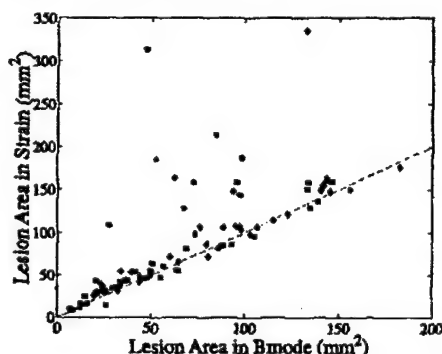Fig. 1. A B-mode and strain image pair obtained by freehand scanning of a breast carcinoma *in vivo*.

Fig. 2. A comparison of lesion area for carcinomas (circles), cysts (squares) and fibroadenomas (diamonds).

Strategies for reducing that frame-to-frame variability in local strain estimates is the subject of this report. The goal is to reduce noise while maintaining spatial resolution. An additional goal is to obtain reduction in strain image noise with minimal incremental computational load such that the technique can be implemented in on-line processing for clinical trials. Several possible approaches are suggested, and results of implementing those approaches are encouraging.

II. MATERIALS AND METHODS

Strain Image Formation

A 2-D block matching algorithm, based on the sum-squared difference (SSD) algorithm, is used for motion tracking in our implementation. The kernel size was selected to approximate the 2-D pulse-echo ultrasound point spread function for the system employed (Siemens SONOLINE Elegra with 7.5L40 and VFX13-5 linear arrays). Data were processed on the

image processor subsystem of the Elegra. The algorithm displays streaming B-mode and strain images side-by-side at about seven frames per second and stores the full sequence of I-Q echo data for on-line post-processing.

Patient Scanning

All patients provided informed consent consistent with the protocol approved by the Human Subjects Committee (Institutional Review Board) at Kansas University Medical Center. Patient scans were performed in a manner consistent with a normal breast ultrasound exam; the breast was scanned with the patient (typically) in the supine position with her arm behind her head. When the breast lesion was located, the transducer was pressed toward the chest wall at a steady rate in an effort to achieve about 0.5–1.2% compression frame-to-frame while repeating the compress/release cycle for relatively large (>10%) compression. The compression technique was adjusted, by changing the compression direction or patient position, until there was nearly uniaxial compression with minimal elevation motion. Real-time B-mode and strain image display allowed visualization of the data quality. Using this scanning technique, no patient has experienced any discomfort in our procedures.

III. SOURCES OF NOISE AND STRATEGIES FOR IMPROVED RESULTS

Small Deformation–Low Average Strain

The strain image contrast-to-noise ratio increases as the applied (uniaxial) strain increases for frame-average strains up to about 5% (see, for example [4]). Freehand deformation sometimes results in nonuniform frame-to-frame average strain. The pairing of rf echo frames of data in post-processing can be adjusted to select appropriate frame pairs to obtain, nominally, 1–1.5% frame-average strain [5]. A representative result for a *in vivo* breast fibroadenoma is shown in figure 3.

Large Displacement Errors

Regardless of the average applied strain, the motion tracking algorithm, and whether that strain was applied with freehand scanning or motorized deformation, displacement estimation errors sometime occur. When
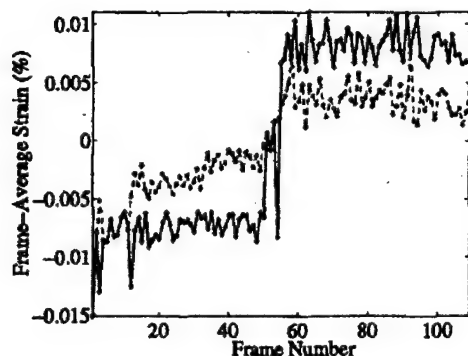
Fig. 3. The frame-to-frame strain obtained by freehand scanning of a breast *in vivo* and pairing adjacent frames (dashed) or dynamically adjusting the frame pairing in post-processing (solid) for strain estimation.
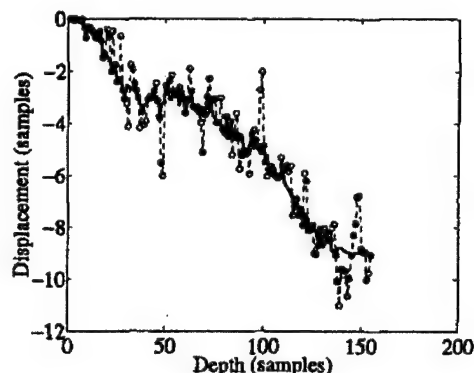

Fig. 4. Displacement estimates resulting from 2-D block matching (dashed) and moving linear regression (solid) for those results as a function of depth for one line of data.

using a very small 2-D kernel to track motion, relatively large errors are easily detected. A statistical argument and a moving linear regression can be used to detect displacement estimates that are so different from their neighbors that they are very unlikely to be correct. For example, if we know that adjacent displacement estimates differences of one sample imply a local strain of 7%, and the frame-average strain is only about 1%, then adjacent displacement estimate differences of more than one sample are extremely unlikely. We can use linear regression to estimate the local displacement and compare each estimate to the local regression fit. If the difference between the individual estimate and the regression value is more than some threshold, for example one sample, that estimate is judged to be in error and is replaced by the regression value. This approach is very effective at detecting and removing large displacement errors prior to estimating local strain. An example of this technique applied to *in vivo* breast data is shown in Fig. 4.

It is straightforward to extend this approach and fit local displacement estimates to a small (planar) surface to detect and exclude large errors. The advantage of using a surface fit is that it minimizes local axial shear. The size of the surface, as with the linear regression window, is a tradeoff between tracking true displacements (resolution) with small surfaces and rejecting consecutive displacement errors (noise reduction) with a longer window. A 2 mm × 2 mm surface provides subjectively satisfactory results.

Complex Motion

Correlation search techniques for motion tracking, such as that employed for our real-time strain imaging, work well when the deformation is small and the motion is relatively simple [6]. When the motion is relatively large (>5% strain) or includes obvious shear the performance of correlation search techniques degrades. Under these conditions higher order motion models typically improve motion tracking performance but at higher computational load [7].

In these techniques, a cost function is defined that minimizes the constraints used to model the motion. The basic approach assumes that the brightness of each point in the image remains constant from one frame of data to the next. A brightness constraint, E_b, is then used to estimate the deformation field that describes the transformation from one frame of data to the next. That general concept was adapted to rf echo samples, instead of B-mode pixel brightness in our previous work [8]. Our current approach uses the sum squared difference between pre- and warped post-compression echo fields as the brightness constraint. A smoothness constraint, E_s, is added to the cost function to place a penalty on large deviations from average local motion. Numerous approaches to create smoothness constraints have been reported. One of the earliest smoothness constraints was reported by Horn [9].

From our previous work using similar techniques [8] we recognized the importance of the constraint function in the overall performance of this approach. We

are investigating the use of strain energy as a smoothness constraint function, as suggested by Bajscy [10]. The resulting cost function is

$$C = \iint\limits_{\Omega} (\gamma E_b + E_s) dx dy \qquad (1)$$

where γ is an adaptively chosen scale factor. Example images of the same data with and without these noise reduction strategies are shown in Figs. 5 and 6.
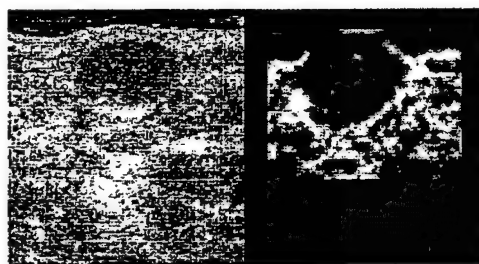

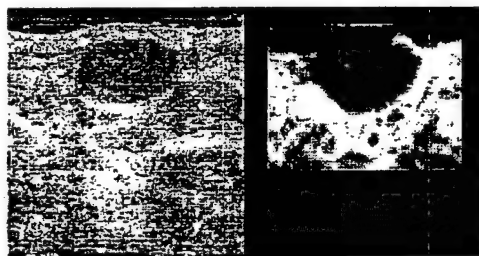Fig. 5. A B-mode and strain image pair without noise reduction.

Fig. 6. A B-mode and strain image pair with all three noise reduction strategies.

IV. DISCUSSION

Real-time display of side-by-side B-mode and strain images is essential for guiding the manipulation of boundary conditions for the mechanics experiment that is strain imaging. The real-time feedback to the hand-eye coordination systems allows the sonographer to manipulate the compression direction, force, and rate to obtain high-quality sequences of strain images. The system involves no remote data acquisition or display, and no additional signal processing hardware. It is fully integrated into the Elegra system.

The sequence of B-mode and strain image pairs allows the sonographer to select images representative of the "typical" strain image for a lesion. This ability, along with better determination of lesion boundary available by viewing a sequence of images, has likely improved the ability to measure true lesion size in strain imaging compared with the results reported by Garra, et al.

Deformable model approaches are iterative and require an initial displacement field approximation. When that approximation has large errors, accurate displacement estimates are influenced by the presence of local displacement errors. By first using the above techniques to minimize local displacement errors, we start the deformable model iteration with a reasonable approximation to the true displacement field. The result is a significant reduction in frame-to-frame variability in strain images and improved detection of lesion boundaries and contrast changes.

V. CONCLUSIONS

Strategies for reducing strain image noise in a sequence of strain images are described. Tests of these strategies on breast data acquired *in vivo* demonstrate improvements in the image sequence. In combination these strategies provides significant improvements in the visual interpretation of a sequence of strain images.

REFERENCES

[1] T. J. Hall, Y. Zhu, and C. S. Spalding, "In vivo real-time free-hand palpation imaging," *Ultrasound Med Biol*, p. accepted for publication, 2002.

[2] B. S. Garra, I. Céspedes, J. Ophir, S. R. Spratt, R. A. Zuurbier, C. M. Magnant, and M. F. Pennanen *Radiology*, vol. 202, pp. 79–86, 1997.

[3] T. A. Kroukop, W. TM, F. Kallel, B. S. Garra, and T. J. Hall *Ultrasonic Imaging*, vol. 20, pp. 260–274, 1998.

[4] P. Chaturvedi, M. F. Insana, and T. J. Hall *IEEE Trans Ultrason, Ferroelec, Freq Cont*, vol. 45, no. 4, pp. 1022–1031, 1998.

[5] M. A. Lubinski, S. Y. Emelianov, and M. O'Donnell *IEEE Trans Ultrason, Ferroelec, Freq Cont*, vol. 46, no. 1, pp. 97–107, 1999.

[6] G. E. Trahey, J. W. Allison, and O. T. von Ramm *IEEE Trans Biomed Eng*, vol. BME-34, pp. 965–967, 1987.

[7] G. E. Maillioux, A. Bleau, M. Bertrand, and R. Petitclerc *IEEE Trans Biomed Eng*, vol. BME-34, pp. 356–364, 1987.

[8] Y. Zhu, P. Chaturvedi, and M. Insana *Ultrasonic Imaging*, vol. 21, pp. 127–146, 1998.

[9] B. K. Horn, *Robot Vision*. Cambridge, MA: MIT Press, 1986.

[10] R. Bajscy and S. Kovacic *Computer vision, graphics and image processing*, vol. 46, pp. 1–21, 1989.

Beyond the Basics: Elasticity Imaging with Ultrasound

Timothy J. Hall, Ph.D.
Medical Physics Department, University of Wisconsin-Madison,
1530 Medical Sciences Center, 1300 University Avenue, Madison, WI, 53717-1532
USA.
Telephone: (608) 265-9459
FAX: (608) 262-2413
e-mail: tjhall@wisc.edu

Beyond the Basics: Elasticity Imaging with Ultrasound

Abstract

A new mode of imaging with ultrasound is under development in several laboratories around the world. The new mode estimates some measure of the viscoelastic properties of tissue. The information displayed in these images is a surrogate for that obtained with manual palpation. This report reviews some of the fundamental concepts in elasticity imaging and highlights the development of a system for a real-time elasticity imaging being tested for in vivo breast and thyroid imaging. Results of early laboratory tests that motivated this effort are reviewed and results obtained using this system with in vivo tissues are included. Imaging the elasticity of in vivo breasts suggest that invasive ductal carcinomas appear, on average, more than twice as large in an elasticity image compared to the same lesion in an ultrasound B-mode image, but fibroadenomas and cysts are nearly equal in size in the two image types. Data from that real-time system also demonstrate that the relative stiffness of many fibroadenomas change as they, and their surrounding tissue, are deformed. The utility of this technology, and the new information it provides, suggests that it might soon be available on commercial ultrasound imaging systems.

Summary Statement
Elasticity imaging could significantly improve the diagnosis of breast abnormalities using ultrasound.

INTRODUCTION

It is the experience of many that palpation, pressing on the surface of soft tissue in an effort to 'feel' abnormalities, is a commonly used diagnostic tool. This tool has been used for thousands of years and is the primary diagnostic tool for some diseases. Examples include breast self examination for sensing breast 'lumps' and digital rectal examination for prostate cancer. Palpation is known to be subjective and it lacks sensitivity to small abnormalities that are deep beneath the skin surface.

Improving sensitivity and reducing the subjectivity of palpation could have a significant impact on breast cancer prognosis. Breast cancer is the second-leading cause of cancer deaths in women. Over 200,000 new cases of invasive breast cancer are expected in the USA this year alone. It is anticipated that approximately 40,000 women in the USA will die of breast cancer in 2003. The prognosis for breast cancer patients is best when the disease is detected at an early stage. Specifically, 5- and 10-year survival statistics are best when cancer is noninvasive[1] and is less than 1cm in diameter.[2] Improvements in mammography have resulted in improved detection of breast lesions, and mammography has been shown capable of detecting smaller tumors in young women than either breast self-examination or clinical breast examination.[3] However, mammography is not infallible. Approximately 15% of palpable breast cancers are not detectable with mammography, and this number is likely higher in younger women.[4] A combination of clinical palpation with either mammography or sonography has been shown to significantly increase the sensitivity and specificity of breast cancer detection.[5] One of the greatest difficulties in mammography is imaging the radiographically dense breast. Unfortunately, women with mammographically-dense breasts have a risk of breast cancer that is 1.8—6.0 times greater than that of women the same age with little or no mammographic density.[6] Small lesions become much more difficult to detect when obscured by dense connective tissues and ducts. Several recent studies have demonstrated that sonography has higher sensitivity for breast cancer detection than mammography alone,[7] mammography combined with physical examination,[7,8] or mammoscintigraphy.[9] Furthermore, the sensitivity of mammography decreases significantly with increasing mammographic density.[7,10] Hormone replacement therapy reduces the sensitivity of x-ray mammography[11] and increases the need for alternate diagnostic tools.

In an effort to improve the sensitivity of palpation and provide quantitative measures of 'palpable,' research groups around the world are actively working toward imaging technologies that display quantitative maps of 'tissue stiffness.' This report describes the physics of palpation and uses that information to understand the limitations of palpation. That basic physical understanding is then used to describe the various approaches to these imaging technologies. The emphasis then turns to elasticity imaging systems and the development of an elasticity imaging system that is implemented on commercial sonography system and displays real-time elasticity images with freehand scanning. Results of preliminary tests of the utility of that system for diagnosing breast abnormalities are then described.

Previous reviews of elasticity imaging using ultrasound are available.[12,13] This report updates those prior reviews and emphasizes a specific real-time elasticity imaging system and results obtained with that system.

4

The physics of palpation

An understanding of how palpation works can be obtained by examining the basic physics of applying an external deformation to an object. Begin with a simple model of forces and deformation. A standard concept presented in introductory physics is the elastic deformation of a simple spring (a 1-dimensional object) due to a known applied force. Figure 1 illustrates the typical simple experiment to study elasticity. A known mass suspended from a simple spring results in a measurable elongation of that spring. Suspending a different known mass results in a different elongation of the spring. Each mass in the standard gravitational field of the earth places a known force on the spring. The difference in these forces and the difference in the elongations of the spring due to those forces can be combined using Hooke's law to estimate the spring constant, k, which is characteristic of the spring and quantifies its 'stiffness.'

To extend the concept of force and deformation to a 3-dimensional (3-D) object, consider separately the forces and resulting displacements. The analysis will be simplified by assuming that the material is homogeneous and isotropic (meaning that the material properties are uniform in composition without any directional dependence in elasticity). Ignore the class of forces, called 'body forces,' which act on all volume elements of the material (such as gravity and inertia). The class of forces to consider is called 'surface forces' because they have units of force per unit area and can be viewed as acting on a surface element of the object. That surface element is not necessarily on the exterior boundary of the object, but can be a surface of an arbitrary interior volume element. The orientation of that surface is described by a vector that is perpendicular to the surface element (a normal vector), thus a 3-D coordinate system (x_i, i=1,2,3 or x_1,x_2,x_3) is required to describe the normal vector. A force acting on that surface element has a magnitude and direction (force is a vector quantity), and the direction of that force is not necessarily perpendicular to the surface element. Thus, to describe the direction of the force vector also requires a 3-dimensional coordinate system (y_j, j=1,2,3). To maintain generality and simplicity (to obtain principle components) in the description of the surface force two separate 3-D coordinate systems are used (x_i and y_j). Collapsing the arbitrary surface element to a point we obtain a 'stress tensor.' A tensor is a generalization of the concept of a vector; tensor calculus is used to study the derivatives of vector fields. The stress tensor, σ_{ij}, is a 3x3 matrix corresponding to the nine combinations available by combining the two independent 3-D coordinate systems of the force and the surface element on which it acts.

Similarly, consider the displacement of a volume element acted on by an external force. If the motion does not involve a change of volume or shape of the object, the motion is termed 'rigid body motion.' If, on the other hand, the object is deformed (changes shape or volume) as a result of the external force the description of motion is again more complex. A 3-D coordinate system is required to describe the motion in space. To maintain generality and simplicity (to obtain principle components) in the description of the gradients (spatial rate of change) of that deformation (strain is the spatial rate of change of displacement) another 3-D coordinate system is required. The strain tensor, ε_{kl}, is thus another 3x3 matrix corresponding to the nine combinations available by combining these two independent 3-D coordinate systems.

An equation to relate the nine-component stress tensor to the nine-component strain tensor is called a constitutive equation. The form of the constitutive equation

5

depends on whether a material is a fluid (an ideal fluid with no viscosity or a Newtonian viscous fluid), purely elastic (e.g., an idealized solid) or viscoelastic (neither purely viscous nor purely elastic). In a purely elastic (lossless) deformation, the stress is dependent only on the strain

$$\sigma_{ij} = C_{ijkl}\, \varepsilon_{kl}\,.$$

This equation is analogous to Hooke's law for the 1-D spring, but it accounts for forces and deformations in all three directions. The quantity C_{ijkl} is the 'modulus tensor' of elastic coefficients and is the equivalent of the spring constant, k, used to describe the deformation of a spring. The four subscripts indicate that four sets of 3-D coordinate systems are required for a general description of the relationship between the stress and strain tensors, and thus, C_{ijkl} has (3^4) 81 components. The stress and strain tensors are symmetric and therefore each contains at most six independent components. Therefore, the modulus tensor for infinitesimal elastic deformations is also symmetric and contains at most 36 independent components. It can be shown[14] that by assuming a material to be completely isotropic, the number of independent elastic coefficients is reduced to two (called the Lamé constants). A more detailed description of stress and strain can be found in any text on continuum mechanics (see, for example, reference 15).

The elastic coefficients that describe the behavior of a material are absolute measures of intrinsic properties of the material. Estimating these quantities requires measurements of stresses and strains under well-characterized experimental conditions. For example, the viscoelastic properties of many soft tissues under cyclic uniaxial loading are found to depend on the strain range, the strain rate, measurement temperature, etc.[16] It is often easier to simplify the experiment and only measure components of the surface stress distribution or the internal strain distribution. The drawback is that stress or strain alone are relative quantities and are not intrinsic to the material under study.

The basic physics of elasticity (stress and strain) can be used to understand the limitations of palpation. Engineers often use a computational tool called 'finite element analysis' (FEA) to study the behavior of objects under external forces or deformations. FEA was used to simulate the stress and strain involved when deforming a uniform block containing a spherical inclusion, as shown in Figure 2. The upper surface of the block is uniformly displaced by 1% of the total height. The lower surface is allowed to move freely laterally and the sides have unrestricted motion. The simulation shows the distribution of stress and profiles of that stress distribution are plotted on the right. In palpation, the fingers press on the tissue to deform it and then sense the stress distribution that results. The simulation shows that as the sphere moves further away from the surface (profile further from the sphere), the variation in stress across the profile decreases suggesting that the sphere would be more difficult to palpate (less stress contrast available to the fingers to sense) as it is placed deeper in the block.

In vitro tissue studies

The most common approach to studying the viscoelastic properties of soft tissues is to sinusoidally deform in vitro samples of tissue, measure the force required to induce the deformation and study the phase relationship between force and displacement. In vitro studies of the viscoelastic properties of breast tissue[13,17] have demonstrated several findings that are significant to elasticity imaging (see Table 1). First, for cyclic load-unload experiments, there is little phase delay between the sinusoidal deformation and

response (strain and stress) for compression frequencies near 1Hz. This shows that the energy required to deform the tissue is nearly completely recovered when the deforming force is released (nearly lossless deformation). Thus, in vitro breast tissue behaves as a nearly completely elastic medium at these strain rates, and the viscous component can be ignored. These deformation motion frequencies are typical of that used in clinical ultrasound breast exams with compression. Second, the stress-strain relationship for most breast tissues is non-linear, and the degree of non-linearity varies with tissue type. (Materials with linear stress-strain relationships exhibit stress that is directly proportional to strain; that is, they exhibit constant 'stiffness.' Materials with nonlinear stress-strain relationships change stiffness, most commonly getting stiffer, as they are deformed.) Third, the elastic moduli of breast tissue, obtained from the slope of the stress-strain curves, vary significantly among breast tissue types and strain range. In summary, breast tissue is mostly elastic for the strain rates likely encountered with freehand scanning, object contrast is likely high in strain and modulus images, contrast will likely be different for different lesion types, and contrast will likely change with increasing compression.

Imaging the elastic properties of tissue

Approaches to elasticity imaging can be classified by the modality of the signal source (primarily ultrasound or MRI), the mechanical parameter estimated (e.g., stress, strain, or modulus), or a descriptor of the experimental procedure ("dynamic" or "(quasi-)static" techniques). The mechanical properties estimated with these techniques are related. As described above, stress and strain are mutually responsive quantities, but they are not intrinsic material properties. Images of stress and strain are maps of a parameter relative to its surroundings (as a mammogram maps the relative x-ray attenuation, for example). Elastic moduli are intrinsic material properties generally described with a matrix (as described above), but for practicality experimental conditions are manipulated and material properties (such as incompressibility, homogeneity and isotropy) are assumed so that the size of this matrix is reduced to one or two parameters.

Several research groups are developing techniques for imaging the stress distribution. Most notable among the stress imaging techniques is the work from Wellman, et al.,[18] using a piezo-resistive sensor array (TekScan, Inc., Boston, MA) coupled to a position tracking system. This system closely mimics the mechanics of palpation and demonstrates a strong correlation between the size of the lesion measured with the tactile system and the lesion size measured following resection. The performance for small lesions (less than 10mm) that are relatively deep (more than 10mm) remains to be seen. Also noteworthy is the work of Sarvazyan[19] in which he attempts to solve the inverse problem of determining the 3-D modulus distribution that causes the measured surface pressure distribution.

Strain imaging has received the most attention in elasticity imaging. The earliest implementations used M-mode acquisition and cross correlation to track tissue motion and study tissue elasticity.[20,21] In later studies Doppler processing techniques were used to track differences in motion[22,23] and "sonoelasticity imaging" soon followed.[24] The Doppler processing techniques were the first "dynamic techniques" and derived their data from ultrasound. 'Static compression elastography' is the most common approach to

strain imaging. Numerous groups are pursuing ultrasound-based strain imaging with efforts in algorithm development,[25,26,27,28,29] performance evaluation,[30,31,32] and clinical testing[33,34] (representative citations).

The basic information derived in strain imaging techniques is the relative tissue displacement. An imaging system (typically ultrasound or MRI) acquires (pre-deformation) data corresponding to a map of tissue anatomy. A small deformation is applied, either through an external compressor or physiological function (breathing, cardiac pressure variations, etc.), and another (post-deformation) map of the anatomy is acquired. The displacement field in the deformed tissue is estimated by comparing these two maps of anatomy. Mechanical strain is estimated by calculating the gradient (the spatial rate of change) of the displacement field. In ultrasound the displacement along the acoustic beam propagation (axial) direction can be estimated far more accurately and with higher precision than in the lateral or elevational directions.[32]

An important aspect for clinical acceptance of ultrasound strain imaging is the technique for deforming the soft tissue between image pairs. Most phantom experiments in the literature used motorized compression devices and extensive fixtures. These devices are not likely to gain clinical acceptance because they either limit the locations that strain imaging can be applied or are time consuming to incorporate. Freehand scanning, where tissue is deformed with the surface of the transducer, is desirable.[33,34,35]

Developing a real-time strain imaging system that allows freehand scanning is essential for clinical utilization. The strain imaging algorithm must be computationally efficient, insensitive to motion irregularities and track tissue motion in 2-D (eventually 3- and 4-D). Block matching (template matching) algorithms are widely used in image processing applications for tracking motion. The most notable application is movie image compression algorithms such as MPEG. The use of block matching in ultrasonic imaging was first reported by Trahey, et al. for blood flow estimation.[36] Block matching is a good candidate since it is simple in principle and is capable of tracking motion in 2-D. However, for strain imaging, the algorithm needs to be modified to increase its computational efficiency and insensitivity to decorrelation noise.[29] (Decorrelation is a measure of how similar two signals are. That similarity is measured with cross correlation or surrogate measures of correlation. Echo signals decorrelate when there is high electronic noise or when there is large deformation of the tissue.)

There has been less attention focused toward strain imaging systems than toward strain imaging algorithms, data simulation, and performance testing. Bamber, et al., have reported[35] their progress in freehand elasticity imaging. Their system lacked real-time feedback in the data acquisition process, but still, they found that it is possible to obtain good elasticity data with freehand scanning. Their rate of success was relatively low, and significant pre- and post-processing was necessary to obtain accurate displacement estimates. The system reported by Garra, et al.[33] employed a modified mammography paddle with a hole cut out to provide an acoustic window. This allowed (relatively) easy correlation with the mammogram. However, the acoustic data acquisition system was crude. The system only allowed scanning with a 5MHz transducer—lower than the standard of its day (7.5MHz)—and had significantly poorer performance than current systems. In addition, the digitization was external to the ultrasound scanner resulting in reduced electronic SNR and increased timing jitter in the acquired echo signals. The increased jitter significantly reduces the performance of displacement estimates in strain

8

imaging. The current system used by that group incorporates a mid-range ultrasound scanner with a 5-axis motor controlled compression system.[37] The first real-time elasticity imaging system was developed for prostate imaging.[38] Data were acquired in a sector-shaped scan from an endo-cavity transducer and a 1-D tracking method was used. As a result, elasticity image frame rates were quite high at the expense of image quality.

The in vivo studies of strain imaging reported by Garra, et al.,[33] demonstrated that strain imaging has merit in differentiating among solid tumors in breasts. Their most significant finding was that invasive ductal carcinomas are significantly wider in strain images than in the corresponding B-mode image, and this difference is likely due to the desmoplastic reaction that surrounds this tumor type.

Modulus imaging has also been investigated, and there are three primary approaches in the literature. The first approach estimates the shear wavelength in tissue and from this directly estimates the shear modulus of the tissue.[39,40,41] The other techniques require simultaneous measurements of stress and strain and require assumptions regarding the boundary conditions of the experiment.[42,43,44,45,46] Compared to strain imaging, modulus imaging has lower spatial resolution, higher noise, and the assumptions regarding boundary conditions can result in biased estimates. However, estimating an intrinsic tissue parameter, instead of the relative parameters estimated in stress or strain images, makes this an attractive approach.

There are also methods under development that use acoustic radiation force to deform tissue and study tissue viscoelasticity[47,48,49] with promising results. Other novel approaches to describing the viscoelastic behavior of tissues, such as those reported by Greenleaf, et al.,[50,51] are also under investigation.

Early work in strain imaging demonstrated the limitations of tracking motion in 1-D and motivated the development of 2-D and 3-D motion tracking algorithms for elasticity imaging.[27,28,52] Those studies demonstrated that 1-D tracking failed to correctly track motion in a 3cm wide field of view with as little as 0.6% compression, and motion tracking errors got increasingly worse with increased compression. However, by using 2-D tracking algorithms that appropriately compensate for lateral motion, high contrast-to-noise images of mechanical strain could be obtained with compressions of more than 5% in phantoms (see Figure 3). The basic approach, called 'companding,' was to use 2-D motion tracking to align (warp) either the pre- or post-deformation data field prior to 1-D cross correlation.

Other early work also demonstrated the need to control motion during elasticity imaging experiments. The images in Figure 4 demonstrate that it is essential to control the motion during deformation especially with regard to elevation motion. A typical clinical ultrasound imaging system acquires echo data, nominally, from a plane of tissue. Any out-of-plane motion of tissue will result in echo signal decorrelation and reduced elasticity image quality.

The key to obtaining high quality elasticity images is the quality of the motion tracking algorithm. Ultrasound radio-frequency (rf) echo signals, the same data used to form a B-mode image, are used as a map of anatomy. Those same signals are used to track the deformation of the anatomy. The task is to accurately track the anatomical deformation with minimal uncertainty (displacement estimate variance or covariance). A review of many of the techniques used for tracking tissue motion with ultrasound can be

found in reference 53. A tutorial on the general topic of waveform coherence and time-delay estimation can be found in reference 54.

A review the assumptions used in signal correlation analysis can help to appreciate the difference between many motion tracking algorithms. A typical assumption in motion tracking based on time delay of ultrasound echo signals is that the deformation of the tissue is minimal (or recoverable) within the echo signal segment being tracked. Another common assumption is that the observation window (data segment length) is large compared to the time delay. Thus, a relatively long data segment is needed to avoid ambiguous displacement estimates (referred to as 'peak hopping'). The plot in Figure 5 demonstrates that with an rf echo segment as short as 3mm and with only 1.5% axial strain, there is obvious echo signal decorrelation between the pre- and post-deformation A-lines. However, the single large peak in the cross correlation function plotted in Figure 5 demonstrates that there is little ambiguity in the time delay required to match pre-and post-deformation signals. Using shorter rf echo segments in motion tracking reduces the decorrelation within the echo signal segment, and increases the waveform coherence, as shown in Figure 6. However, short data segments increase the likelihood of time delay ambiguity (e.g., a one-wavelength segment of rf looks very much like many other one-wavelength segments). Using multiple (usually adjacent) A-line segments reduces the likelihood of ambiguity, as shown in Figure 7. Short data segments also demonstrate the benefit of interpolating (up-sampling) the rf echo signal. The waveforms shown in Figure 6 illustrate that waveform coherence would improve if time-delays of less than one sample were available. An alternative is to interpolate the correlation function, but this requires a model for the functional form of the cross correlation function. If up-sampling the rf echo signal can be justified, it reduces the need for an accurate model of the cross correlation function when interpolating sub-sample displacement estimates, as show in Figure 8.

Development of a real-time strain imaging system

Experience in developing motion tracking algorithms and experiments with phantoms and in vitro tissues suggest criteria for a clinically viable elasticity imaging system. First, the system must track tissue motion in 2-D (or 3-D, if available) for high contrast-to-noise images.[27,28] Second, the system should use short 2-D data segments (kernels) for motion tracking to minimize decorrelation within the data segments and to minimize time-delay ambiguity. Third, the system should provide real-time elasticity images, as well as normal B-mode images, to allow the user to monitor the images being acquired and manipulate the transducer array with freehand scanning thus insuring that the tissue motion is suitable for forming high-quality elasticity images. In addition, the data acquisition technique should be similar to that currently used in sonography to increase the likelihood of clinical acceptance. A large deviation from standard clinical practice would likely receive a more skeptical assessment by potential users than a subtle modification to current practice.

A novel motion tracking algorithm has been developed and implemented on a clinical ultrasound imaging system (SONOLINE Elegra, Siemens Medical Solutions, Issaquah, WA).[29] Phase-sensitive (I-Q) echo data are processed internally in real-time on the Elegra to estimate displacement and strain. The system can use any of the linear array transducers available on the Elegra and is compatible with Tissue Harmonic Imaging on

10

that system. The system displays B-mode and strain images side-by-side on the normal system display at about 7 frames/sec. A region of interest (ROI) is displayed in the B-mode image and displacement and strain are estimated for tissue within that ROI. The size and location of the ROI can be manipulated with front panel controls. When scanning, the normal freeze and cine capabilities of the system are available. When a sequence of data is acquired and stored (frozen), on-line post-processing capabilities allow the ROI location and size to be modified, and other common tools such as modifying the grayscale mapping are available. Initial tests of the elasticity image noise and spatial resolution are found in reference 29. Spherical lesions as small as 2.4mm diameter that are three times stiffer than the background were easily displayed. The protocol for clinical testing of this system was approved by the Humans Subjects Committee at the University of Kansas Medical Center where that initial work was performed.

A critical issue in the development and utility of any imaging system is the achievable spatial resolution for a given task. The ability to image a 3mm diameter sphere in a phantom is encouraging. More importantly, those encouraging results are corroborated with the ability to image small structures in vivo. For example, images of an in vivo 3mm cyst are shown in Figure 9. Although the ability to image small structures in vivo is clearly demonstrated, the required contrast to view objects of a specific size is unknown. Investigations are underway to evaluate this through contrast-detail analysis.[55]

The ability to acquire and view long sequences of elasticity images has provided the opportunity to observe nonlinear elastic behavior of in vivo tissues. Nonlinearity in the stress-strain relationship of tissue was observed with in vitro breast tissues,[17] and was therefore expected with in vivo tissues, but was only recently observed with the availability of a real-time elasticity imaging system.[34] Figure 10 shows an example of the implications of nonlinear elasticity in strain imaging. At low preload (transducer barely in contact with the skin surface and applying minimal pressure) the fibroadenoma appears dark in the strain image. As the preload is increased (pressure applied with the transducer increasing deformation), the strain image contrast of the fibroadenoma (its stiffness relative to the surrounding tissue) decreases. This behavior might explain why others have found that some fibroadenomas are not visible in single strain images.[33]

One of the significant findings in prior clinical trials of in vivo elasticity imaging[33] was that the size of a breast lesion displayed in strain images, relative to it size in a normal B-mode image, appears to be a significant criterion for differentiating malignant from benign breast lesions. Figures 11 and 12 show examples of the B-mode and strain image pair for a fibroadenoma and an invasive ductal carcinoma, respectively. In each case, the lesion is traced in the B-mode image and that tracing is reproduced in the respective strain image. The lesion boundary traced for benign lesions have about the same size and shape in the two image types. However, the lesion boundary traced in B-mode images of invasive ductal carcinomas is much smaller than the lesion displayed in the respective strain image. On average, the area of these carcinomas displayed in strain images is three times larger than that of B-mode images.[34] It is postulated[33,34] that the increased size of carcinomas in strain images is due to the desmoplasia that often surrounds invasive ductal carcinoma.

To test the utility of relative lesion size for differentiating between benign and malignant breast lesions, five observers individually viewed a set of image sequences

from in vivo breast elasticity imaging. Each observer selected the image pair from a sequence (movie loop) that was most representative of the B-mode and strain image pair from that sequence. Each observer then traced the outline of the lesion in each image type and measured the width and height of the lesion in each image. This was repeated for data from 97 movie loops of 55 unique lesions from 29 patients. A plot of the average lesion area for each lesion measured by the group of observers is shown in Figure 13. These data are consistent with those reported by others[33] and suggest that elasticity imaging may be a useful tool to improve the utility of breast sonography. If the ratio of lesion size in strain images versus B-mode images proves to be a sensitive criterion for increasing confidence of a benign diagnosis, the fraction of biopsies that prove to be benign tissue will likely be reduced at significant savings in health care expense and trauma to the patient and their family and friends.

Summary

Elasticity imaging is a relatively new technique for studying the stiffness of tissue. The information acquired with these techniques is similar to that obtained with manual palpation, but elasticity imaging is more sensitive and less subjective than palpation. Further, the information is provided in an image format so that it can be compared with data from other image modalities and it can more easily be documented and shared with others.

Several interesting approaches to elasticity imaging are currently being investigated by research groups around the world. Different approaches provide different information about the viscoelastic properties of tissue. Many of these approaches emphasize the elastic properties of tissue due to the techniques of data acquisition.

At least one method for elasticity imaging is under development that produces images of mechanical strain in real-time using a freehand scanning technique very similar to that of standard breast sonography examinations. The system is integrated into a clinical sonography system without any external equipment and involves software changes only. In vivo tests of this system have demonstrated the ability to image small breast lesions with confidence. It has also allowed the visualization the effects of nonlinear elasticity of in vivo breast tissues. Further investigations with this system suggest that benign breast lesions are about the same size and shape in B-mode and strain images, but invasive ductal carcinomas tend to be significantly larger in strain images than in the corresponding B-mode images. This fact suggests that elasticity imaging might increase the utility of breast sonography and might be offered in clinical sonography systems in the near future.

References

[1] J Sariego, S Zrada, M Byrd, T Matsumoto, "Breast cancer in young patients," Am J Surg 1995; 170(3):243-5.

[2] PG Peer, AL Verbeek, M MRavunac, et al., "Prognosis of younger and older patients with early breast cancer," Br J Cancer 1996; 73(3):382-5.

[3] CP McPherson, KK Swenson, G Jolitz, CL Murray, "Survival among women ages 40-49 years with breast carcinoma according to method of detection," Cancer 1997; 79(10):1923-32.

[4] ME Costanza and KL Edmiston, "Breast cancer screening: Early recognition," Comp Ther 1997; 23(1):7-12.

[5] WT Yang, CO Mok, W King, et al., "Role of high frequency ultrasonography in the evaluation of palpable breast masses in Chinese women: alternative to mammography?" J Ultrasound Med 1996; 15(9):637-44.

[6] Boyd NF, Dite GS, Stone J, et al., "Heritability of mammographic density, a risk factor for breast cancer." N Engl J Med 2002; 347(12):886-94.

[7] Hou M-F, Chuang H-Y, Ou-Yang F, et al., "Comparison of breast mammography, sonography and physical examination for screening women at high risk of breast cancer in Taiwan," Ultrasound Med Biol 2002; 28(4):415-20.

[8] Kolb TM, Lichy J, Newhouse JH, "Comparison of the performance of screening mammography, physical examination, and breast US and evaluation of factors that influence them: an analysis of 27,825 patient evaluations," Radiology 2002; 225(1):165-75.

[9] Wang HC, Chen DR, Kao CH, et al., "Detecting breast cancer in mammographically dense breasts: comparing technetium-99m tetrofosmin mammoscintigraphy and ultrasonography," Cancer Invest 2002; 20(7-8):932-8.

[10] Saarenmaa I, Salminen T, Geiger U, et al., "The effect of age and density of the breast on the sensitivity of breast cancer diagnostic by mammography and ultasonography," Breast Cancer Res Treat 2001; 67(2):117-23.

[11] Laya MB, Larson EB, Taplin SH, et al. "Effect of estrogen replacement therapy on the specificity and sensitivity of screening mammography," J Nat Cancer Inst 1996; 88(10):643-649.

[12] Gao L, Parker KJ, Lerner RM, Levinson SF. Imaging of the elastic properties of tissue--a review. Ultrasound Med Biol 1996; 22(8):959-77.

[13] Ophir J, Alam SK, Garra B, Kallel F, Konofagou E, Krouskop T, Varghese T. Elastography: ultrasonic estimation and imaging of the elastic properties of tissues. Proc Inst Mech Eng 1999;213(3):203-33.

[14] Tschoegl NW. The Phenomenological Theory of Linear Viscoelastic Behavior: An Introduction. New York: Springer-Verlag, 1989.

[15] Fung YC. A First Course in Continuum Mechanics. Englewood Cliffs, NJ: Prentice Hall, 1994.

[16] Fung YC. Biomechanics: Mechanical Properties of Living Tissues. 2nd ed. New York: Springer-Verlag, 1993.

[17] Krouskop TA, Wheeler TM, Kallel F, Garra BS, Hall T. Elastic moduli of breast and prostate tissues under compression. Ultrason Imaging 1998; 20(4):260-74.

[18] Wellman PS, Dalton EP, Krag D, et al. "Tactile imaging of breast masses: first clinical report," Arch Surg 2001; 136(2):204-8.

[19] Sarvazyan A, "Mechanical Imaging: A new technology for medical diagnostics," Int J Med Inf 1998; 49(2):195-216.

[20] Dickinson RJ and Hill CR, "Measurement of soft tissue motion using correlation between A-scans," Ultrasound Med Biol 1982; 8(3):263-71.

[21] Wilson LS and Robinson DE, "Ultrasonic measurement of small displacements and deformations of tissue," Ultrason Imaging 1982; 4(1):71-82.

[22] Krouskop TA, Dougherty DA, and Vinson FS, "A pulsed Doppler ultrasonic system for making noninvasive measurement of the mechanical properties of soft tissue," J Rehabil Res Dev 1987; 24(2):1-8.

[23] Yamakoshi Y, Sato J, and Sato T, "Ultrasonic imaging of internal vibration of soft tissue under forced vibration," IEEE Trans Ultrason, Ferroelec, Freq Contr 1990; 37(2):45-53.

[24] Lerner RM, Huang SR, and Parker KJ, "Sonoelasticity images derived from ultrasound signals in mechanically vibrated tissues," Ultrasound Med Biol 1990; 16(3):231-9.

[25] Ophir J, Cespedes EI, Ponnekanti H, et al., "Elastography: A quantitative method for imaging the elasticity of biological tissues," Ultrason Imaging 1991; 13(2):111-34.

[26] O'Donnell M, Skovoroda A, Shapo B, and Emelianov S, "Internal displacement and strain imaging using ultrasonic speckle tracking," IEEE Trans Ultrason, Ferroelec, Freq Contr 1994; 41(3):314-25.

[27] Chaturvedi P, Insana MF, and Hall TJ, "2-D companding for noise reduction in strain imaging," IEEE Trans Ultrason, Ferroelec, Freq Contr 1998; 45(1):179-91.

[28] Insana MF, Chaturvedi P, Hall TJ, and Bilgen M, "3-D companding using linear arrays for improved strain imaging," Proc IEEE Ultrason Symp 1997; 97CH36118:1435-8.

[29] Zhu Y and Hall TJ. A modified block matching method for real-time freehand strain imaging, Ultrasonic Imaging 2002; 24(3):161-76.

[30] Bilgen M and Insana MF, "Elastostatics of a spherical inclusion in homogeneous biological media," Phys Med Biol 1998; 43(1):1-20.

[31] Bilgen M and Insana MF, "Deformation models and correlation analysis in elastography," J Acoust Soc Am 1996; 99(5):3212-24.

[32] Insana MF, Cook LT, Bilgen M, Chaturvedi P, Zhu Y, "Maximum-likelihood approach to strain imaging using ultrasound." J Acoust Soc Am 2000; 107(3):1421-34.

[33] Garra BS, Cespedes EI, Ophir J, et al., "Elastography of breast lesions: Initial clinical results," Radiology 1997; 202(1):79-86.

[34] Hall TJ, Zhu Y, Spalding CS, "In vivo real-time freehand palpation imaging," Ultrasound Med Biol 2003; 29(3): 427—35.

[35] Doyley M, Bamber JC, Fuechsel F, Bush NL, "A freehand elastographic imaging approach for clinical breast imaging: system development and performance evaluation," Ultrasound Med Biol 2001; 27(10):1347-57.

[36] Trahey GE, Allison JW, von Ramm OT, "Angle independent ultrasonic detection of blood flow," IEEE Trans Biomedical Eng 1987; 34: 965-7.

[37] Merritt CR, Forsberg F, Liu J, Kallel F, "In vivo elastography in animal models: Feasibility studies," J Ultrasound Med 2002; 21:S:98, (abstract).

[38] Lorenz A, Sommerfeld H-J, Garcia-Schurmann M, et al., "A new system for the acquisition of ultrasonic multicompression strain images of the human prostate in vivo," IEEE Trans Ultrason, Ferroelec, Freq Control 1999; 46(5): 1147-1154.

[39] Dutt V, Kinnick RR, Muthupillai R, Oliphant TE, Ehman RL, Greenleaf JF, "Acoustic shear-wave imaging using echo ultrasound compared to magnetic resonance elastography," Ultrasound Med Biol 2000; 26(3):397-403.

[40] Sandrin L, Tanter M, Catheline S, Fink M., "Shear modulus imaging with 2-D transient elastography," IEEE Trans Ultrason, Ferroelectr, Freq Control 2002; 49(4):426-35.

[41] Sandrin L, Tanter M, Gennisson JL, Catheline S, Fink M. "Shear elasticity probe for soft tissues with 1-D transient elastography," IEEE Trans Ultrason, Ferroelectr, Freq Control 2002; 49(4):436-46.

[42] Skovoroda AR, Emelianov SY, O'Donnell M, "Tissue elasticity reconstruction based on ultrasonic displacement and strain images," IEEE Trans Ultrason, Ferroelectr, Freq Contr 1995; 42(4):747-765.

[43] Sumi C, Suzuki A, Nakayama K, "Estimation of shear modulus distribution in soft-tissue from strain distribution," IEEE Trans Biomed Eng 1995; 42:193-202.

[44] Kallel F and Bertrand M, "Tissue elasticity reconstruction using linear perturbation method," IEEE Trans Med Imaging 1996; 15:299-313.

[45] Doyley M, Meaney PM, Bamber JC, "Evaluation of an iterative reconstruction method for quantitative elastography," Phys Med Biol 2000; 45(6):1521-1540.

[46] Zhu Y, Hall TJ, and Jiang J. A Finite Element Approach for Young's Modulus Reconstruction. IEEE Tran Med Imaging (accepted Jan 2003).

[47] Nightingale KR, Palmeri ML, Nightingale RW, Trahey GE, "On the feasibility of remote palpation using acoustic radiation force," J Acoust Soc Am 2001; 110(1):625-34.

[48] Fatemi M, Greenleaf JF, "Application of radiation force in noncontact measurement of the elastic parameters," Ultrason Imaging 1999; 21(2):147-54.

[49] Tanter M, Bercoff J, Sandrin L, Fink M. "Ultrafast compound imaging for 2-D motion vector estimation: application to transient elastography," IEEE Trans Ultrason, Ferroelectr, Freq Control 2002; 49(10):1363-74.

[50] Fatemi M, Greenleaf JF, "Ultrasound-stimulated vibro-acoustic spectrography," Science 1998; 280(5360):82-5.

[51] Fatemi M, Wold LE, Alizad A, Greenleaf JF, "Vibro-acoustic tissue mammography," IEEE Trans Med Imaging 2002; (1):1-8.

[52] Chaturvedi P, Insana MF, and Hall TJ, "Testing the Limitations of 2-D Companding for Strain Imaging Using Phantoms," IEEE Trans Ultrason, Ferroelec, Freq Contr 1998; 45(4):1022-31.

[53] Hein IA, O'Brien WD. Current time-domain methods for assessing tissue motion by analysis from reflected ultrasound echoes—A review. IEEE Trans Ultrason, Ferroelec, Freq Contr 1993; 40(2):84-102.

[54] Carter GC. Coherence and Time-Delay Estimation: An Applied Tutorial for Research, Development, Test, and Evaluation Engineers. New York: IEEE Press, 1993.

[55] Madsen EL, Frank, FR Krouskop TA, et al., Low-contrast spherical lesion phantoms for assessing leastography performance. Ultrasonic Imaging 2003; 25:61 (abstract).

15

Lesion type	5% Precompression 10%/s Strain Rate	20% Precompression 20%/s Strain Rate
Normal Fat	19 ± 7	20 ± 6
Normal Glandular	33 ± 11	57 ± 19
Fibrous	107 ± 32	233 ± 59
Ductal Carcinoma In Situ	25 ± 4	301 ± 58
Invasive Ductal Carcinoma	93 ± 33	490 ± 112

Table 1. Results of measuring the elastic modulus of in vitro breast tissue samples for a variety of breast tissue types with two different strain ranges and strain rates. Ductal carcinoma has the largest difference for modulus measurements in these two conditions suggesting it has the most nonlinear stress-strain relationship among tissues measured.
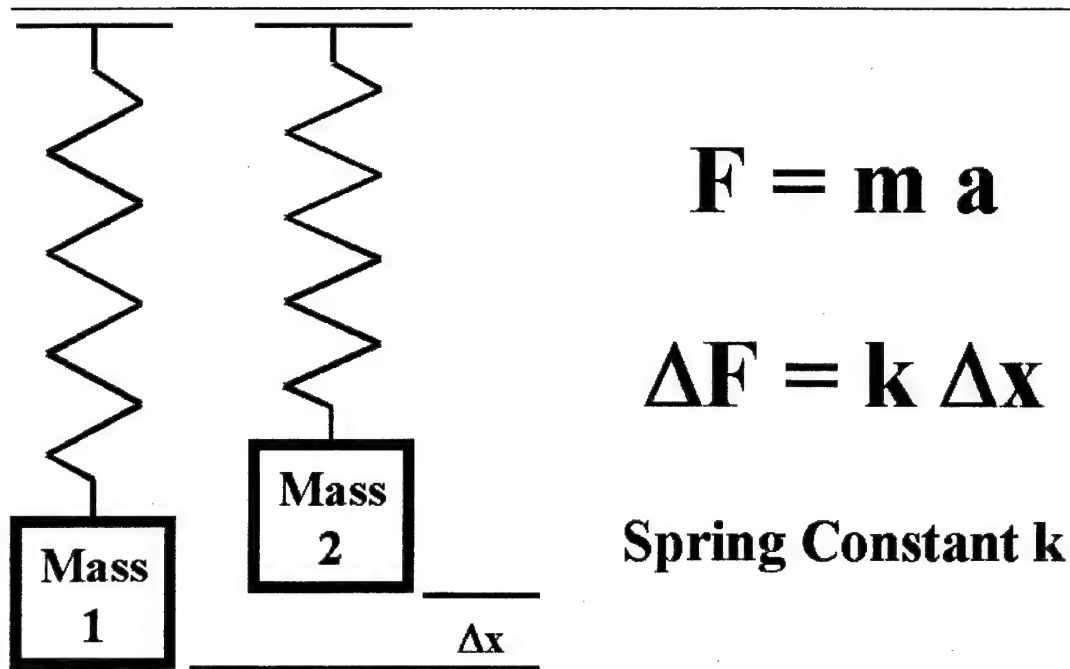
Figure 1. Introductory mechanics describes the behavior of a spring supporting different masses. The diagram illustrates how one spring would be stretched to two different lengths by two different masses. Hooke's law describes this behavior and can be used to characterize the spring under small deformations. Newton's second law equates a force, F, with a mass, m, and an acceleration, a. A known mass suspended from a spring exerts a known force due to the acceleration of gravity. Hooke's law relates the difference in stretch of the spring, Δx, due to the change of force, ΔF, resulting from suspending different masses. The proportionality constant, k, characterizes the stiffness of the spring.
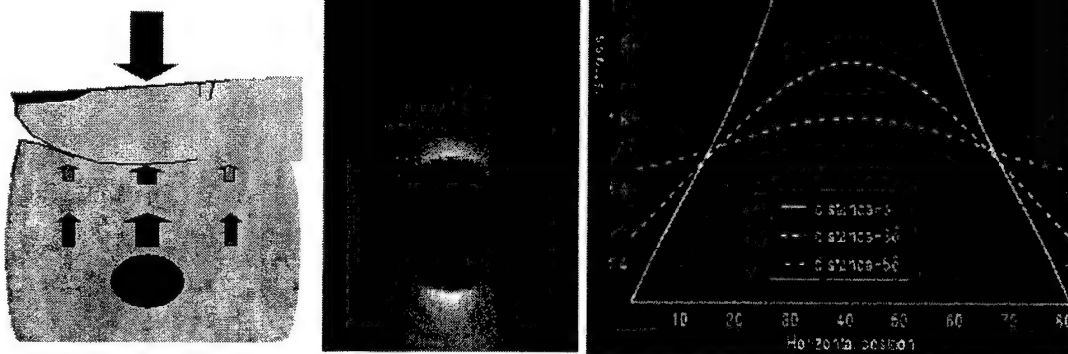
Figure 2. Palpation can be approximated with a simulation tool (FEA). The center image is the axial stress distribution resulting from a uniform displacement of the top surface of a block containing a spherical object. The plot on the right shows profiles of the stress distribution across the lines in the center image. A large variation in the stress profile is found for the profile close to the spherical object. This simulates a sphere being near the surface of the block. As the profile moves further away from the sphere, the variation in stress across the profile decreases suggesting the sphere would be more difficult to palpate as it is placed deeper in the block.
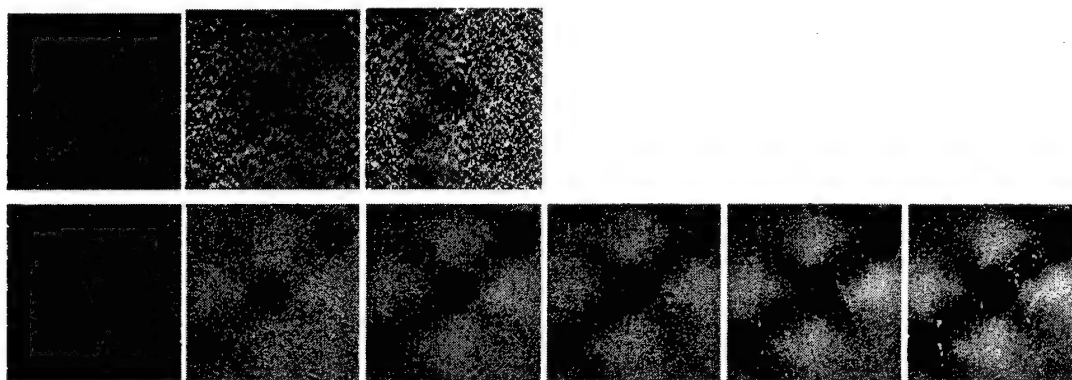
Figure 3. Images of the mechanical strain in the axial direction for a gelatin phantom with three cylinders which are three times stiffer than the background. The top row shows strain images obtained with 1-D tracking using cross correlation. The bottom row shows images obtained with 2-D companding (2-D motion tracking). The applied deformation (top and bottom rows), from left to right, is 0.6%, 1.2%, 2.4% 3.6%, 4.8% and 6.0% strain. Lateral expansion (bulging) occurring with axial compression causes the echo A-lines to not match and the echo signals to decorrelate with 1-D tracking. 2-D tracking is able to track the lateral as well as axial motion to obtain higher contrast-to-noise strain images.
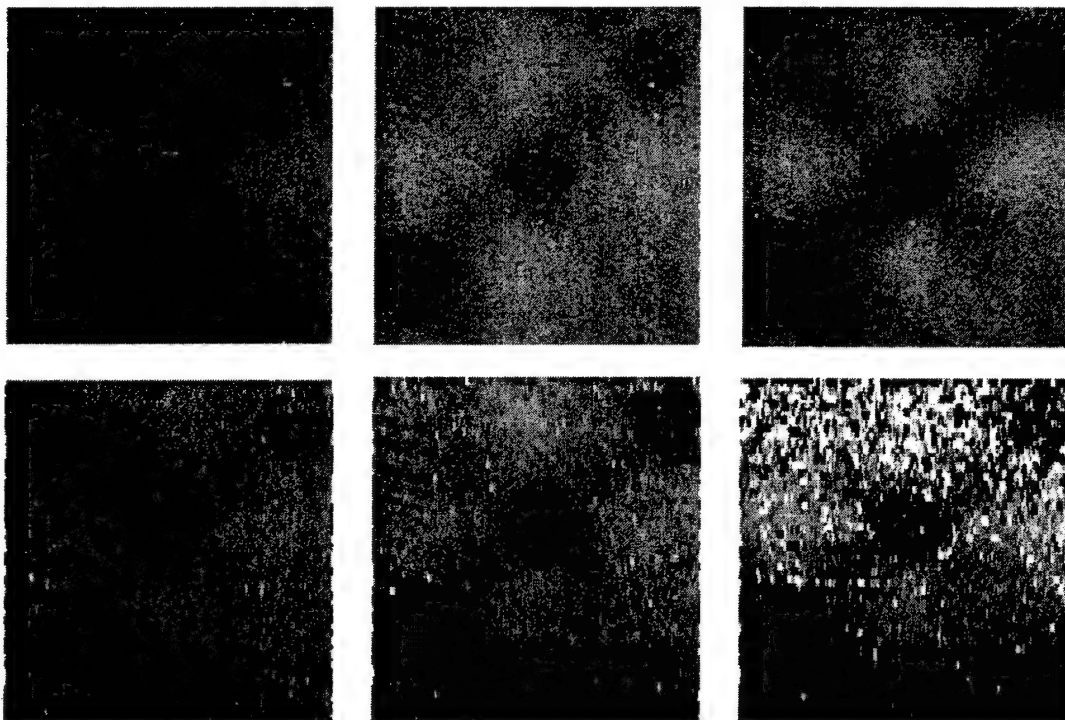
Figure 4. Images acquired near the edge (in elevation, perpendicular to the image plane) of a gelatin phantom with varying deformation (from left to right, 0.6%, 1.2% and 2.4% axial strain). The phantom was bound in elevation at the bottom and slid freely at the top. As the phantom was deformed, the top slid out of the image plane in elevation resulting in echo signal decorrelation. Increasing the deformation caused greater decorrelation.
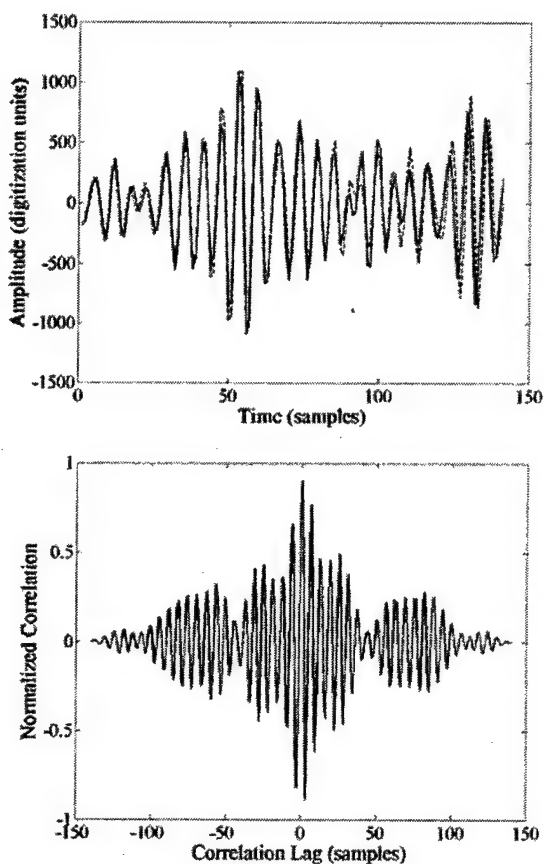
Figure 5. On top is a plot of the pre-deformation (red dashed line) and post-deformation (1.5% axial strain, solid blue line) for a 3mm segment (140 rf samples) of the echo signals from the center of a gelatin phantom. The post-deformation signal has been shifted in time to match the pre-deformation signal as well as possible. The deformation has caused decorrelation in the echo signal which reduces coherence (cross correlation coefficient = 0.87). Below is a plot of the cross correlation function comparing the pre- and time-delayed post-deformation rf echo signals shown above. The single large positive peak suggests there is little ambiguity in the correct delay required to match these signals.
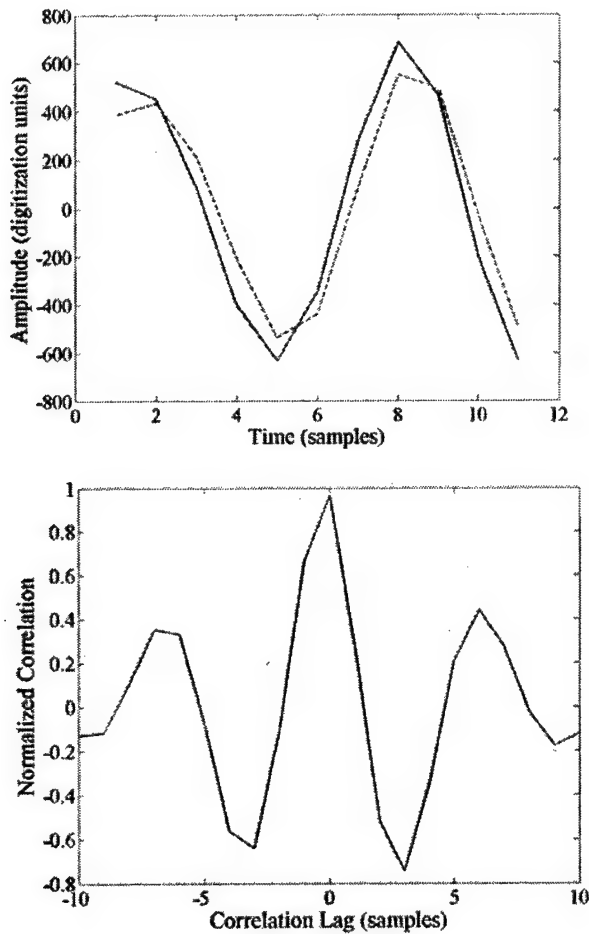
21

Figure 6. On top is a plot of the pre-deformation (red dashed line) and post-deformation (1.5% axial strain, solid blue line) for a 0.24mm segment (11 rf samples) of the echo signals from the center of a gelatin phantom. The post-deformation signal has been shifted in time to match the pre-deformation signal as well as possible. Little decorrelation in the echo signals within this short echo segment results in high coherence (cross correlation coefficient = 0.96). Below is a plot of the cross correlation function comparing the pre- and time-delayed post-deformation rf echo signals shown above.
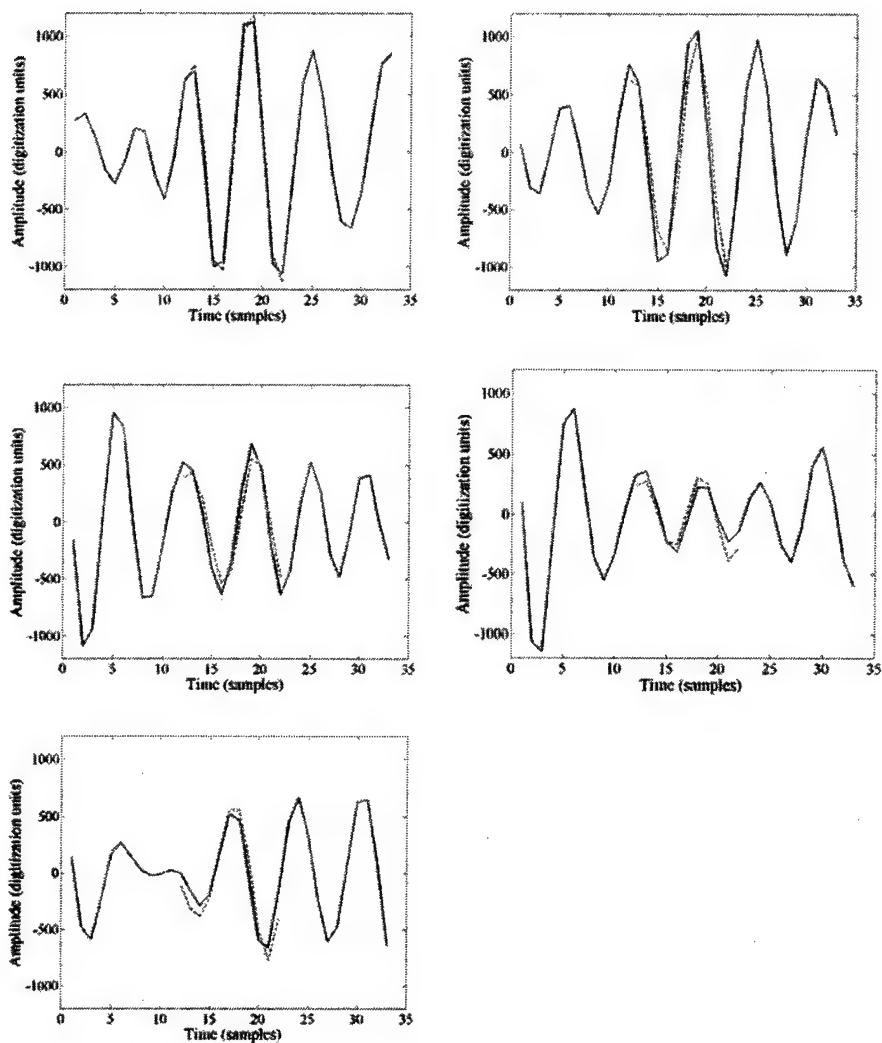
Figure 7. Plots of the pre-deformation (solid blue) and the time-shifted post-deformation (1.5% strain, dashed red) rf echo signal from five adjacent A-lines obtained near the center of a gelatin phantom. Using multiple short line segments reduces decorrelation within the data segment while simultaneously reducing the ambiguity in time-delay estimation.
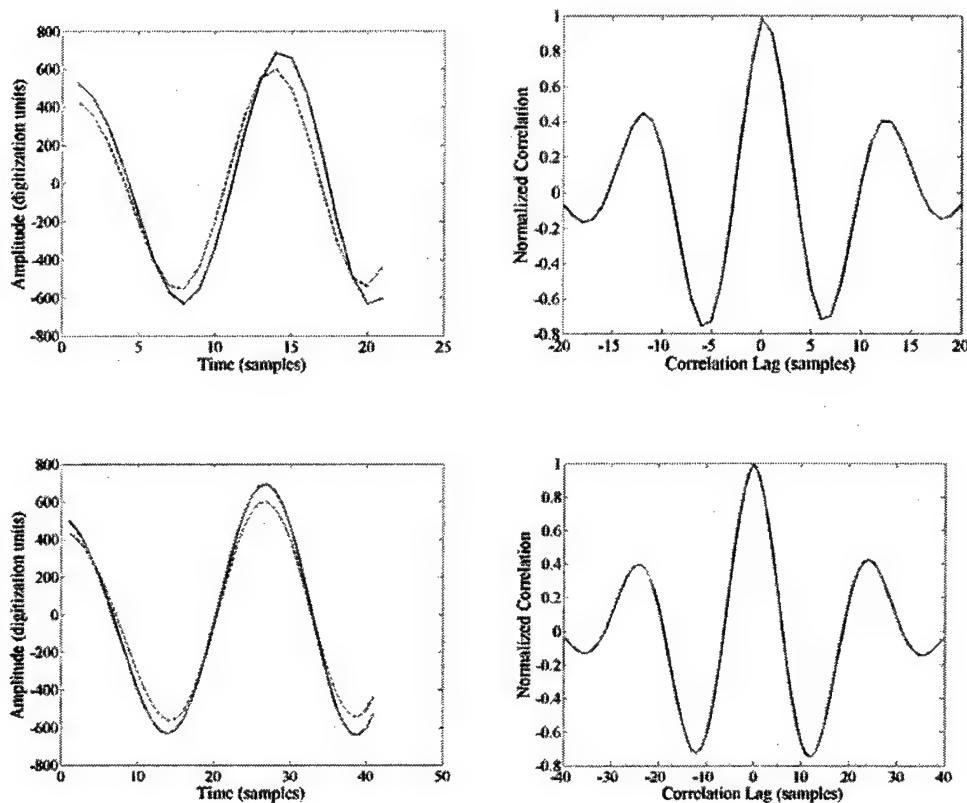
Figure 8. In the left column are plots of the pre-deformation (red dashed line) and post-deformation (1.5% axial strain, solid blue line) for a 0.24mm segment of the echo signals acquired at 36MHz sampling frequency up-sampled to 72MHz (top row) and 144MHz (bottom row). The post-deformation signal has been shifted in time to match the pre-deformation signal as well as possible. As the effective sampling interval is reduced, the integer time delay error is also reduced allowing for greater waveform coherence (correlation coefficients of 0.965 (Figure 6), 0.978, and 0.998 were obtained with 36MHz, 72MHz and 144MHz sampling, respectively).

24

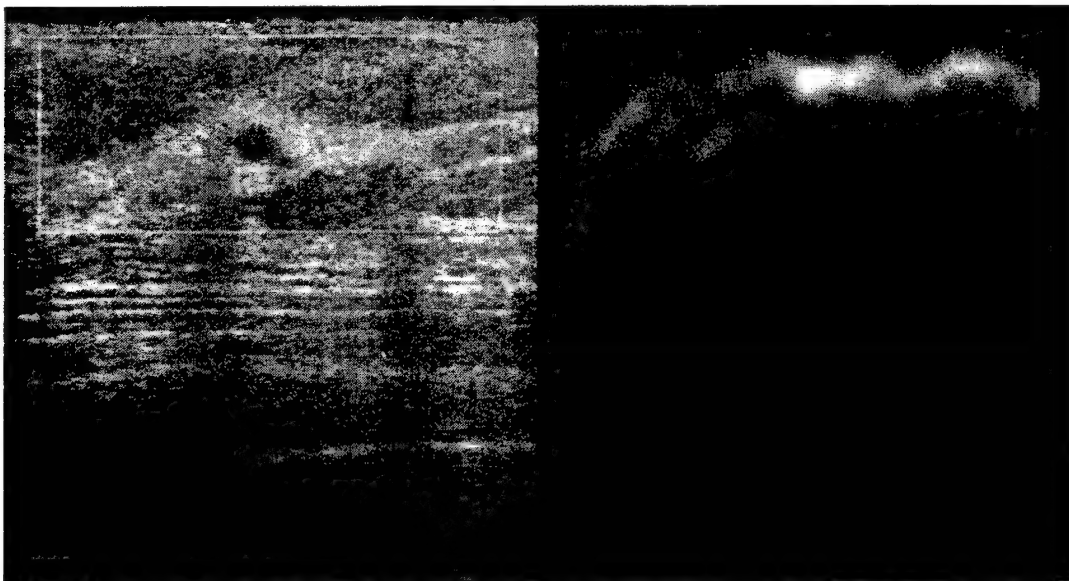
Figure 9. B-mode and elasticity (mechanical strain) images of a 3mm diameter in vivo breast cyst demonstrating that small in vivo structures are resolvable in strain images.
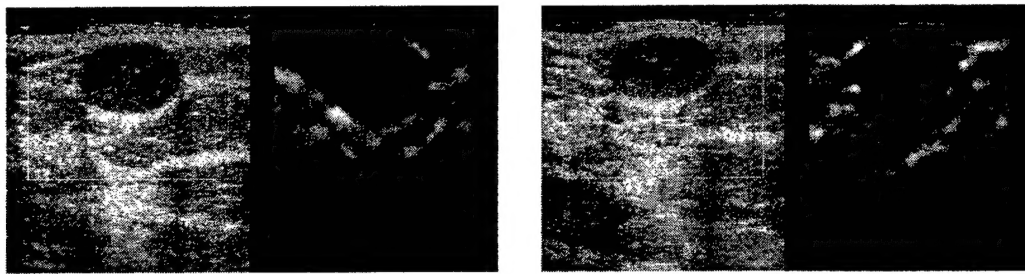
Figure 10. B-mode and strain images of a typical fibroadenoma at two different amounts of deformation (preload). For both elasticity images the average strain in the image is about 1.2%. The image pair on the left was acquired with the ultrasound transducer just barely in contact with the skin surface. At low preload fibroadenomas typically are stiff compared to their surrounding glandular tissue. As the preload increases the strain image contrast of the fibroadenoma decreases and the lesion becomes nearly equal stiffness compared to the surrounding tissue.
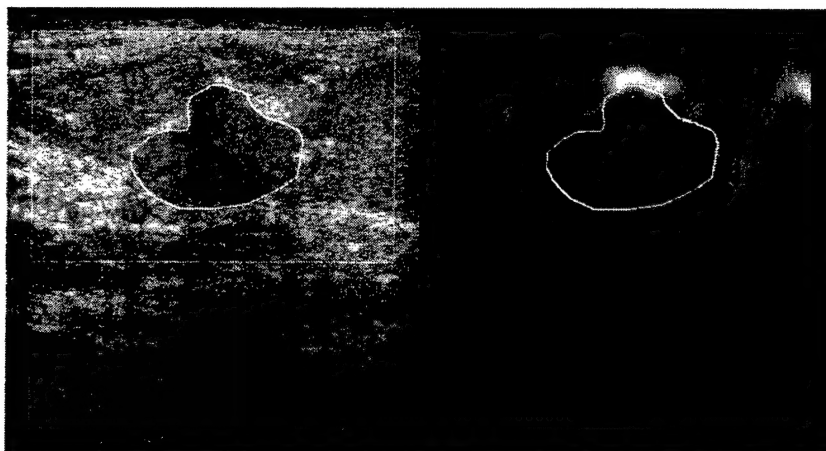
Figure 11. A B-mode and strain image pair of a fibroadenoma. The lesion is traced in the B-mode image and that tracing is displayed in the strain image. The lesion size and shape in the two image types are very similar.
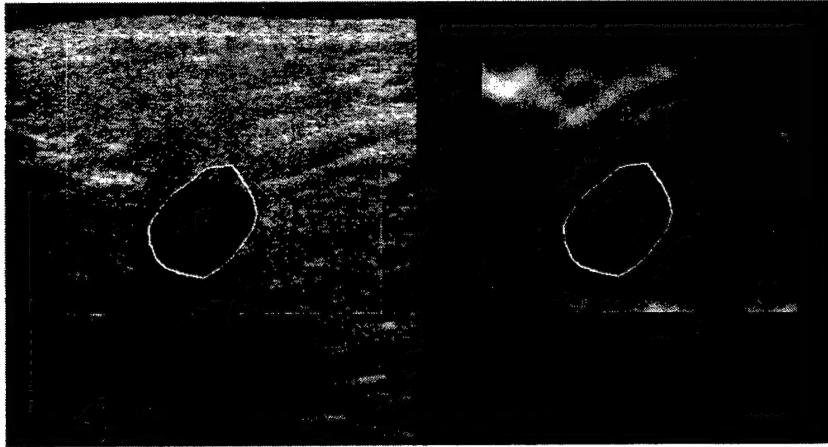
Figure 12. A B-mode and strain image pair of a scirrhous invasive ductal carcinoma. The lesion is traced in the B-mode image and that tracing is displayed in the strain image. The lesion size is larger in the strain image than in the B-mode image.
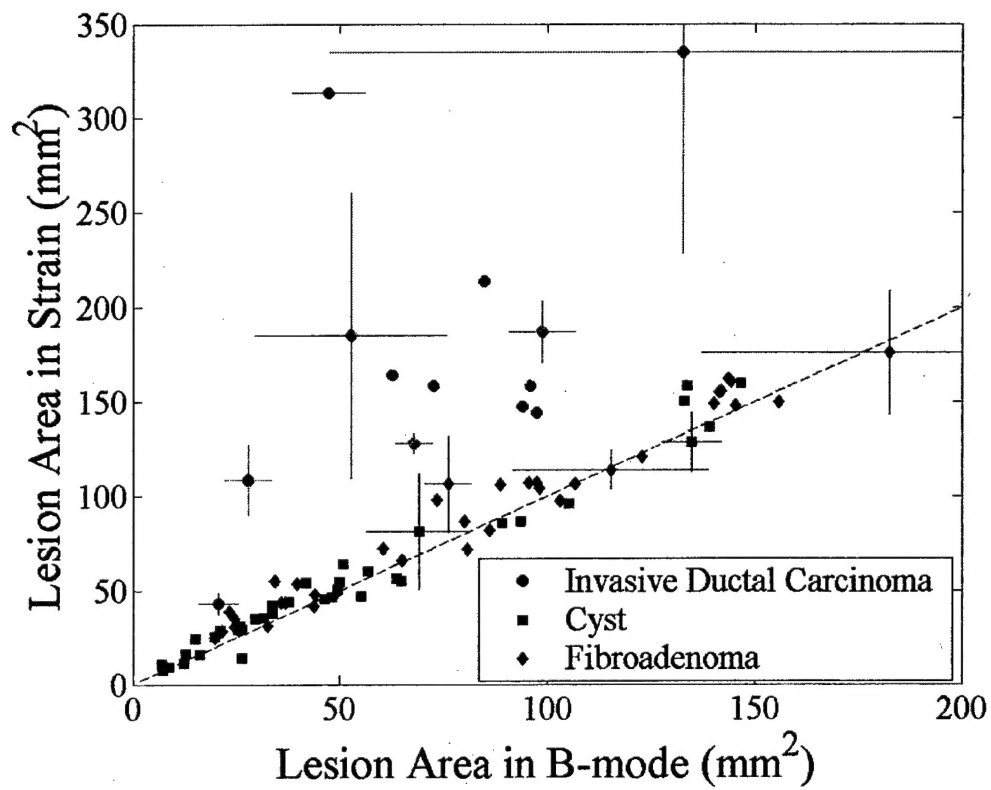
Figure 13. A plot of the lesion area measured in strain images versus the same lesion measured in the corresponding B-mode images for cysts, fibroadenomas and invasive ductal carcinomas. The average result of five observers is plotted and error bars represent standard deviations among those measurements. The dashed line represents equal area in both image types.